Investigation of passive root flaps on HAWT

An experimental analysis of different configurations of root flaps on the performance of Horizontal Axis Wind Turbines

Zohaib Saleem B.Sc.

13/05/2019

Faculty of Aerospace Engineering · Delft University of Technology

TUDelft

Delft
University of
Technology

Investigation of passive root flaps on HAWT

An experimental analysis of different configurations of root flaps on the performance of Horizontal Axis Wind Turbines

MASTER OF SCIENCE THESIS

For obtaining the degree of Master of Science in Aerospace Engineering at Delft University of Technology

Zohaib Saleem B.Sc.

13/05/2019

Faculty of Aerospace Engineering · Delft University of Technology

The undersigned hereby certify that they have read and recommend to the Faculty of Aerospace Engineering for acceptance a thesis entitled **"Investigation of passive root flaps on HAWT"** by **Zohaib Saleem B.Sc.** in partial fulfillment of the requirements for the degree of **Master of Science**.

Dated: 13/05/2019

Supervisors:

Dr. ir. Carlos Simão Ferreira

Dr. ir. Daniele Ragni

Dr. Andrea Sciacchitano

Abstract

Passive root flaps and in particular the Gurney flaps have been employed for improving aerodynamic characteristics for various applications since the 1970's [1]. The effects of passive flaps on two dimensional airfoils have therefore been studied extensively, however, research on their application to Horizontal axis wind turbine blades (HAWT) is lacking and scarce. This research is a part of ongoing efforts at the Delft University of Technology to fill this missing gap.

The blade of a HAWT is generally divided into three different regions for aerodynamic analyses. The region closest to the rotational axis is defined as the root region ($r/R = 0 : 0.3$) [2] [3]. This region experiences the lowest rotational speeds and requires higher structural strength, resulting in a thick airfoil section. Although this section does not contribute significantly to the power generation of the whole turbine, the flow from this region does however effect the performance of the rest of the blade. Improving the aerodynamic flow characteristics of this region, therefore, increases the performance of the whole turbine.

For this research, passive (i.e. stationary) flaps were considered to enhance the flow at the root region and experimental analyses carried out at the Open Jet Facility (OJF) wind tunnel of TU Delft. An LM388 wind turbine blade (of Nordex N80 wind turbines) was used as a reference to create a scaled blade. The Analyses consisted of load (power and thrust) measurements and calculations for various flap configurations on a scaled wind turbine model. Furthermore, to understand how the flow is effected by the augmentation of flaps a Stereoscopic Particle Image Velocimetry (SPIV) was carried out for the most effective flap configuration and also no-flap configuration for the sake of comparison.

Acknowledgements

Contents

List of Figures

List of Tables

Part I

Introduction

Chapter 1

Introduction

Figure 1.1: Model/Illustration of the first documented *(vertical axis)* windmills from the ancient Greater Khorasan region *(includes present day Afghanistan and Iran among others)*

1.1 A brief background

Wind power has come a long way from the earliest documented windmills *"doulab"* found and some still operated to this day in the ancient Greater Khorasan region *(includes present day Afghanistan and Iran among others)* to today's wind turbines with rotor diameter reaching 180m [9].

Furthermore, with the ever growing concerns for the global warming and its negative impact, renewable technologies are being developed and installed at a significant pace. Wind Energy, being one of the main sources of renewable energy, has seen a steadily increasing growth and reached 487GW of installed capacity in 2016. [10] Research to further improve the technology is ongoing and this research forms a part of that effort.

The rotation of horizontal axis wind turbine blades result in different sections of the blade experiencing different rotational velocities, which influences it's shape. The region closest to the axis, defined as the root region ($r/R = 0 : 0.3$) [2] [3], experiences the lowest rotational speeds and requires higher structural strength, resulting in a thick airfoil section. These factors result in less significant contribution towards the power generation of the turbine and encounters high angles of attack during operation at the root region which result in strong Coriolis and Centrifugal forces [11]. Figure 1.2 illustrates how omitting certain sections of the blade affect the power coefficient C_P, but it is a wrong idea to ignore this region without any consequences [12], as the flow in this region affects the performance of the rest of the blade. Figure 2.15b shows how the stall at the root region travels outboard of the blade.
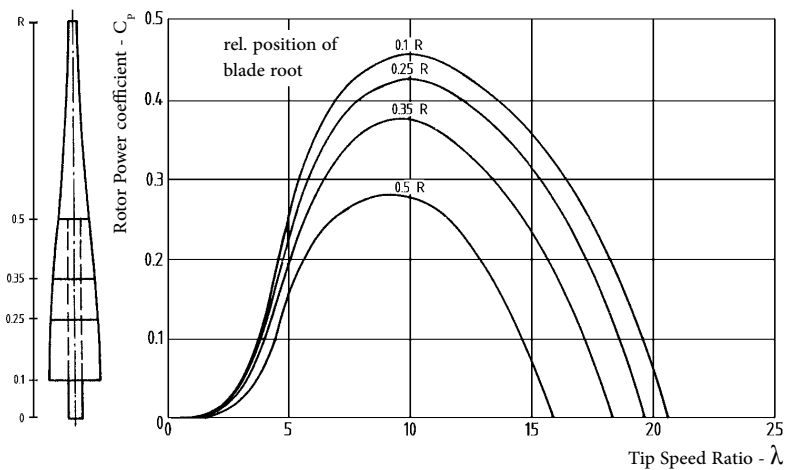
Figure 1.2: Influence of omitting sections of the blade area near the hub on the rotor power coefficient C_P [12]

To counter these effects that occur at the root of the HAWT blades, various configurations of Gurney flaps were considered for an experimental investigation, followed by flow visualization to get a better understanding of the flow behavior.

1.2 Research question, aims and objectives

In the preceding sections, a brief overview of the research done on Gurney Flaps (microtabs) has been presented. Most of this research was numerical and computational in nature. The experimental work has mostly been done on stationary two-dimensional airfoils with only a hand full on helicopter blades. Therefore for a better understanding of this flow-control device especially for operational wind energy application, experimental research is needed. From this, the research question can be derived as:

How does the addition of Gurney flaps to the root region of a HAWTs effects its performance and how do the experimental results compare with the numerical simulation of the same set-up carried out previously?

4

From this research question, multiple sub-questions can be derived;

1. How do different types/profiles of Gurney flaps effect the performance of the HAWTs?

2. What effects can be observed by altering the location of Gurney flaps on the HAWTs root region? And which position yields the best results?

3. How do the values calculated from the Particle image velocimetry compare with the data collected and calculated from the sensors on the HAWTs experimental model?

4. How do the addition of flaps effect the flow around the HAWT blades?

These questions lead to the following goals;

Definition of the problem statement: Flow at the root region of a wind turbine is a complex phenomenon and influences the performance of the rest of the blade, however, requires more research for a better understanding. Also, how do miniflaps of different shapes and sizes influence the flow and the performance at the root region?

Formulation of the experimental setup: In order to get a better understanding, a scaled model wind turbine experimental setup will be prepared. This includes the sizing and selection the mini-flap configurations and other experimental parameters, such as the tip-speed ratios, wind speed, etc.

Understanding the flow phenomenons: To get a better understanding of the flow, SPIV will be carried out for the same scaled model setup. SPIV will be used to get out-of-plane velocity component besides the in-plane components. This analysis will be carried out for the whole blade at multiple selected span-wise locations for flapped and no-flaps configurations.

Post-processing the results: The SPIV results will be post-process both for the flapped and no-flaps configuration. Comparing the results of the two configurations will shed light on the three-dimensional flow around wind turbine blades and how the addition of the flaps influences the flow.

Chapter 2

Research Background

2.1 Passive flow control devices

The rapid development of the sustainability technologies and in particular wind energy is pushing the industry to create bigger wind turbines with higher power production capabilities. This results in increasingly large rotor diameters presently in the range of $160m$ with a $180m$ of AD 8-180 [9] under production. However, this poses logistical, material and structural issues [13]. Therefore, the challenge is to increase the efficiency and get more out of the already massive turbines. One of the ways of achieving this is to increase the aerodynamic efficiency of blades by augmenting flow control devices, which are usually low cost and easy to install.

There are various ways that the flow control devices for the wind turbine can be classified but one simple categorization can be done based on their operational principles. [14] Also techniques that can be augmented post-production have only been taken into consideration and methods like thickening of the trailing-edge, Camber morphing, blowing and suction techniques [15] have been omitted.

1. **Passive flow control devices**

    (a) Vortex Generators
    (b) Microtabs / Gurney flaps
    (c) Serrated trailing edge
    (d) Fences
    (e) Spoilers

2. **Active flow control devices**

    (a) Trailing-edge flaps
    (b) Synthetic jets
    (c) Air Jet Vortex Generators

As the research focuses on **microtabs | Gurney flaps**, other passive flow control devices will be briefly discussed in the following paragraphs before moving on to a detailed decision on Gurney flaps in the following section 2.2.

2.1.1 Vortex Generators

The vortex generators (VG) were introduced by Harlan D. Taylor in 1947 [18] and a lot of research has been done on them since then. The main objective of the VGs is to delay the

(a) Spoilers [16]

(b) Fences [17]

(c) Vortex Generators

(d) Serrated trailing edge
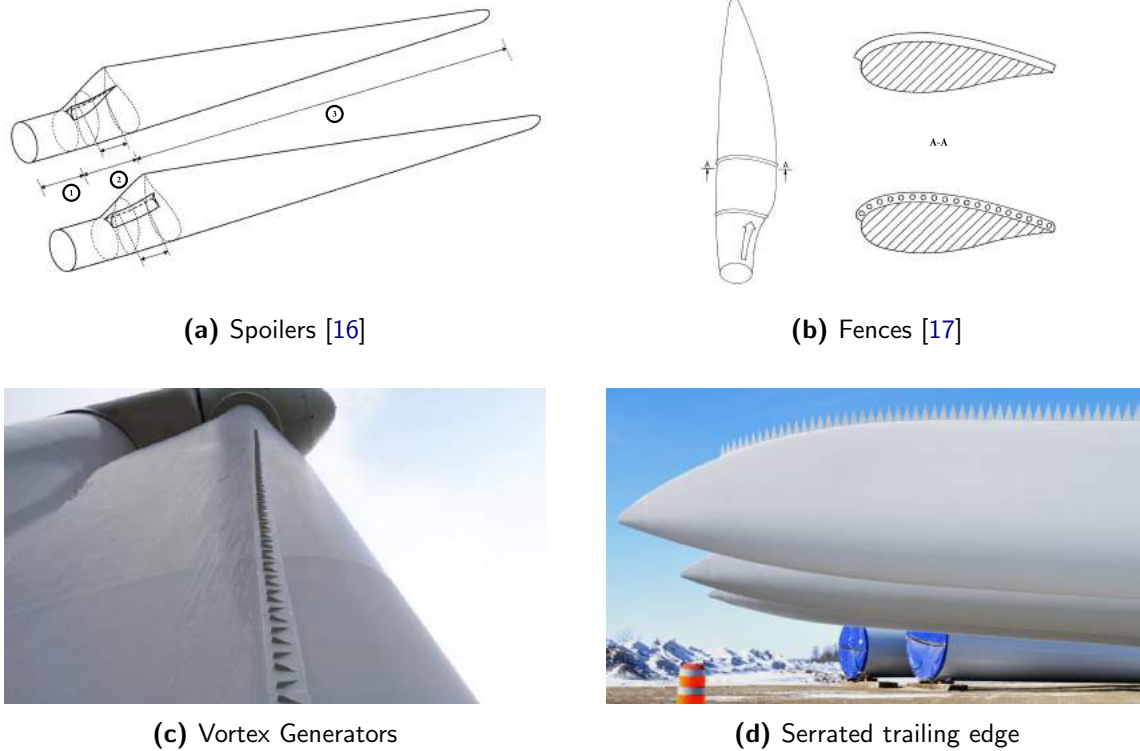
Figure 2.1: Different passive flow control devices installed on Wind Turbine blades

flow separation, which is achieved by creating a vortex that energizes the normal boundary layer, making it more resistant to flow separation than a stagnant boundary layer. VG are most effective with triangular geometry which generate counter rotating vortices according to research done by Gordard et al. [19]. It is, therefore, no wonder that this is the most prevailing shape, as can also be seen in figure 2.1c. Bruce et al. [20] carried out an experimental study on Gurney Flaps and VG and found that combining the two devices generates higher lift than either device on its own.

2.1.2 Spoilers

In section 1.1 the root region was defined as $r/R = 0 : 0.3$, but according to Lenz and Fuglsang [16], the section of a blade wind turbine can also be defined by its shape, i.e.;

1. Circular region - Closest to the hub
2. Transitional region - between the circular and airfoil region
3. Airfoil region - This section has an airfoil profile.

This division of the blade can also be seen in figure 2.1a. The term spoiler originally comes from the aerospace industry where spoilers are installed on wings to "spoil", i.e. reduce the lift and increase drag. This definition is closer to the spoiler for wind turbines as defined by Franco et al. [15] and can also be seen in figure 2.2b. Another variation of a spoiler for wind turbines can be seen in figure 2.2a, which also works by increasing drag on the root section of the wind turbine blade. 'Spoilers' as defined in the European patent [16] *(see figure 2.1a)* are

also employed on certain wind turbine models of Sevion *(formally RePower)*, namely the MM82 *(figure 2.3a)* and the MM92 *(figure 2.3b)*. However, in scientific literature, flow control devices added to the suction side of wind turbines are classified as Gurney flaps or micro-tabs.

(a) Root Spoilers [14]

(b) Spoilers on the leading edge [15]
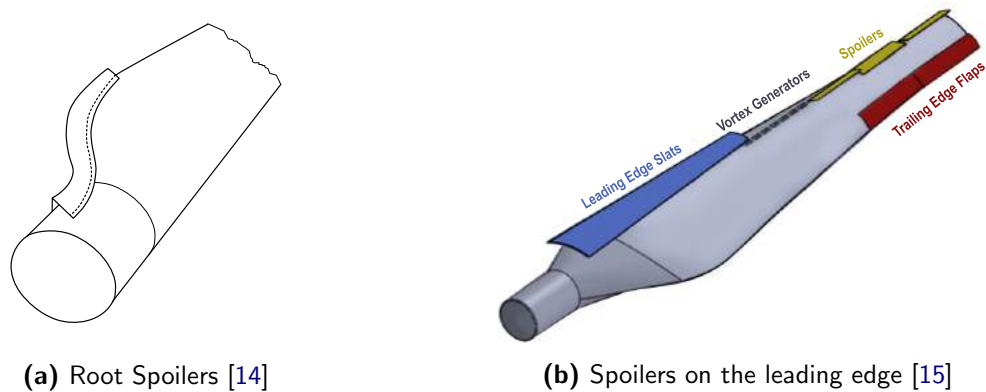
Figure 2.2: Different types of spoilers for Wind Turbine blades

(a) Close-up of spoiler on Sevion MM82

(b) Spoiler and fences on the blades of Sevion MM92

Figure 2.3: Spoilers installed on Sevion MM82 and MM92 wind turbine blades

2.1.3 Serrated trailing edge

The serrated trailing edge has been designed to combat noise during the operation of wind turbines and other aeronautical applications. The noise reduction is accomplished by the serration of the trailing edge to effectively scatter the vorticity at the training edge. One such solution was first patented by Siemens in 2003 and named 'Dino Tail' [14]. This technology is being used for actual wind turbines and one such example can be seen in figure 2.1d. According to an experimental study carried out at the Dutch National Aerospace Laboratories (NLR), a reduction of $2-3$dB can be achieved by serrating the trailing edge close to the tip, which is the main source of noise [21].

2.1.4 Fence

As mentioned before, different sections of the wind turbine blade experience different flow conditions and influence the flow of other sections. Fences are a system proposed to counter this by disrupting the span-wise outboard airflow to prevent the developing inboard stall at the

root to grow outwards [17]. This phenomenon is explained by Herráez et al. [22] and can also be seen in figure 2.15b where the flow on the suction side at different wind speeds, namely: a) $U_\infty = 10\,\mathrm{m\,s^{-1}}$, b) $U_\infty = 15\,\mathrm{m\,s^{-1}}$, c) $U_\infty = 19\,\mathrm{m\,s^{-1}}$ and d) $U_\infty = 24\,\mathrm{m\,s^{-1}}$ is visualized. The fences flow control device achieves this by vertical *'fences'* that are installed close to the root section as can be seen in figures 2.1b and 2.3b.

2.2   Gurney Flaps

Gurney Flaps, also referred to as 'micro-tabs', 'mini-flaps' and 'micro-flaps' in the literature [23], are small tabs placed either at or close to the trailing edge of an airfoil usually on the pressure side. The Gurney flaps are named after the American racing car driver and constructor Daniel Sexton Gurney, who is credited for first installing and using them on a race car in 1971 [24]. He observed that they improved the traction of the car and helped it achieve higher speeds. Actual flow measurements were however first carried out by Liebeck in 1978 [1]. He postulated the flow around a Gurney flap at the trailing edge of an airfoil with two counter rotating vorticies downstream of the flap as seen in figure 2.4. Liebeck hypothesized flow was later confirmed by numerical and experimental studies [25]. The Gurney flaps influence the local camber of the trailing edge and increase lift by altering the Kutta condition.
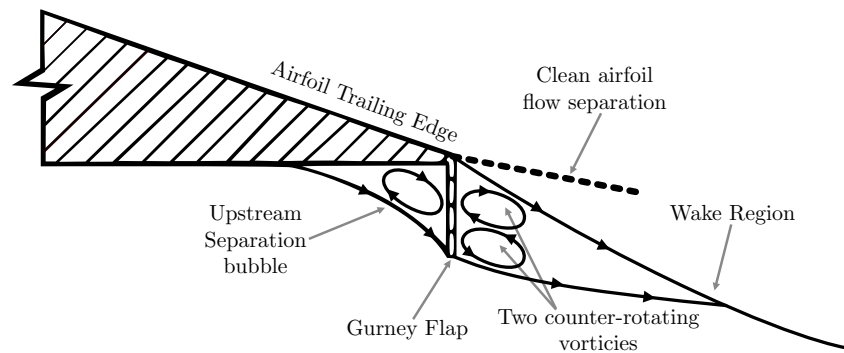
Figure 2.4: Hypothesized flow at trailing-edge of an airfoil with a Gurney flap based on [1]

The geometry and the placement of the microtabs play a significant role in how they influence the flow and the performance of an airfoil. Different aspects like height h, deflection angle ϕ, thickness t, location s and Reynolds number Re were studied and are discussed in the following paragraphs to explain their effect on the aerodynamic performance.

2.2.1   Height

The height of the Gurney flaps, usually measured as a percentage of the chord length [% c], plays a vital role in its performance enhancement, according to Giguère et al. [26] and Wang et al. [27]. The optimal height for the Gurney flaps is not larger than the local boundary layer thickness of the flow. Gurney flaps with larger heights do increase lift, however, it is not linear with the height of the flap [28] as can also be observed in figure 2.5a. Maughmer et al. [29] conclude from their experimental research on the GF with various heights that the drag properties of the airfoil are mainly influenced by the height of the GF. A numerical investigation

conducted by Jang et al. [25] concluded that Gurney flaps with heights up to $1.25\%\,c$ increase the lift without having significant impact on drag. Similarly Liebeck [1] concluded that Flaps with $h > 2\%\,c$ increased the drag significantly. Brown and Filippone [30] have proposed a semi-empirical relation to determine the optimal flap height h_{opt} based on the airfoil chord c [m] and the free-stream velocity V_∞ [m s^{-1}].

$$h_{opt} = 37.155 \left(\frac{c^{0.8}}{V_\infty^{0.2}} \right) \cdot 10^3 \tag{2.1}$$

(a) $C_L\,vs.\,\alpha$ curves

(b) $L/D\,vs.\,\alpha$ curves
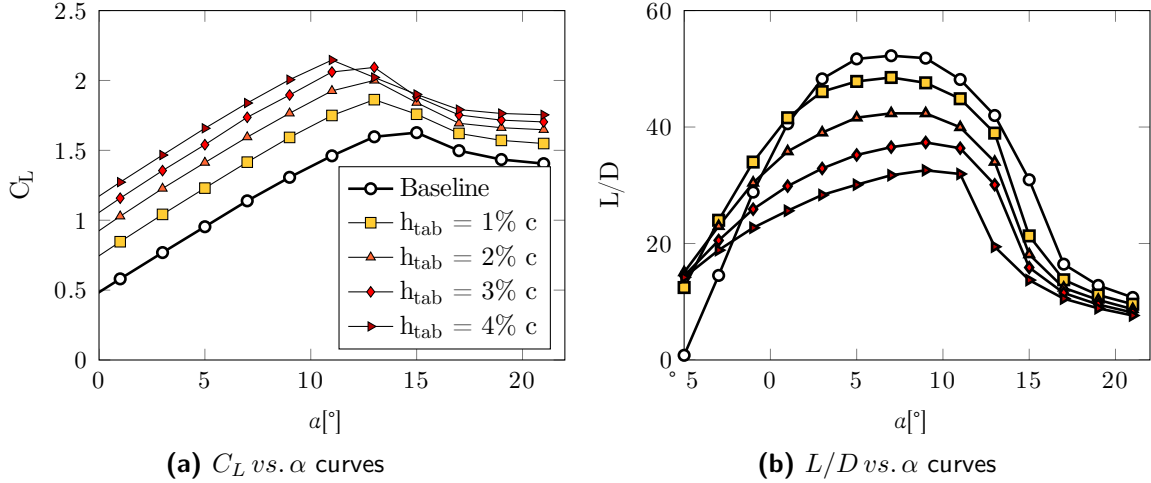
Figure 2.5: Effect of different heights $(1\%\,c - 4\%\,c)$ of micro-tabs placed on the pressure side of an Althaus AH93W174 airfoil at the trailing edge $(Re = 1 \times 10^6)$ [28]

2.2.2 Deflection angle

Gurney Flaps and microtabs are usually deployed at a 90° angle, i.e. perpendicular to the airfoil. Therefore, there is not a lot of research done on this aspect and just two experimental studies were found by Nengsheng et al. [4] and Wang et al. [27] which deal with static Gurney Flaps of various deflection angles $[\phi]$, namely 45°, 90°, 135° and 45°, 60°, 90° respectively. The angles are measured from the trailing edge as shown in figure 2.6a. According to Nengsheng et al. [4], the standard 90° flaps result in the highest C_L values followed by 135° and finally 45°, as can be seen in figure 2.7a. The C_D values however, are very similar and 90° just being slighter higher for α angles $10° - 20°$. Experiments by Wang et al. [27] also observed similar results with highest C_L and C_D values for $\phi = 90°$ and lower values when $\phi < 90°$. Other interesting computational study was found that dealt with active swinging Gurney flaps, by Woodgate et al. [5, 31] and therefore not completely applicable for the static case, however, an interesting flow visualization can be seen from this numerical study in figure 2.8.

2.2.3 Location

Wang et al. [27] carried out experiments to study the effects of the location of GF mounted close to the trailing edge on airfoil aerodynamic properties. The flaps were positioned at $s = 0\%\,c$, $2\%\,c$, $4\%\,c$, $6\%\,c$ as defined in figure 2.6a. Moving the flaps away from the trailing edge has a negative impact on the $C_{l_{max}}$, reducing it by 0.2%, 0.5% and 3.8% for the $2\%\,c$, $4\%\,c$

(a) Gurney Flap angle definition [27]

(b) Gurney Flap angle configuration as defined in [4]
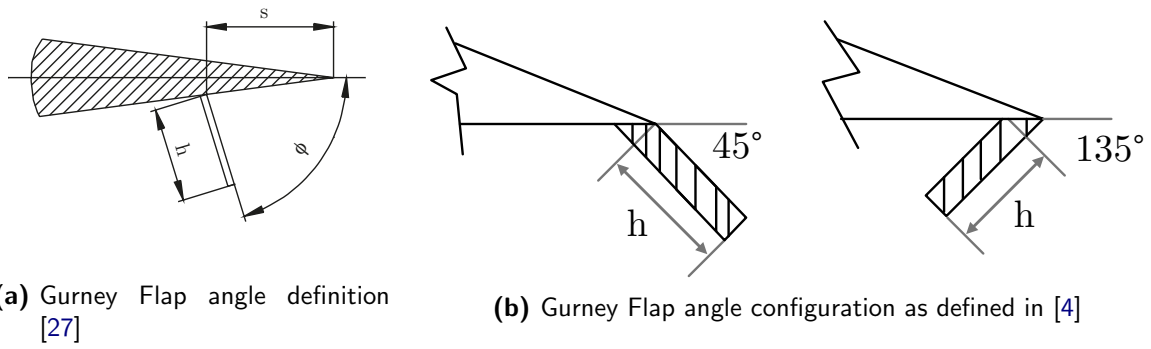
Figure 2.6: Gurney Flap angle configurations

(a) C_L and C_D $vs.\,\alpha$ curves

(b) C_L $vs.\,C_D$ curves
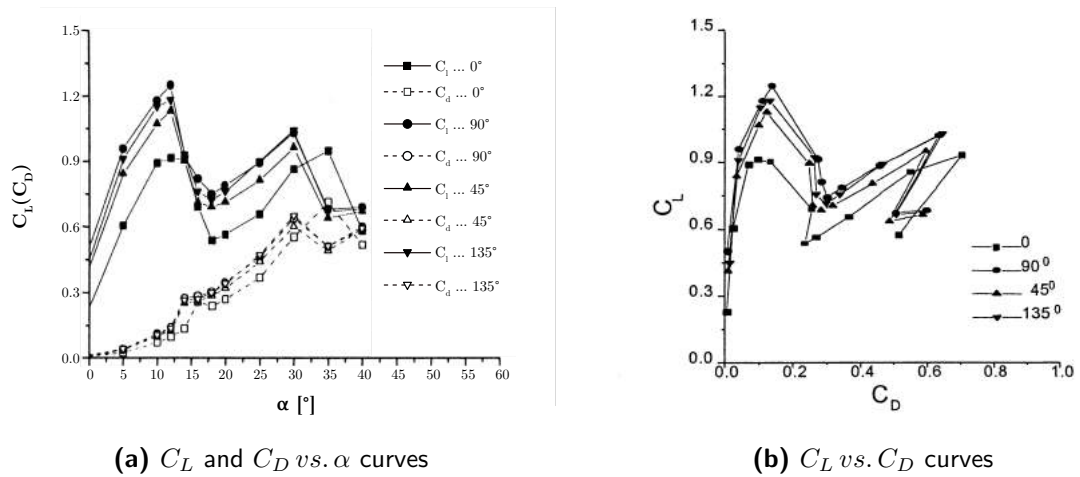
Figure 2.7: C_L and C_D curves for $2\%\,c$ height Gurney Flaps with different trailing edge angles [4]

(a) C_P behind a swinging Gurney Flap at $45°$

(b) C_P behind a swinging Gurney Flap at $135°$
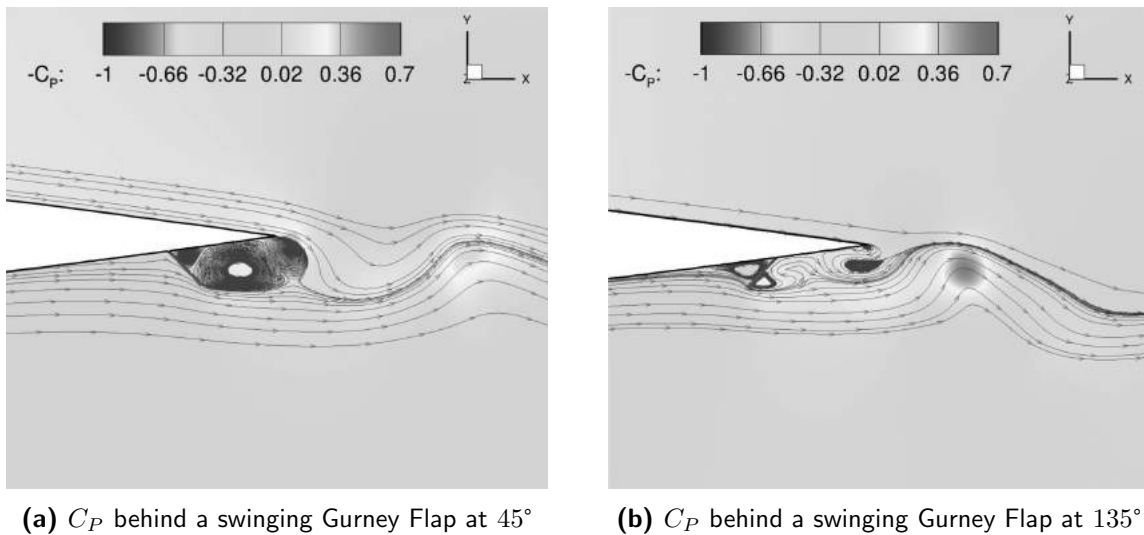
Figure 2.8: Pressure contours and streamlines of Gurney Flaps with $45°$ and $135°$ trailing edge angles [5]

and $6\%\,c$ case respectively. Furthermore, an increase in drag was also observed as the GF were mounted away from the trailing edge. Similarly, in an experimental analyses, Maughmer et

12

al. [29] observed a 10% drop in $C_{l_{max}}$ at $s = 10\% \, c$, which can be seen in figure 2.9b. Bach [28] carried out similar experiments on an AH93W174 wind turbine airfoil, also concluding that the placement of GF upstream from Trailing edge causes reduction in lift, as evident from figure 2.9a. In contraction with these findings, Chow et al. [32] claim that an optimal location in terms of L/D is around $95\% \, c$, however important to note is that this numerical study was conducted on dynamically deployed flaps. Active Gurney flaps that can be retracted into the airfoil are usually deployed around $90 - 95\% \, c$ location, which is a challenge, as limited space is available inside the aft of the airfoil [33]. That might explain this contradiction.

(a) ΔC_L as a function of the flap chord-wise location [28]

(b) $\Delta C_{L_{max}}$ for various GF heights at various locations [27]
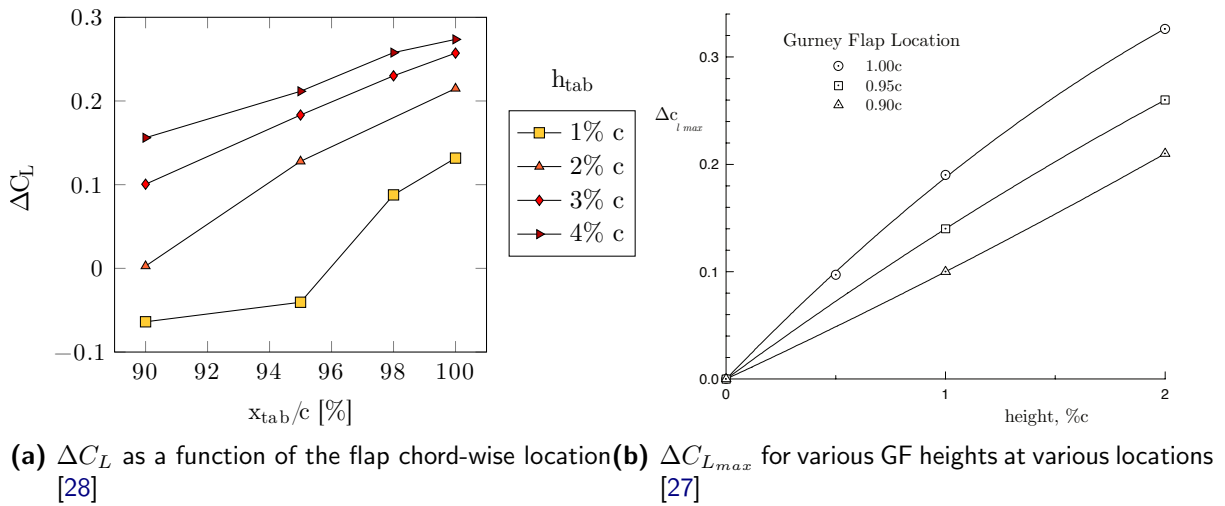
Figure 2.9: Effect on lift properties due to different chord-wise location of GF

2.2.4 Thickness

The thickness of the Gurney Flaps seems not to have any effect on the vorticity behind the flaps based on a CFD study carried out by Woogate et al. [31]. The analysis was done on a NACA23012M airfoil with $1.5\% \, c$ *(height)* Gurney flaps placed at $93.5\% \, c$ with a simulated flow of $M = 0.2$ and $Re = 0.5 \times 10^6$. The thickness of the Gurney was $0.25\% \, c$ for the thick flap and a block face thickness was considered for the virtual flap. The vorticity visualization from this study can be seen in figure 2.10.
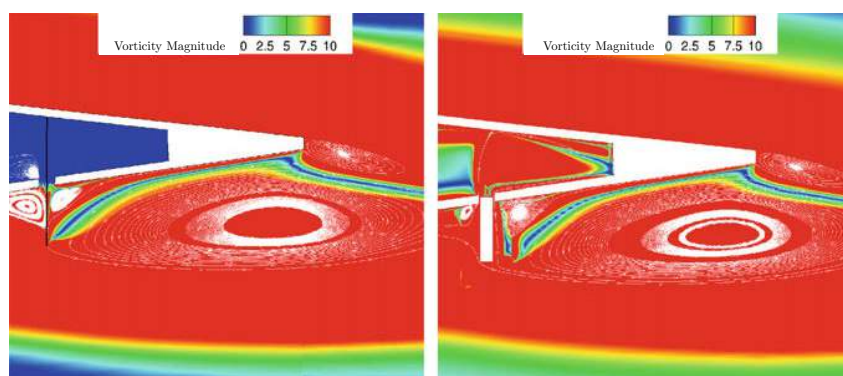
Figure 2.10: Vorticity magnitude visualization of NACA23012M airfoil with two different thickness Gurney flaps; *(left)* thin, *(right)* $0.25\% \, c$ thick [31]

2.2.5 Slitted and Serrated variations

As the lift increment comes at the cost of increase in drag, slitted and serrated variations of the GF have been tested to see if this effect can be minimized. van Dam et al. [34] conducted experimental investigation on serrated GF. The serrated GF had the same height but 50% frontal area that resulted in improved L/D performance, as can be seen in figure 2.11. Similarly, Mayda et al. [35] carried out an experimental study on the effects of slits and also found better L/D characteristics as shown in figure 2.12.
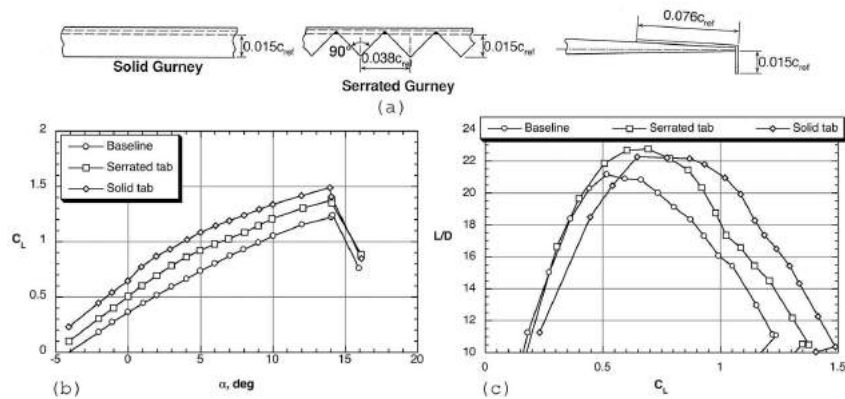
Figure 2.11: Geometric definition of the solid and serrated trailing edge flaps and comparison of their C_L and L/D ratio
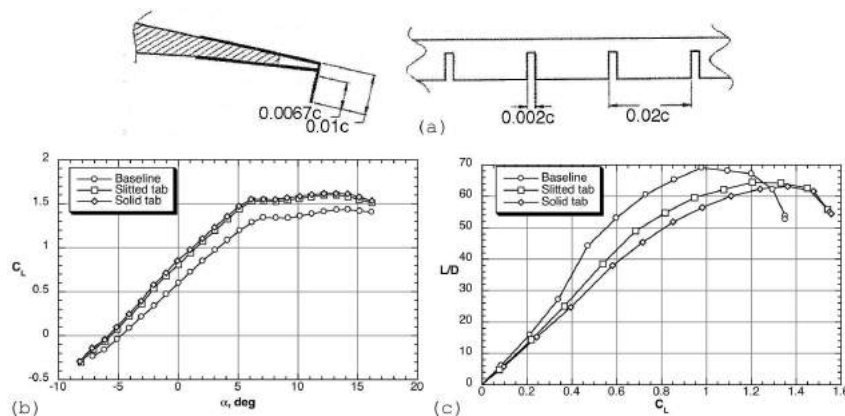
Figure 2.12: Geometric definition of the solid and slitted trailing edge flaps and comparison of their C_L and L/D ratio

2.2.6 Reynolds Number

A unique numerical research by Jain et al. [6] studied the effects of Reynolds number on the aerodynamics of airfoils with GF. They observed that performance of the airfoil without GF is influenced less than that of an airfoil with GF and as the Reynolds number is increased, lift increases while drag decreases. Further, for higher Reynolds number above the critical range, changes in the aerodynamic performance are negligible.
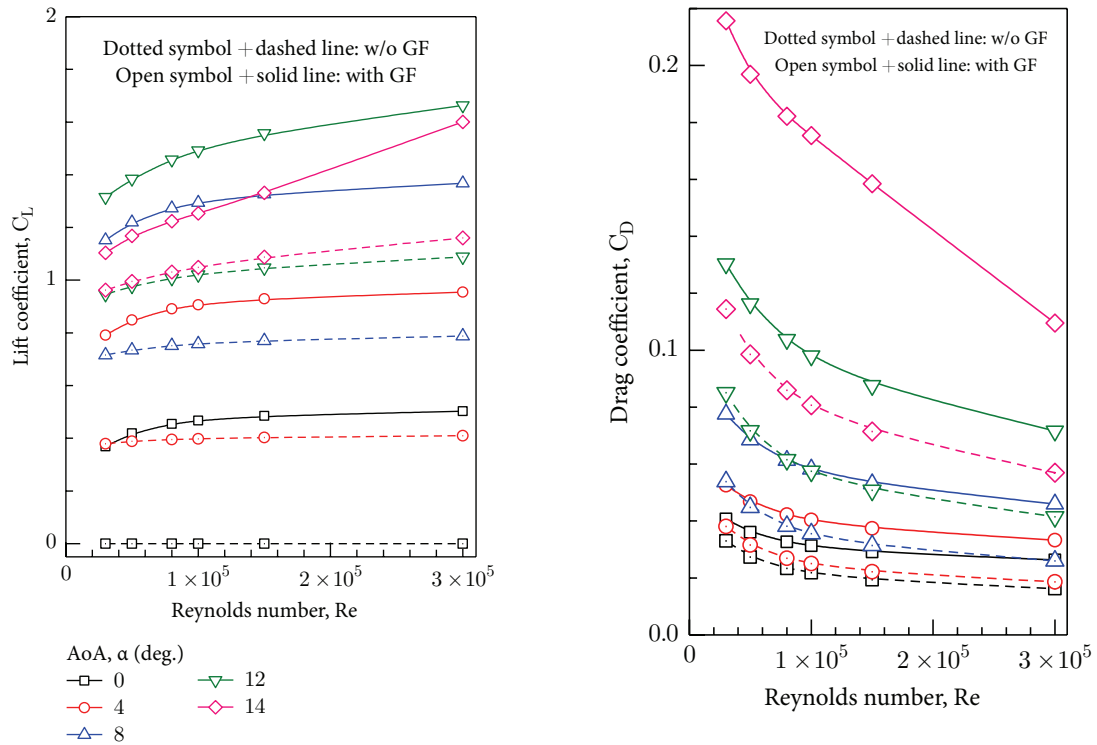
(a) C_L variation for different Reynolds number

(b) C_D variation for different Reynolds number

Figure 2.13: Effect of Reynolds number on C_L & C_D for NACA 0012 airfoil with and without $3\%\,c$ height GF [6]

2.2.7 Wedge fap

A variation of the trailing edge device is the wedge flap. Although it is not a Gurney flap by definition the working principles are quite similar [20] and therefore included here. The angle of the wedge flap is usually around $15° - 45°$ and the total height around $0.5\% - 1.5\%\,c$ [20], which are quite similar heights as used for GF. Doosttalab et al. [36] carried out a numerical study of the DU 91-W2-250 wind turbine airfoil developed at TU Delft. According to their analysis, both types of wedge flaps out performed the standard GF with the same height of $1\%\,c$, as shown in figure 2.14b. The standard GF produces a slightly higher C_L but due to higher drag is out performed by both wedge flap configurations as can be seen in figure 2.14a. From the two configuration of the wedge flaps, the curved turned out to have better aerodynamic enhancements.

Wedge flap

Divergent trailing edge | Curved wedge
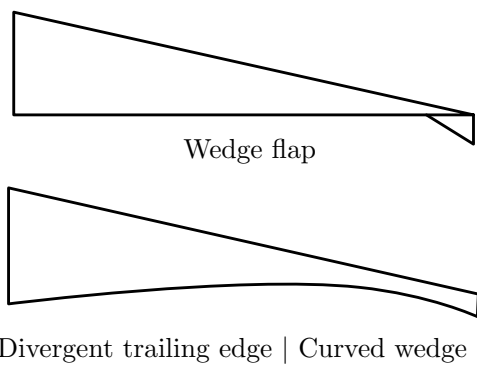
(a) The wedge flap and the curved wedge flap or divergent trailing edge [20]
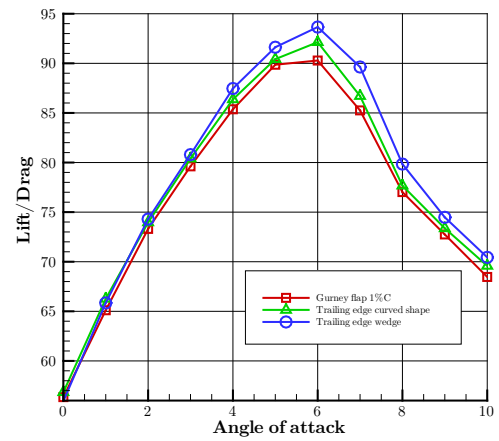
(b) L/D Comparison of standard GF with Wedge flap and curved shape wedge [36]

Figure 2.14: Different configurations of wedge flaps and L/D comparison with standard GF

16

2.3 Flow visualization techniques

To understand how fluids (air/water) interact with objects, it is extremely helpful to be able to visualize the flow, which can help not only get quantitative, but also qualitative information about the flow. This is especially needed for unsteady flows, which have a higher degree of complexity [37]. Air being a transparent medium, requires different techniques to achieve flow visualization. These include, surface oil, tufts, pitot tubes, hot-wire anemometry and laser Doppler velocimetry [38].

(a) Laser

(b) Oil-flow representation on a wind turbine blade [22]

(c) Tuft and Smoke

(d) Schlieren

(e) Laser Doppler velocimetry setup with Pressure Tubes

(f) Hot-wire (anemometer) velocity probe
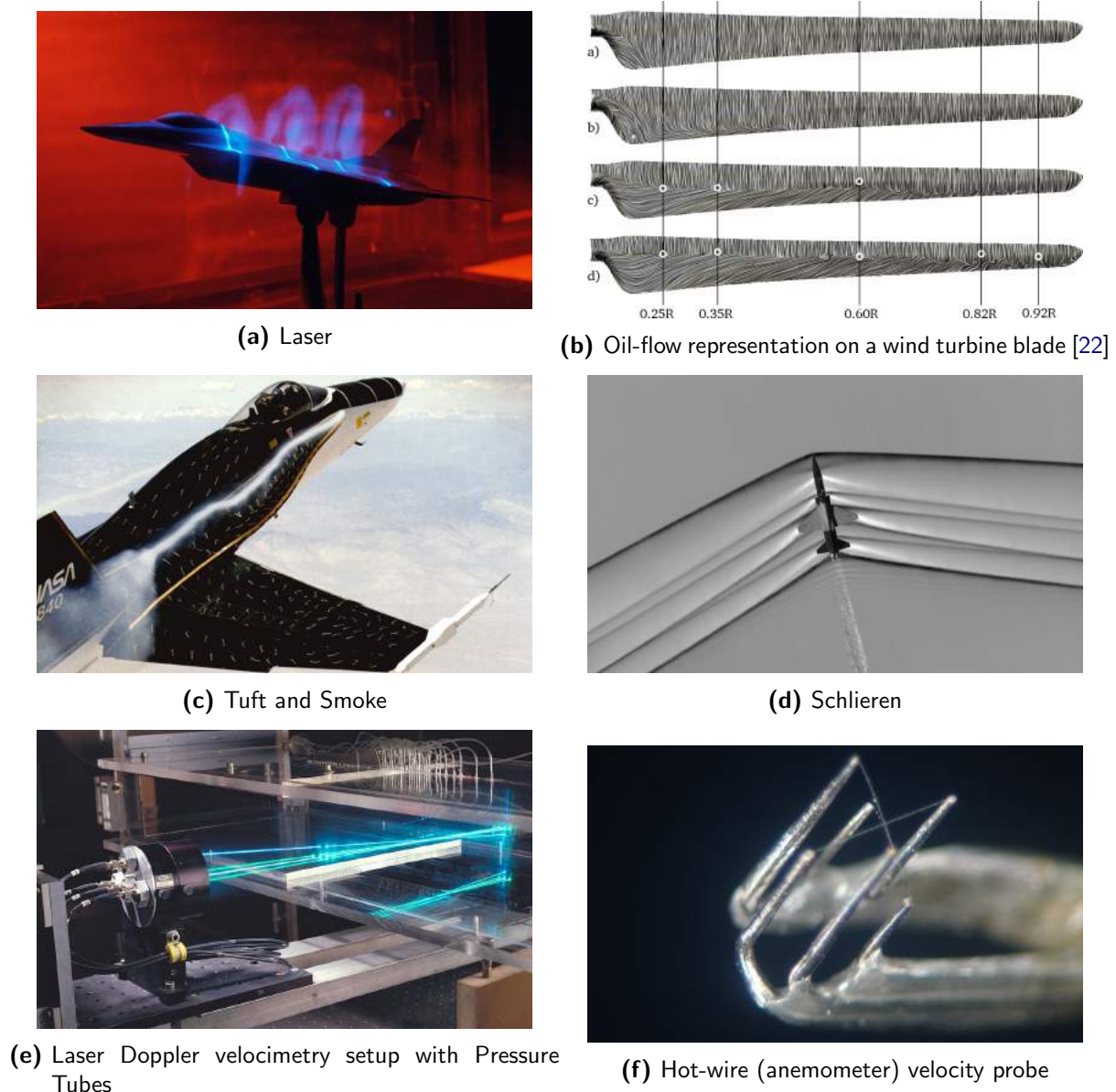
Figure 2.15: Different methods of Flow visualization and measurement techniques

Techniques like surface oil and tuft are applied directly to the surface being investigated, as shown in figures 2.15b and 2.15c, making the visualization process intrusive, while pitot tubes, hot-wire anemometry and laser Doppler velocimetry techniques are limited by their ability to

measure the velocity at a single point. Particle Image Velocimetry (PIV) on the other hand is an non-intrusive technique capable of producing two-dimensional or even three-dimensional vector fields. This technique and its various aspects will be discussed in the following section 2.4.

2.4 Particle Image Velocimetry

The birth of Particle Image Velocimetry (PIV) can be traced to the mid 1980s in Oldenburg and Göttingen, Germany [39]. The PIV technique involves the seeding of a transparent medium with tracer particles that reflect the light from a bright pulsating light source, usually a laser system. This reflected light is captured repeatedly over a short time interval and the analysis of succeeding images provides the displacement of groups of particles from which the velocity low field can be derived. The generalized PIV setup consists of light source, tracer particles, imaging camera and an image acquisition system [37].
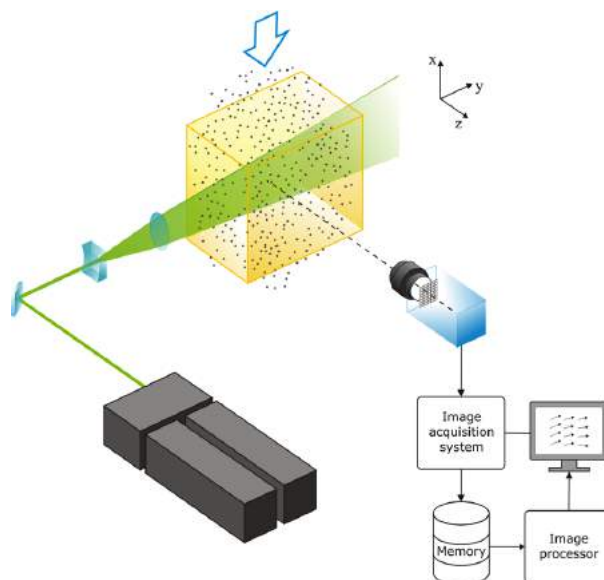
Figure 2.16: A sketch of Particle Image Velocimetry setup [38]

2.4.1 Tracer Particles

The PIV technique indirectly measures the flow velocity by measuring the displacement of tracer particles over Δt exposure time. Therefore the fluid dynamic properties of the tracer/seeding particles are important, as they should not influence the actual flow properties of the fluid and these particles need to be buoyant and small with respect to the fluid [37]. For air, this means that the seeding particles are generally around $5 - 200$ µm. As the images are generated from capturing light reflected from the particles, it is vital that they are highly reflective and scatter light as less as possible. These properties depend on the size and the refraction index of the particles. The size of the particles in combination with other properties must be able to achieve a $30 - 50\%$ exposure level [40].

2.4.2 Light Source

As mentioned in the introductory paragraph, lasers are generally used as the light source for PIV experiments. Stamhuis [41] explains the reason for this being the coherent and monochromatic nature of the light provided by lasers, which maintains a constant thickness without irregularities and diffusion. The light from the laser is converted into a laser light sheet using various optical arrangements to define the area that needs to be investigated. Lasers for PIV application can be categorized into two types; CW *(continuous weight)* and Pulsed lasers. CW as their name indicate, provide a continuous light which is of low power while the pulsed lasers provide a higher illumination with very short intervals, which are required for high speed experiments.

2.4.3 Imaging capturing

The light reflected from the particles is captured using Charged Coupled Device (CCD) or Complimentary Metal-Oxide Semiconductor (CMOS) devices after it has passed through a lens [7]. For standard 2D PIV, the optical axis of the camera is aligned perpendicular to the illuminated plane [42]. The focal length f, aperture number $f^{\#}$ and image magnification M_0 are the main defining properties of a lens, where, $f^{\#}$ is f divided by the aperture diameter and M_0 is the ratio between the image distance Z_0 and object distance z_0 [7].

2.4.4 PIV Image Post Processing

After the successful acquisition of images they need to be processed to generate the velocity fields. To make the computation process simple, the images are divided into smaller parts called *Interrogation Regions*, zones or windows. To determine the displacement of the particles during the time interval Δt from the two interrogation regions, as shown in figure 2.17, a Cross-correlation function ϕ is calculated as [38]:

$$\phi(m,n) = \frac{\sum\limits_{i=1}^{I}\sum\limits_{j=1}^{J} I(i,j) \cdot I'(i+m, j+n)}{\sqrt{\sum\limits_{i=1}^{I}\sum\limits_{j=1}^{J} I^2(i,j) \cdot \sum\limits_{i=1}^{I}\sum\limits_{j=1}^{J} I'^2(i,j)}} \tag{2.2}$$

For a good cross-correlation, both interrogation regions I and I' need to contain the same particles. This requires the optimization of the correlation window size, as a small size will result in wrong velocity vectors while a larger size will lower the resolution of the flow field [43].

Another method to improve the quality of the data for processing is Overlapping. The particle close to the edges of the interrogation regions are missing in the $t + \Delta t$ window, which depending on the flow velocity have moved out of the region. Overlapping helps recover these "missing" particles so that their displacements can also be calculated. Adrian [44] has specified an general overlapping of 50%.

2.5 Stereoscopic Particle Image Velocimetry

Conventional two-dimensional PIV can be used to extract the out-of-plane velocities, however, the vectors obtained from such an analysis are randomly distributed and possess extremely low
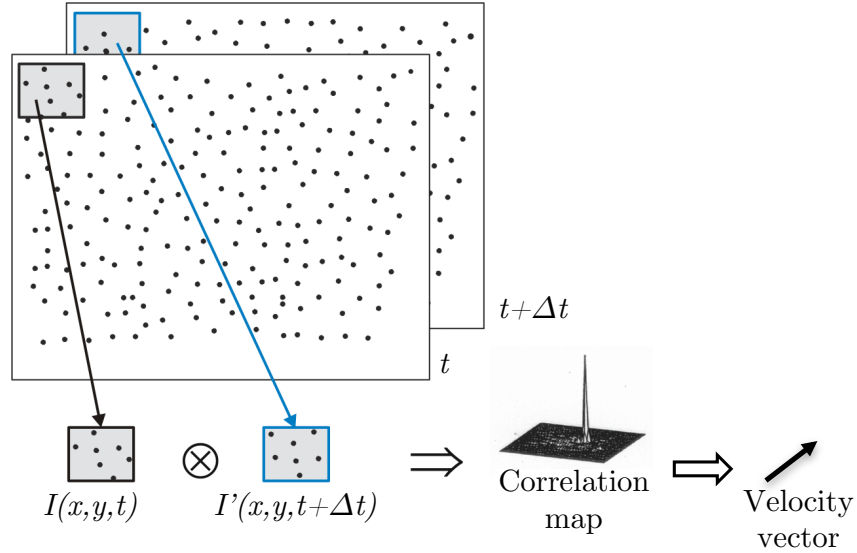
Figure 2.17: Cross-correlation map from two interrogation regions taken at t and $t + \Delta t$ [38]

spatial resolution [42]. These problems are overcome by using two cameras which provide enough information to calculate the third out-of-plane component of the velocities. This variation of PIV is known as Stereoscopic Particle Image Velocimetry (SPIV).

2.5.1 Set-up

Two basic setups for SPIV have been defined by Adrian et al. [42] and Prasad et al. [45], namely the *translation method* and the *angular displacement method*, as shown in figure 2.18. The translation method has the advantage that the magnification from both the cameras is constant as they are at the same distance from the object plane, however, this method has two major shortcomings. SPIV require both cameras to capture the object plane due to the physical limitation of the setup, as can be seen in figure 2.18a, only a small overlap can be achieved, in other words, a maximum viewing angle of 15° [7]. Another disadvantage is that the off-axis images can easily get out of focus.

The angular displacement method on the other hand, as depicted by figure 2.18b, allows larger viewing angles. However, this comes at the cost of magnification not being constant, which causes perspective deformation of the image as shown in figure 2.20. Higher angles increase the accuracy of the out-of-plane components, but Prasad et al. [42] suggest a $30° - 50°$ inclination angle, as increasing the angle further comes at the cost of magnification distortions. This is also evident from equation 2.3, where the inverse relation between the out-of-plane displacement and the angle α *(between image plane & lens plane)* can be observed, where $\sigma_{\delta x}$ & $\sigma_{\delta z}$ are the errors of the in and out-of-plane vectors.

$$\frac{\sigma_{\delta z}}{\sigma_{\delta x}} = \frac{1}{\tan \alpha} \tag{2.3}$$

(a) The translation method   **(b)** The angular displacement method
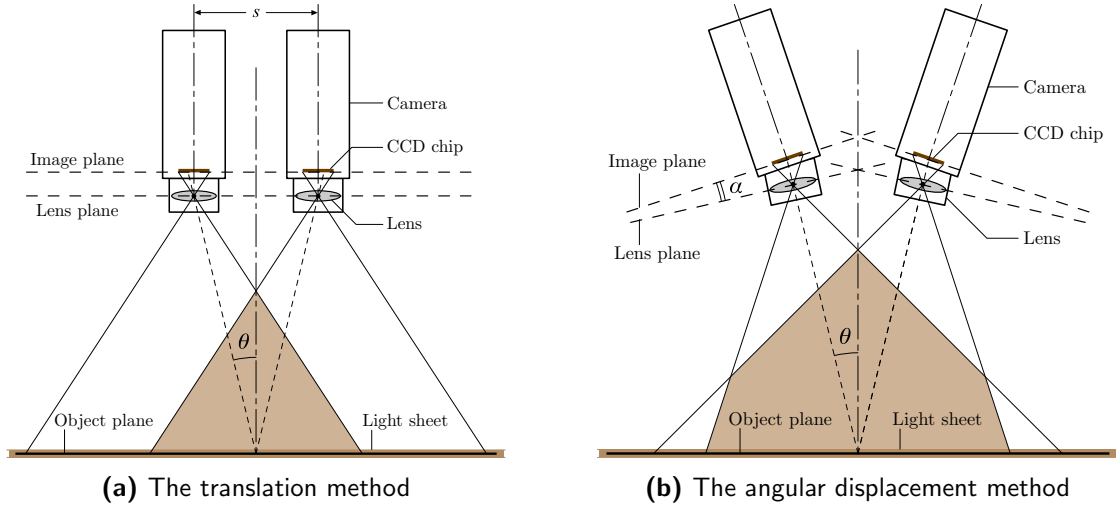
Figure 2.18: Optical setups for SPIV [7]

2.5.2 Scheimpflug condition

To take advantage of the wide viewing angles of the angular displacement method and to overcome its challenges, the Scheimpflug condition can be applied. As the cameras are deployed at an angle, the object plane and the lens plane are not parallel and hence only a small region will be in focus. The Scheimpflug principle works by rotating the lens plane to increase the area that is in focus, as can be seen in figure 2.19. The nominal image magnification M_0 defined for the optical axis of the Scheimpflug condition is given by equation 2.4, where θ is the angle between the lens and object plane [40].

$$M_0 = \frac{\tan\alpha}{\tan\theta} \tag{2.4}$$

(a) Angle displacement arrangement with Scheimpflug [46].   **(b)** Detail of the Scheimpflug condition [7]
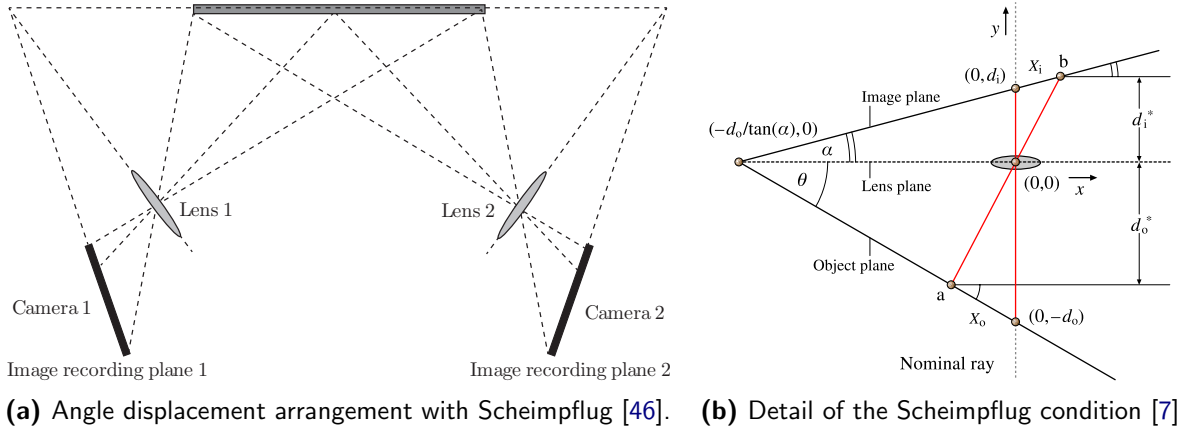
Figure 2.19: Scheimpflug condition

2.5.3 Calibration

As figure 2.19a shows that the cameras are mounted at an angle. This causes the images to have a perspective, as can be seen in figure 2.20. In order to correct for these distortions and

moreover to be able to cross-correlate the images from two cameras, a calibration is carried out. A target is placed in the object plane; usually a plate with dots and ridges.
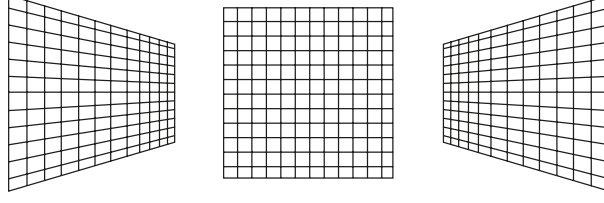
Figure 2.20: The perspective view from the cameras in the angle displacement arrangement [46].

2.5.4 Displacement components reconstruction

Hu [46] has detailed a method for the reconstruction of the displacement components of the particles from an angle displacement arrangement. A schematic overview with notations can be observed in figure 2.21 where two cameras are placed at $L1$ and $L2$. The cameras are observing the $X - Y$ plane while the Z axis points towards the cameras, i.e. the out-of-place component. For this setup, the displacement vectors can be calculated using equations

$$dx = \frac{dx_2 \tan \alpha_1 - dx_1 \tan \alpha_2}{\tan \alpha_1 - \tan \alpha_2} \tag{2.5}$$

$$dy = \frac{dy_2 \tan \beta_1 - dy_1 \tan \beta_2}{\tan \beta_1 - \tan \beta_2} \tag{2.6}$$

$$dz = \frac{dy_2 - dy_1}{\tan \beta_1 - \tan \beta_2} \tag{2.7}$$

For a case where β_1 and β_2 become extremely small, i.e. the cameras are right next to each other *(or the same location)* and perpendicular to the laser sheet, the $\tan \beta_1$ and $\tan \beta_2$ also approach zero. This means that dz will not be able to be calculated for such a case and solving the equation for such a case will result in:

$$dy = \frac{dy_1 + dy_2}{2} + \frac{dx_1 + dx_2}{2} \cdot \left(\frac{\tan \beta_2 - \tan \beta_1}{\tan \alpha_1 - \tan \alpha_2} \right) \tag{2.8}$$

2.6 Pressure and Load calculation from PIV/SPIV

Imaichi and Ohmi [47] proposed using the Navier-Stokes equations for the two-dimensional case, as given by equations 2.9 & 2.10, to calculate the pressure distribution numerically by the integration of these equations. However, they observed problematic results in certain cases as these equations have been simplified to neglect the unsteady terms. Therefore, this can be only used for two-dimensional, incompressible and steady flows cases with accuracy.

$$u \frac{\partial u}{\partial x} + v \frac{\partial u}{\partial y} = -\frac{1}{\rho} \frac{\partial p}{\partial x} + \nu \left(\frac{\partial^2 u}{\partial x^2} + \frac{\partial^2 u}{\partial y^2} \right) \tag{2.9}$$
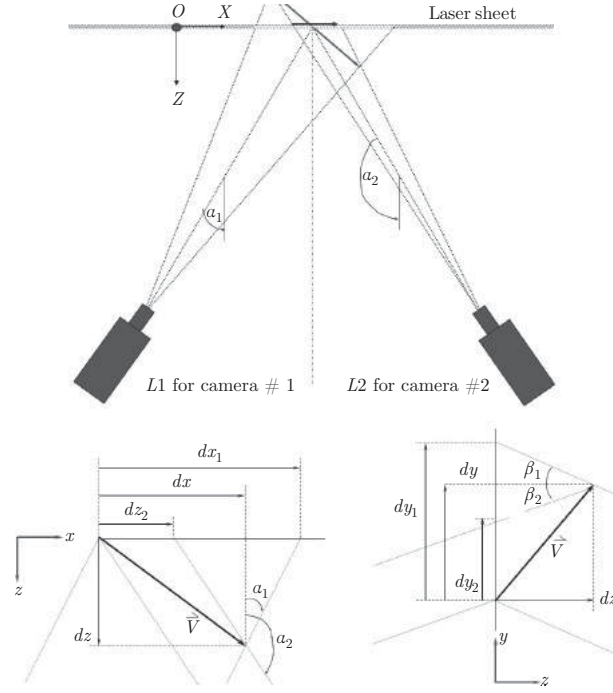
Figure 2.21: An overview of steps required to reconstruct the three-dimensional displacement components [46]

$$u\frac{\partial v}{\partial x} + v\frac{\partial v}{\partial y} = -\frac{1}{\rho}\frac{\partial p}{\partial y} + \nu\left(\frac{\partial^2 v}{\partial x^2} + \frac{\partial^2 v}{\partial y^2}\right) \tag{2.10}$$

For more complex flow conditions, Noca et al. [48] proposed using the control volume approach. The control volume approach isolates a section of the flow around an object; airfoil in case of a scaled wind turbine blade *(figure 2.22)* to extract the aerodynamic forces from the change in momentum of the flow inside the pre-defined control volume. Airfoil in flow, experiences aerodynamic forces that are caused by surface pressure distribution and viscous shear stresses. Therefore, this method offers a simpler approach to calculate these loads which are given by equation 2.11, derived by Campo et al. [49] for calculations of loads for a PIV analysis on a scaled wind turbine blade.
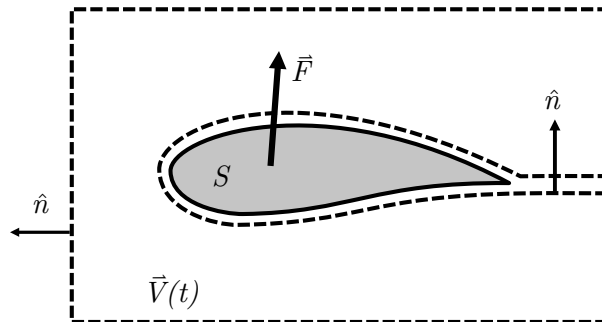
Figure 2.22: Control volume approach based on Noca et al. [48] for an airfoil

$$\vec{F}_{\text{flow}\Rightarrow\text{airfoil}} = -\frac{d}{dt}\iiint_v \rho\vec{V}_r dv - \iint_S p\vec{n}ds + \iint_S \bar{\bar{\tau}}'\vec{n}ds - \iint_S \rho\left(\vec{V}_r\cdot\vec{n}\right)\vec{V}_r ds$$
$$-\iiint_v 2\rho\left(\vec{\Omega}\times\vec{V}_r\right)dv - \iiint_v \rho\left(\vec{\Omega}\times\left(\vec{\Omega}\times\vec{r}\right)\right)dv \tag{2.11}$$

As the frame of reference does not move with respect to the blade airfoil, the time-derivative becomes redundant. Further, Coriolis force and Reynolds stress are added to account for the non-inertial nature of the frame of reference. After all of this, the final equation 2.12 is obtained by Campo et al. [49], which can be used for calculations of in- and out-of-plane velocity fields.

$$\begin{bmatrix}F_x\\F_y\end{bmatrix} = \overbrace{\int_V \mu\begin{bmatrix}2\frac{\partial u}{\partial x} & \left(\frac{\partial u}{\partial y}+\frac{\partial v}{\partial x}\right)\\ \left(\frac{\partial u}{\partial y}+\frac{\partial v}{\partial x}\right) & 2\frac{\partial v}{\partial y}\end{bmatrix}\vec{n}ds - \frac{d}{dz}\iint_S \mu\begin{bmatrix}\left(\frac{\partial u}{\partial z}+\frac{\partial w}{\partial x}\right)\\ \left(\frac{\partial u}{\partial y}+\frac{\partial v}{\partial x}\right)\end{bmatrix}}^{\text{Viscous forces}}$$

$$\overbrace{-\int_V \rho\begin{bmatrix}uu & uv\\ uv & vv\end{bmatrix}\vec{n}ds - \frac{d}{ds}\iint_S \rho\begin{bmatrix}uw\\ vw\end{bmatrix}dxdy}^{\text{Convective acceleration}} \tag{2.12}$$

$$\overbrace{-\int_V \rho\begin{bmatrix}u'u' & u'v'\\ u'v' & v'v'\end{bmatrix}\vec{n}ds - \frac{d}{ds}\iint_S \rho\begin{bmatrix}u'w'\\ v'w'\end{bmatrix}dxdy}^{\text{Reynolds Force}}$$

$$\overbrace{-2\iint_S \rho\begin{bmatrix}-\Omega w\\ 0\end{bmatrix}dxdy}^{\text{Coriolis Force}}\quad \overbrace{-\int_V \begin{bmatrix}p & 0\\ 0 & p\end{bmatrix}\vec{n}ds}^{\text{Pressure Force}}$$

A similar approach can be utilized for pressure data calculations, where the momentum equation in differential form is given by,

$$\nabla p = \frac{d}{dt}\left(\rho\vec{V}_r\right) - \rho\vec{V}_r\cdot\nabla\vec{V}_r + 2\rho\left(\vec{\Omega}\times\left(\vec{\Omega}\times\vec{r}\right)\right) = \mu\Delta\vec{V}_r \tag{2.13}$$

The calculation of the pressure makes use of multiple space matching algorithms which incurs errors. To minimize this error, pressure data is calculated using a forcing function $g(u,v)$, which leads to,

$$\nabla^2 p \approx D\rho = g(u,v) \Rightarrow p = D^{-1}g(u,w) \tag{2.14}$$

Where the forcing function can finally be defined as,

$$D\rho = \left[\frac{p_{(i+1,j)} - 2p_{(i,j)} + p_{(i-1,j)}}{\Delta x^2} + \frac{p_{(i,j+1)} - 2p_{(i,j)} + p_{(i,j-1)}}{\Delta y^2}\right] \tag{2.15}$$

Part II

Method

Chapter 3

Model
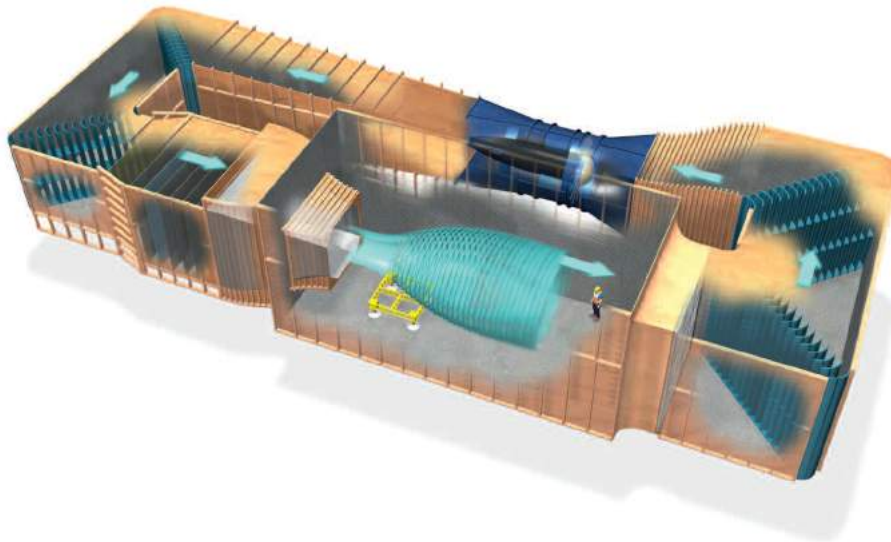
3.1 Wind Tunnel

Figure 3.1: A schematic of the Open Jet Facility (wind tunnel) at the Delft University of Technology

The load measurements and the SPIV experiments were both carried out at the Open Jet Facility (OJF) of the Delft University of Technology. The OJF is a closed loop wind tunnel capable of achieving speeds of up to $35\mathrm{m\,s}^{-1}$. The test section is located in a large room with a width of 13m and a height of 8m. The wind flow is achieved by a large fan that is driven by a 500kW rated electric engine. The fan propels the flow through diffuser and it is guided through two rows of corner vanes in order to rotate the flow 180°. Just before entering the test section the flow is passed through settling chamber which contains wire meshes to reduce

velocity deviations and turbulence. The flow exits through an octagonal 2.85m × 2.85m opening. A part of this exit can be seen in figure 4.1.

At the end of the test section, the flow is cooled by a huge 350kW radiator system to remove the added heat in the flow. In the empty space just after the radiator, a smoke/fog generator can be placed for PIV experiments, this way the fog/smoke can get evenly mixed in the flow and provide better experimental results. The flow is finally passed again through two rows of corner vanes to rotate the flow back towards the fan and completing the loop.

3.2 Turbine Model

The turbine that was used during the experiments has been manufactured by DEMO (Dienst Elektronische en Mechanische Ontwikkeling - *translation: development and construction of unique experimental set-ups and prototypes*) of the Delft University of Technology. Figure 4.2 shows the inside of the load measuring mechanism that is covered by a black, plastic cone during experiments for aerodynamic considerations. This model is fitted with a motor which can be driven at the desired speed, rotations per minute [rpm]. The Turbine has attachment points for two blades and has been used at TU Delft for many experiments, including the experiment that was the subject of this article [2].
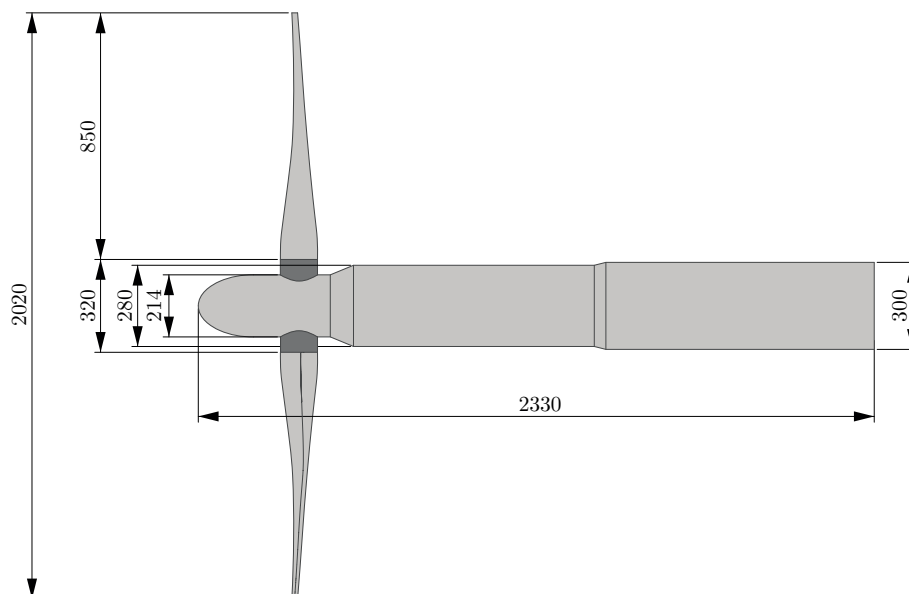
Figure 3.2: Top view with detailed dimensions of the wind turbine model with the blades parallel to the ground. All dimensions are in mm.

3.3 Blade

The blades of the scaled Horizontal axis wind turbine model were based on Nordex N80 wind turbine blades. These turbines are in use by ECN *(now part of TNO)* at their Wind Turbine

Test Site Wieringermeer. The blades of these turbines are produced by LM Wind Power and have the designation LM388.

The primary focus of the experiments was the root region. In order to keep this region from getting too small only $0 - 0.618\ r/R$ of the reference blade was used to design the model blade. This was also necessary to have a sufficiently thick connection at the root to the turbine model for safety. A detailed comparison of the actual blade and the modeled blade can be seen in table 3.1. The values that have been greyed-out under the dashed line are only of the actual blade and not considered for the model. The model is therefore $\sim 3.54\%$ scale of the actual blade.

The various airfoils that form the different sections of the blade, except for the cylindrical root section, are give in figure 3.3. The aerofoils under the dashed-line in the figure, namely, NACA 63418 and NACA 63415, are not part of the model as these airfoils are the section profiles of the part of actual blade that was "chopped-off", as explained in the preceding paragraph. It should also be noted that the sections loft from one airfoil to the next in order to form the continuous shape of the blade. Therefore, the exact shape in-between the sections are 'transitional-aerofoils'. The precise profiles at each r/R are given in figure A.5.

Table 3.1: Comparison of the actual LM388 blade with the scaled shortened blade used for experiments. Note, the r values exclude the hub region

r LM388 [m]	r model [m]	c LM388 [m]	c model [m]	Twist [deg]	Thickness %	Section airfoil
0	0	2.42	0.1286	0	99.99	Cylinder
1.88	0.0666	2.48	0.1317	5.37	96.41	Cylinder
4	0.1417	2.65	0.1408	6.69	80.53	Cylinder
6	0.2125	2.81	0.1493	7.9	65.08	DU-W-405LM
8	0.2833	2.98	0.1583	9.11	51.67	DU-W-405LM
10	0.3542	3.14	0.1668	10.1	40.3	DU-W-405LM
12	0.425	3.17	0.1684	9.39	32.53	NACA-63424
14	0.4958	2.99	0.1588	7.16	28.4	NACA-63424
16	0.5667	2.79	0.1482	5.45	25.62	NACA-63424
18	0.6375	2.58	0.1371	4.34	23.77	NACA-63424
19.2	0.68	2.46	0.1307	3.84	22.86	NACA-63421
22	0.7792	2.21	0.1174	2.86	20.99	NACA-63421
24	0.85	2.06	0.1094	2.31	20.03	NACA-63421
26		1.92		1.77	19.4	NACA-63418
28		1.8		1.28	19.03	NACA-63418
30		1.68		0.9	18.79	NACA-63418
32		1.55		0.55	18.6	NACA-63418
34		1.41		0.23	18.39	NACA-63418
36		1.18		0.03	17.95	NACA-63415
37		0.98		0.02	17.39	NACA-63415
38		0.62		0.93	16.33	NACA-63415
38.4		0.48		2.32	15.7	NACA-63415
38.8		0.07		6.13	14.84	NACA-63415
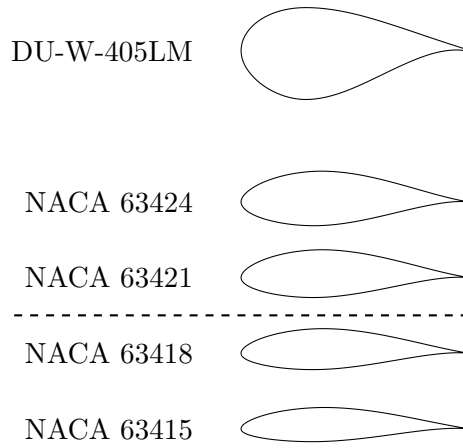
Figure 3.3: Airfoil profiles that form the different sections of the blade
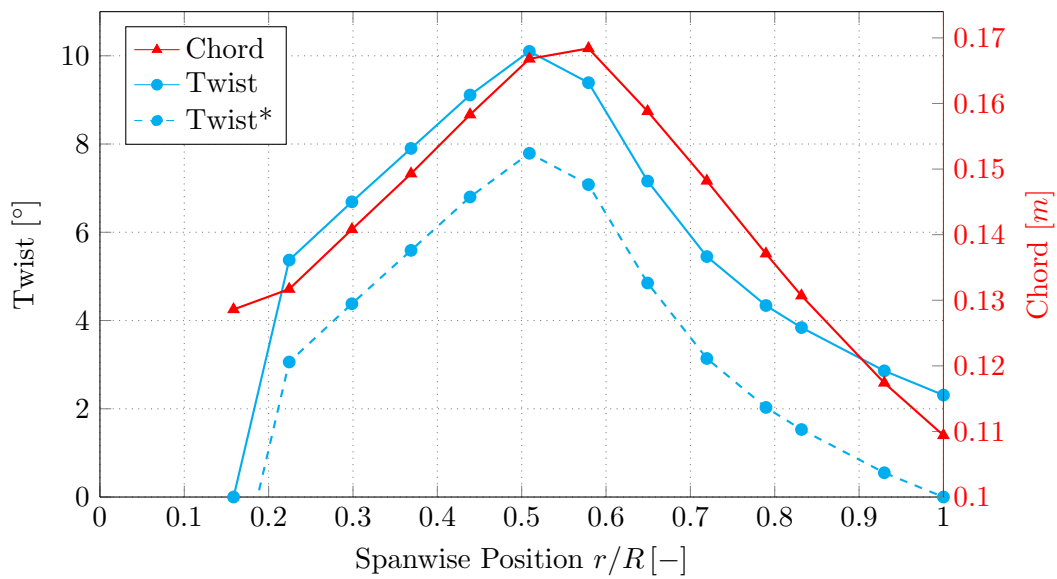
Figure 3.4: The Chord and twist distribution along the blade span

3.3.1 Blade manufacturing imperfections

The blade was milled from the Sika Block M930 material. This material is provided in blocks with a maximum thickness of 75mm. As the thickness of the model blade at the root (128.7mm) exceeds this thickness, two slabs were glues together before the blades were milled. Figure 3.5a shows the part of the model that exceeds the thickness of the Sika Block. This process of manufacturing however resulted in small air-pockets that are visible along the joining line, as show in figures 3.5c, 4.7 and 4.8.

Also, there was a little bump on the blade that was the result of exporting from the CAD program, as can also be seen on the blade in figure 4.7

Furthermore, the blade is mounted to the hub on two rods that stick-out of the hub. These rods also need to covered up. In order to do this a CAD program was used to design a *"Hub-blade connecting part"*, see figure 3.6a. This part was also milled but instead of Sika Block a simple hard foam was used. This was necessary as this part could not be bolted/or properly installed

to the blade and therefore taking safety into account a light material was used. Due to the manufacturing process, the connecting part was not a perfect fit and there was a slight gap towards the end which was closed using duct tape. Also, connecting part was slightly larger than the diameter of the Sika block blade as can be observed in figure 3.6b.
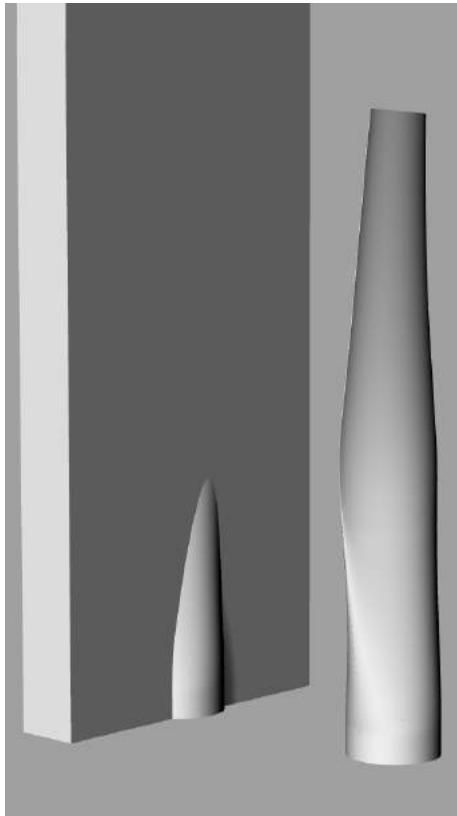
(a) Block superimposed on the blade.
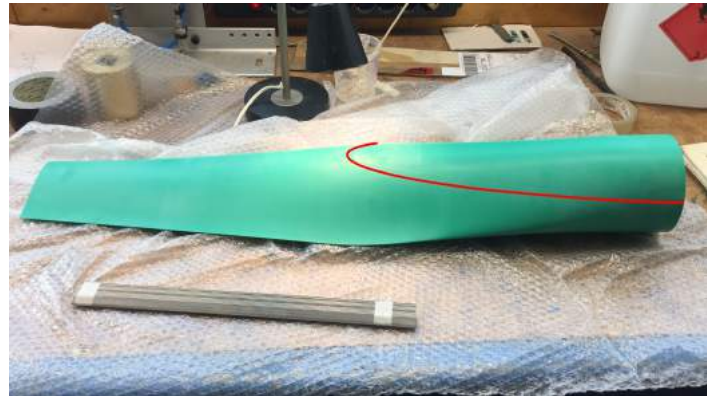
(b) The joining line indicated with a red line.
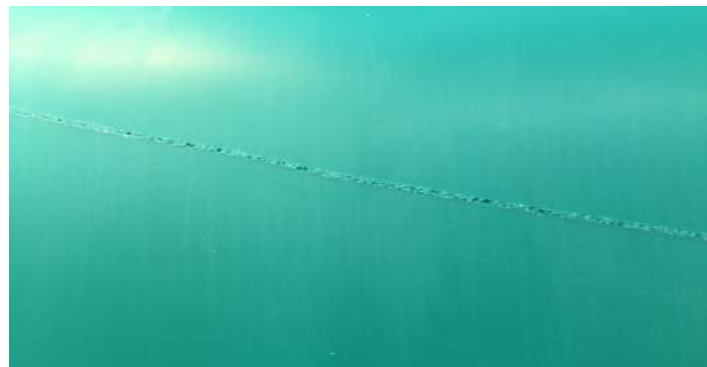
(c) Zoomed in view of the joining line.

Figure 3.5: The joining line on the blade due manufacturing process shown on the unpainted blade.
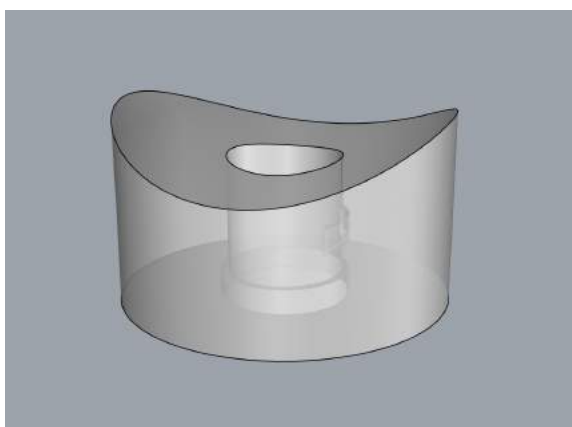
(a) CAD model of the hub-blade connecting part
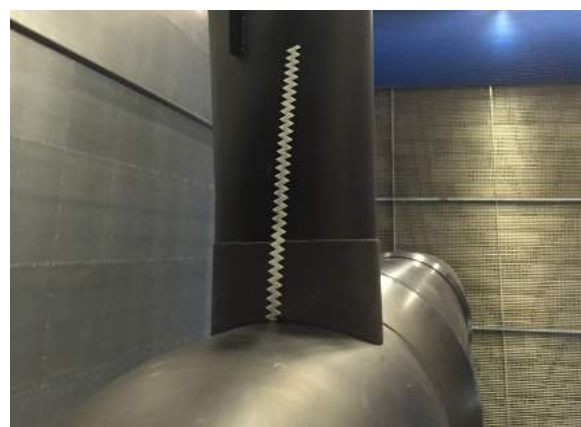
(b) Hub-blade connecting part installed on the blade

Figure 3.6: Hub-blade connecting part

3.4 Flaps models

To understand the effects of height and different shapes of flaps, three configuration were used. These can be seen in figure 3.7. Flap 1 *(also represented by the symbol ∟)* and flap 2 *(also represented by the symbol ∠)* where both made of bend metal strips of 0.8mm thickness. Flap 3 *(also represented by the symbol △)* was made of hard styrofoam, namely BASF's Styrodur. The design was cut of the foam sheet using a hot-wire cutting machine. A CAD drawing of the flap profile was loaded into the software of the machine, which it followed while cutting the foam. Due to melting, age and simplicity of the machine there were minor variations and the edges where curved as a result. The design and shape of the flap △ is that of a wedge flap which was has already been briefly discussed in section 2.2.7. The dimensions given in figure 3.7 are the averaged measured dimensions of the flaps that were produced and used.

All flaps where cut into 40mm sections to accommodate for the curvature of the blade. This length was however not enough as will be discussed in section 4.4. The flaps where all painted black to lower reflection and double-sided tape with a thickness of 0.15mm was used to attach the flap to the blades.
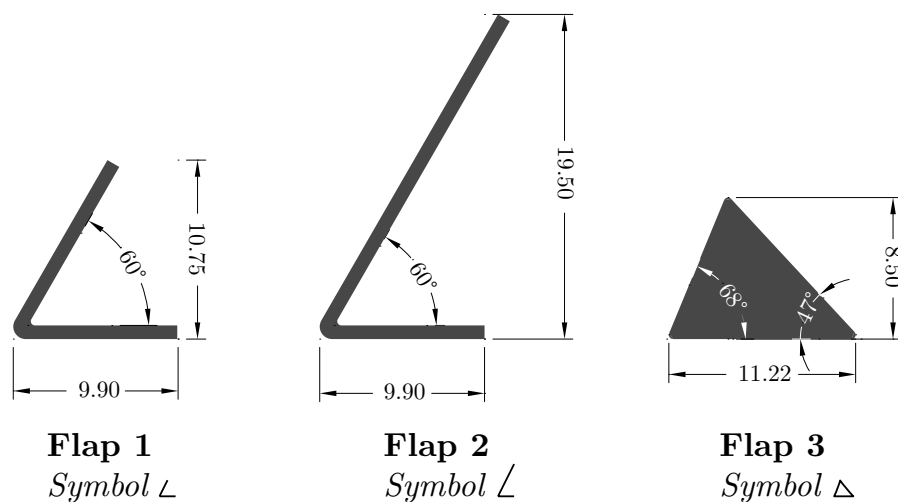
Figure 3.7: Detailed dimensions of the three flaps that were used for the experiment. All linear dimensions are in millimeters [mm], while angles are given in degrees [^{o}].

3.5 Zigzag tapes

In order to compensate for the low Reynolds number when comparing to the full scale turbine and to have the flow behave similarly on the blades, zigzag tapes (a.k.a. tripping wire) were used. Two different types of zigzag tapes were used to effectively influence the flow on the blade. Figure 3.8 shows the detailed measured dimensions of the tapes that were used. The tapes included adhesive tape on one side and were extremely easy to apply. The tapes are made of white plastic with a glossy finish. The 5.3mm tape had a thickness of 0.25mm while the wider 11mm tape had a thickness of 0.45mm.
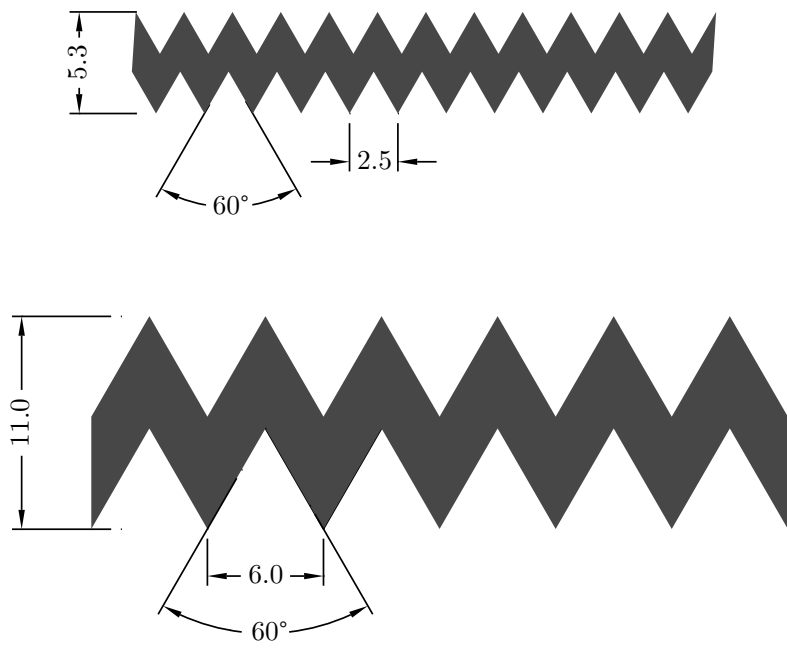
Figure 3.8: The dimensions in [mm] of the zigzag tapes that were used on the blade

Chapter 4

Experimental set-up

The experiment was divided into two parts. Firstly, the forces on the wind turbine were measured with three different types of flaps at three different chord-wise locations and of course the clean, i.e. no flap configurations. Secondly, the stereoscopic-PIV experiments were carried out for one selected case, namely the flap △ at 95% chord location. The choice of the sequence was due to the fact that the PIV required more preparation and a bigger set-up.

4.1   Aligning of the turbine

One of the first steps before the experiments could start was the correct alignment of the turbine model in the wind tunnel. This was needed to ensure that the turbine will be directly in-line with the flow. The wind turbine model was installed on a large platform that could be moved on the floor of the wind tunnel and the height of this platform could be adjusted within a certain range. For the alignment, a 3-plane leveling laser was used and the exit of the wind-tunnel was used as the reference, as the exit mainly determines the direction of the flow. This alignment process can be seen in figure 4.1.

4.2   Calibration of the measurement system

The wind turbine model used for the experiment uses electric strain gauges to measure the forces which can then be translated to torque and thrust. Before starting the experiments, the model was calibrated to ensure that the measured values correspond correctly with the actual values. The calibrations were carried out in both the axial and the tangential directions. The model was loaded with known weights after which the output strain values were measured and plotted. The set-up for the calibration can be seen in figure 4.2. The calibrations for the axial and tangential directions were carried out separately.

The graphs generated from the measured strains during the calibration can be seen in figures 4.3 and 4.4. The model measurement system uses two sets of strain gauges for both directions and the values measured are therefore categorized as strain gauge 1 and strain gauge 2.
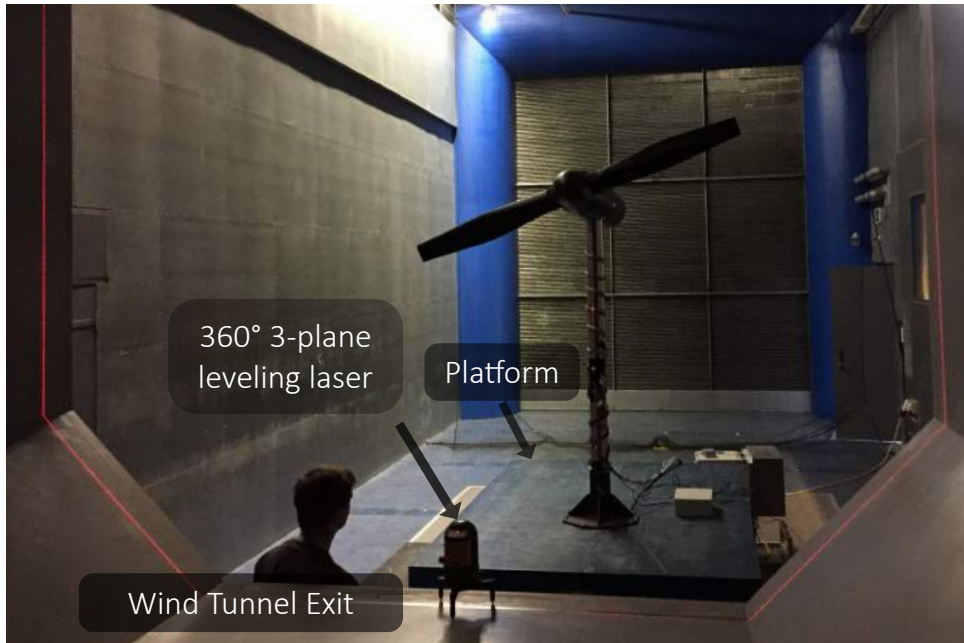
Figure 4.1: The alignment of the wind turbine model mounted on the platform using a 3-plane levelling laser
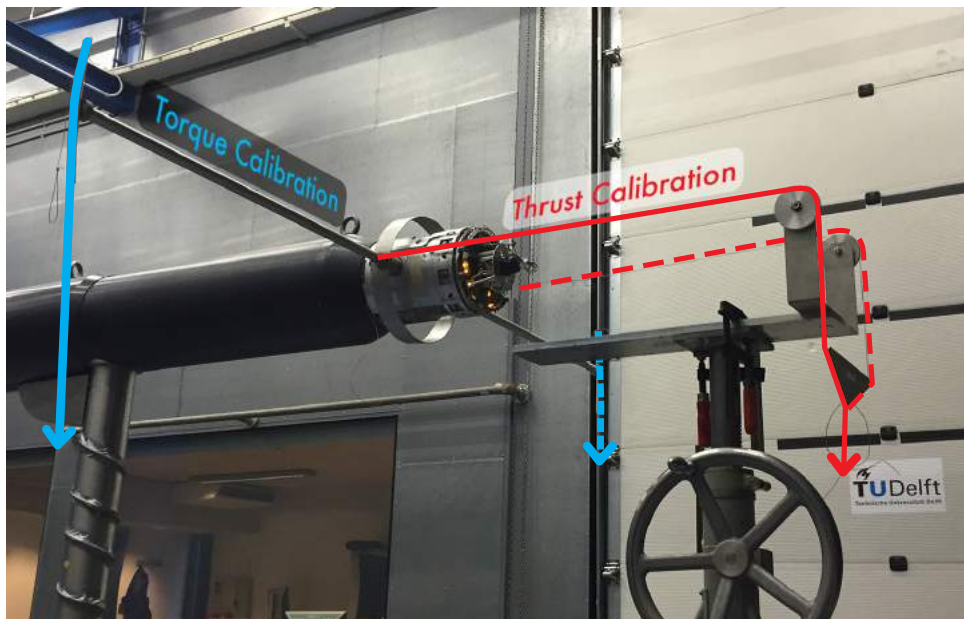
Figure 4.2: The set-up for the calibration of the test model

4.3 Pitch Determination

The blades are mounted manually on the hub and each blade can be pitched individually during the mounting process. To ensure correct pitch angle during mounting, a technique was improvised which involved using a 3D printed mold. This mold was generated from the original 3D model of the blade to ensure accuracy and had straight horizontal and vertical edges. The 3D-printed mold was placed on the tip of the blade and the straight edge used as a reference
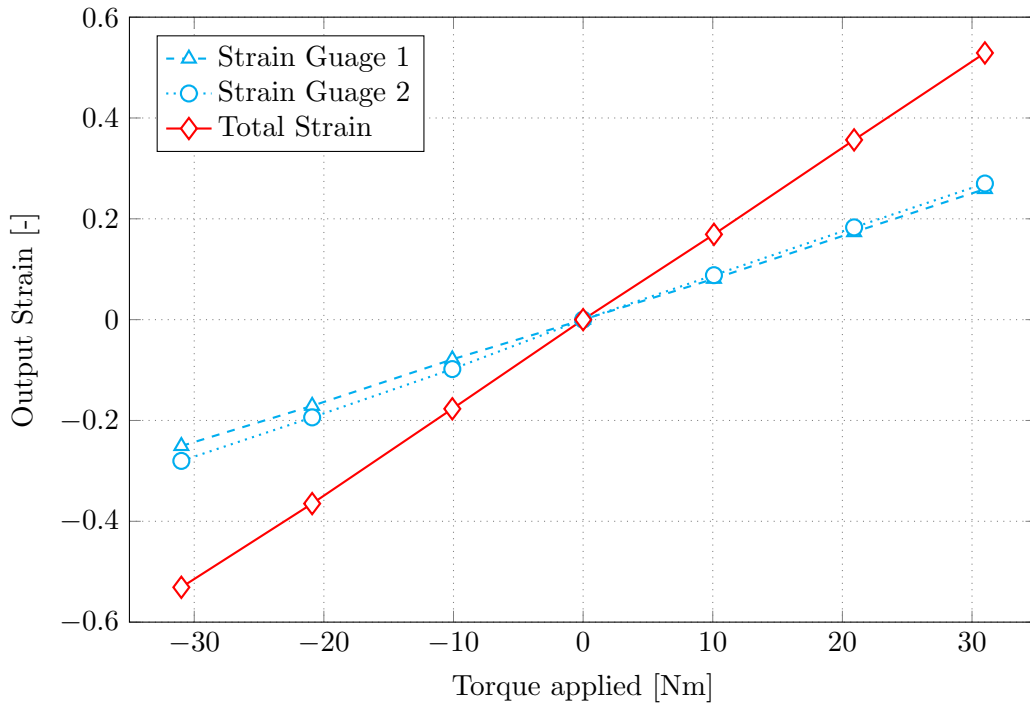
Figure 4.3: The measured strain results from the system loaded with pre-determined tangential load for torque calibration of the test model
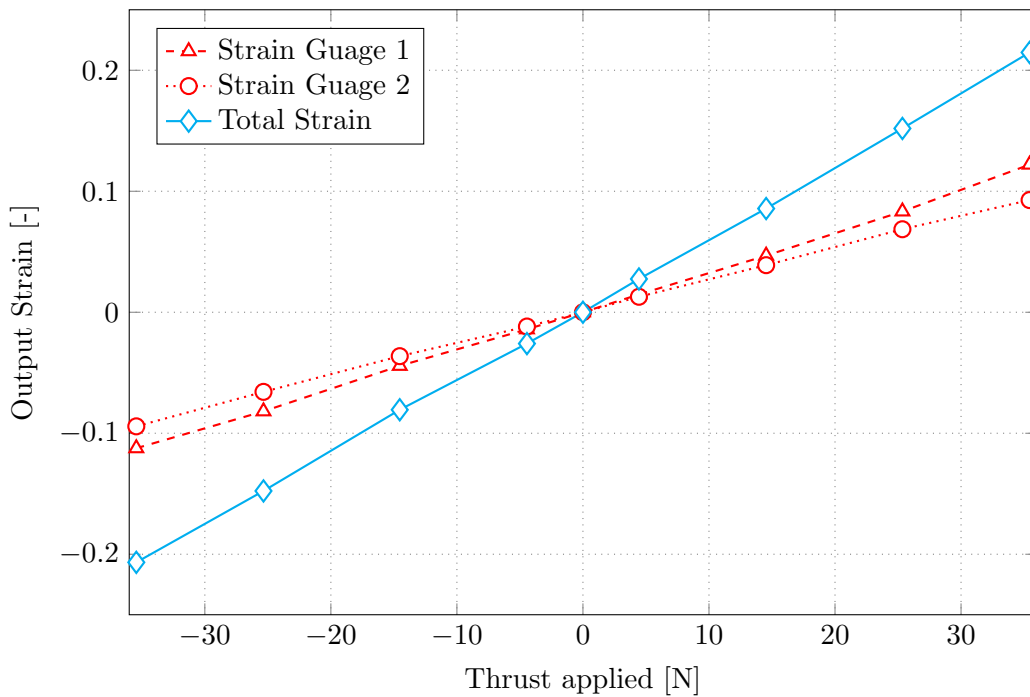
Figure 4.4: The measured strain results from the system loaded with pre-determined axial load for thrust calibration of the test model

to measure the angle. The initial pitch calibration of the blades was done using a bubble level instrument *(see figure 4.5a)*. Later it was discovered that this had a much higher error margin

around ±0.5° which was also confirmed by the re-calibration of the blades using a digital level box *(error margin ±0.1°)* as seen in figure 4.5b. This, however, presented an opportunity to analyze the effects of pitch on the blade performance, which are discussed in section 8.2.

(a) Bubble level being used with the 3D mould   **(b)** Digital level box being used with the 3D mould

Figure 4.5: How the pitch of the blades was calibrated

4.4 Flaps positioning and placement

For the load experiments, three different chord-wise locations were selected, as discussed in section 6.1. These locations were:

   i. 75% *chord*
  ii. 85% *chord*
 iii. 95% *chord*

To be able to install, remove and move the flaps quickly during the measurements, the locations were marked on the blade with a pencil, which stayed on during the whole experiment. Identification of the correct location also posed a challenge, which was addressed by printing actual scale cross-sections onto papers with the chord-wise locations marked (see figure 4.6). The paper was cut to remove the airfoil cross-section from the middle and then these papers were placed at the right r/R location on the blade to mark the chord-wise locations. The flaps spanned from 0.31 r/R to 0.46 r/R. The locations were marked with pencil lines as the flaps had to be moved between measurements. These lines can be clearly observed on the blade in figure 4.7.

It is also important to mention that based on the location of the flaps on the model, $\approx 0.31\ r/R$ to 0.46 r/R, the definition of "root" flap might seem incorrect as the root region is defined as

0 r/R to 0.33 r/R of the blade. However, as explained previously in section 3.3, the blade model was a shortened version of an actual LM388 blade where only the $0 - 0.618\ r/R$ of the actual blade was used *(including the hub the this value is $0 - 0.63\ r/R$)*. The region designated for the flaps on the model corresponds to 0.136 r/R to 0.24 r/R on the actual blade and is therefore well within the root region.

As mentioned in section 3.4, the flaps were cut into 40 mm sections to compensate for the curvature of the blade. This length, however, turned-out not to be small enough especially for the metallic flaps, due to their rigidity, and there was a little gap at the end between the blade and the base of the flap (shown in figure 4.8). Moreover, the top of the flap, especially flap ∠, had a misalignment at the top due to its height and the curvature of the blade, which is highlighted in figure 4.8. Regular tape was applied at the back to close these gaps as these gaps could have otherwise acted as serrated flaps (see section 2.1.3).
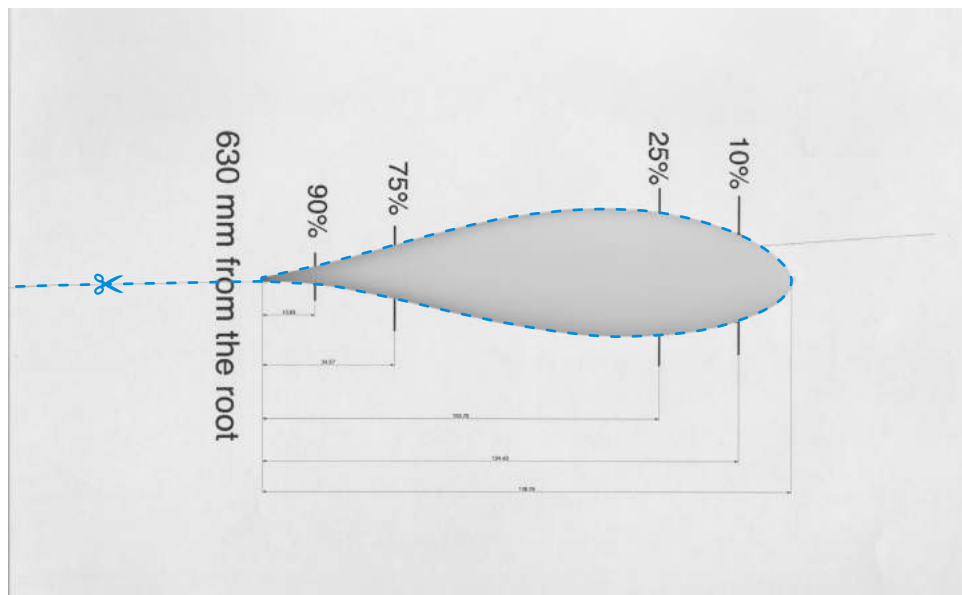
Figure 4.6: A4 paper with cut-out used for marking the positions of the flaps on the blade. This cut out is for $r/R = 0.38$ and is missing the $85\%\ chord$ location. The blue overlaid lines show where the paper was cut to be used.

4.5 Zigzag tape positioning and placement

Like mentioned previously in section 3.5, the zigzag tapes were used to counter some of the effects of flow separation due to the lower Reynolds number. For the placement of zigzag tapes a similar approach was used as for the positioning of the flaps, i.e. using paper cut-outs of the airfoil.

In the beginning, only the root section *(from the hub to 0.3 r/R)* of the blade was equipped with the zigzag tape as it was initially assumed that this would be enough. However, further analysis showed the necessity to trip the flow on the complete span of the blade. Due to differences in the shape of the root section and the rest of the blade, different dimensions of zigzag tapes were used for the root and the rest of the blade. The detailed dimensions of these tapes can been seen in *figure 3.8*. The thicker 11mm tape was used from the hub to 0.3 r/R and placed at 45°

Figure 4.7: The three different flap locations marked with pencil on the blade
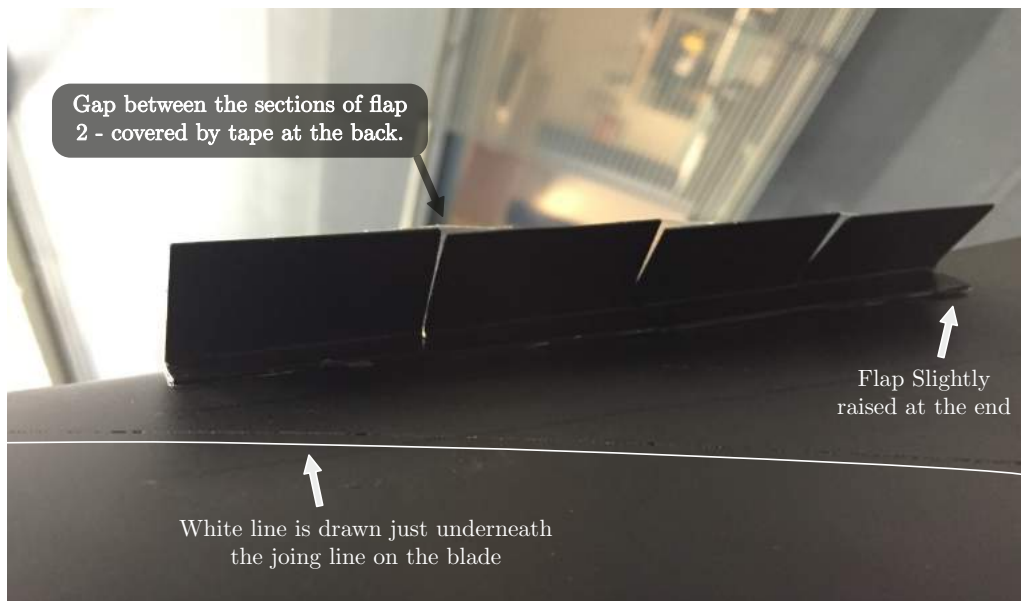
Figure 4.8: A close-up view of flap 2 ∠ positioned on 95% chord.

measured from the leading edge on both sides, as illustrated in figure 4.10, while the thinner tape ran along from 0.27 r/R to the tip and was laid at 10% *chord*.

4.6 Painting of the blade/zigzag tape

During the PIV data accusation process, it was observed that there was a lot of light being reflected from the zigzag tape. In order to fix this issue - black spray paint was applied to the zigzag tape on the blade. This spray *(see figure 4.11)* was not matte as had been assumed and
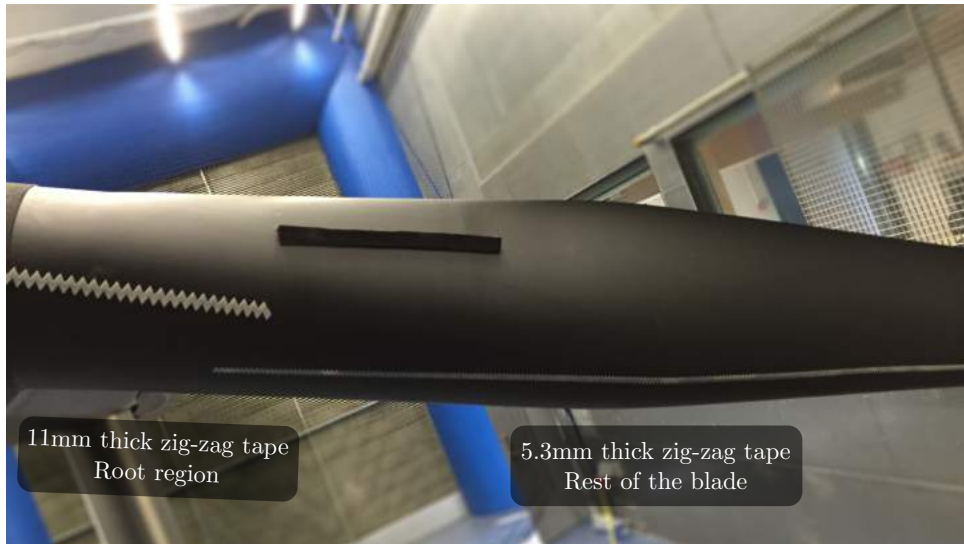
Figure 4.9: The position and the layout of the zigzag tape on the blade

therefore, did not improve the reflection rather might have even slightly made it worse. This will be discussed in section 9.4.
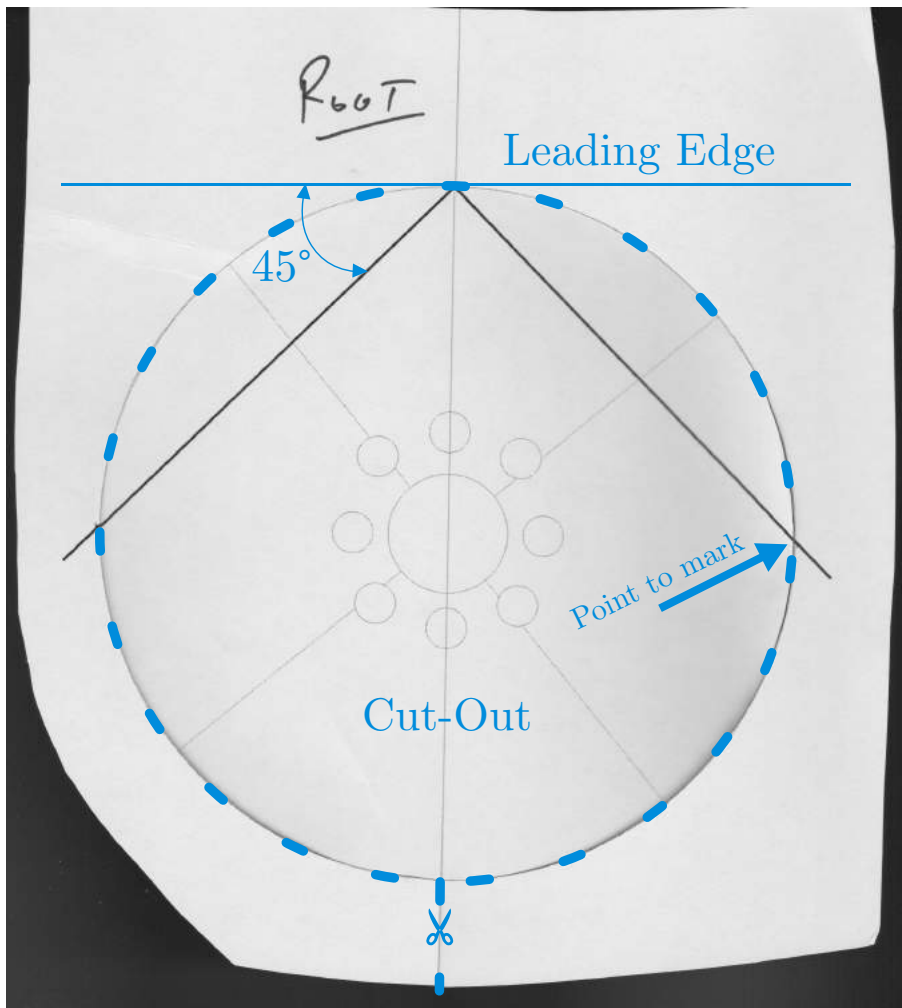
Figure 4.10: Paper cut-out to mark the position on the blade for the zigzag tape. The blue overlaid elements are to illustrate the details and the way it was used.

Figure 4.11: The black spray paint that was used in an attempt to reduce the reflection

Chapter 5

PIV set-up
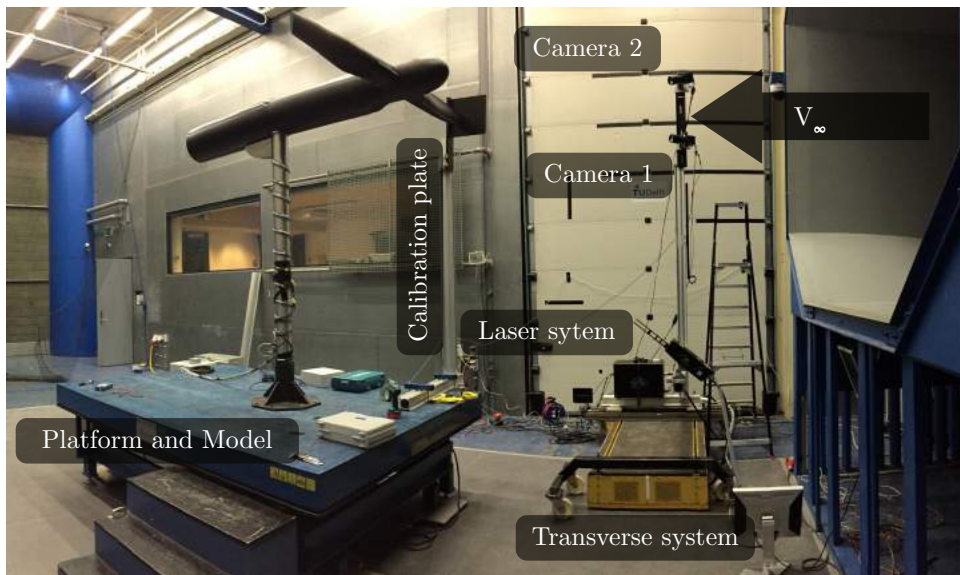
Figure 5.1: A panoramic view of the stereoscopic PIV set-up inside the OJF

Table 5.1: Stereoscopic PIV experimental conditions

Turbine geometry		Operating conditions	
Rotor radius	1.01 m	Flow Velocity	8 m/s
Hub radius	0.107 m	Angular velocity	$36.76 \mathrm{rad\,s}^{-1}$
Number of blades	2	Yaw angle	0°
Blade maximum chord	0.1684 m	Tip Speed Ratio	4.63
Blade Pitch	0°	Atmosphere pressure	1007.86 hPa

Table 5.2: Sterosopic PIV illumination and seeding characteristics

Illumination		Seeding	
Laser type	Double-pulsed Nd:YAG	Fluid Composition	Diethylene glycol & water
Energy per pulse	200 mJ	Fog generator	SAFEX
Sheet thinkness	3 mm	Particle diameter	1 µm *(median)*

5.1 Cameras and their layout

For the stereoscopic PIV analysis two cameras were used for the data acquisition. Both cameras were LaVision's Imager Pro LX (16 megapixel resolution) fitted with Nikon AF Nikkor 180 mm 1:2.8 D lenses. One of the cameras was aligned almost parallel to the blades (i.e. resting or going through the horizontal position.), which can be seen in figure 5.2a. This was done to have only one oblique angle between the object and the image plane and also as a redundancy to fall back to planar PIV in case of any issues with the quality of the stereoscopic PIV results. The second camera was mounted above this plane and "looked-down" at the blade cross-sections, as shown by figure 5.2b. Camera 2 was also equipped with a Scheimpflug to rotate the plane of focus in order to increase the region that is in focus. The Scheimpflug condition was discussed in brief detail in section 2.5.2.
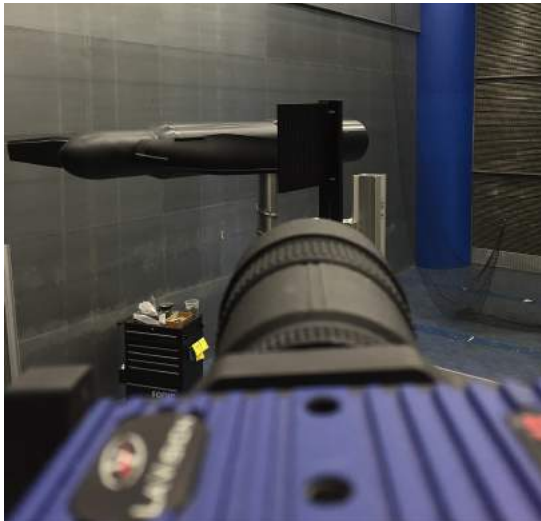
(a) View from camera 1	(b) View from camera 2

Figure 5.2: View of the model and the calibration plate from the cameras

5.2 Laser & optics

The illumination for the PIV was provided by Quantel Laser's EverGreen $(70 - 200 \text{mJ} @ 532 \text{nm})$ Double-pulse Nd:YAG[1] systems. The laser sheet of 3mm was achieved by using three different lenses in a row. The lenses used can be seen in figure 5.3.

---

[1]Neodymium-doped yttrium aluminum garnet; $Nd : Y_3Al_5O_{12}$
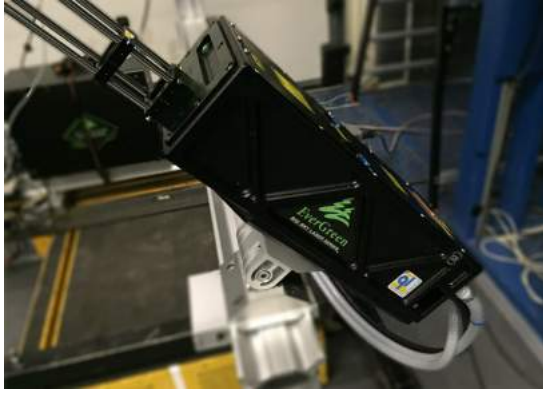
(a) Laser system that provided the light source

(b) Optics used to achieve the laser sheet.

Figure 5.3: Light source and the the optics that were used for the experiment.

5.3 Seeding Particles and seeder

The flow was seeded with smoke particles using a SAFEX® Twin Fog generator. The machine used diethylene glycol and water solution to generate particles of $\sim$ 1µm. The smoke/fog generating machine was placed in the empty space behind the radiator where the flow exited the test section. This way the smoke can get evenly mixed in the flow, which is extremely important for good PIV data. The fog machine was manually operated with a remote that was accessible in the wind tunnel control room. This, however, meant that the fog/smoke consistency was not always constant in the tunnel. Based on the quality of the data being captured more fog/smoke was generated and added to the flow as required.

5.4 Transverse system

The transverse system used during the PIV experiment can be seen in figure 5.1. The electro-mechanical platform is designed to move a metallic base and anything mounted on it along a straight line. A structure consisting of aluminum profiles was built upon this movable base and the laser system and the camera were directly mounted on this frame. The traversing system was operated from a computer in the control room and would move the distance specified in the control software. The frame also ensured that the cameras and the laser system remained static with respect to each other for data acquisition at different positions. Another great advantage was that the wind tunnel did not need to be stopped to move the cameras to the new location and experiments could be carried out uninterrupted

In order to gather data at positions $r/R < 0.37$, the camera set-up was (partially) in the airflow of the wind tunnel nozzle.

5.5 PIV Data acquisition

The PIV data acquisition consisted of the images that were taken by the two cameras that were mounted on the traversing system at different radial positions. The capturing of the images was phase-locked with the rotation speed of the rotor to capture images at each consecutive

rotation. The r/R locations and sequence of this data acquisition are shown in table 6.3. At each location a pair of 100 images were made. The images were saved using LaVision DaVis software on a server computer that was connected to the camera systems. The resolution of the captured images from both cameras was 4872 x 3248 pixels.

Chapter 6

Test cases

6.1 Load cases

The original plan consisted of eleven load cases, with mainly three types of flaps placed at three different locations and of course the no flap cases with and without tripping-wire. However, due to the wrong initial pitch determination some of the tests needed to be redone and in the process generated additional load cases. The details of all the load cases can be seen in table 6.1. The dashed-line in the table indicates the point at which the pitch was corrected as explained in section 4.3. The result of these cases are discussed in chapter 8. Additionally, the initial semi-tripping *(zigzag tape from hub to 0.3 r/R)* and finally the complete blade also generated additional load cases. The details of the zigzag taps used can be found in section 3.5, while their positioning and placement are explained in section 4.5. The second and the third columns in table 6.1 indicate the status of zigzag tape for each case.

The positions of flaps are described in section 4.4, while their types and dimensions are elaborated in section 3.4. It may be evident from table 6.1, that the load case of 85%c for flap △ is missing. This load case was skipped due to time limitations and this choice will be reasoned in section 8.3.

6.2 PIV configurations

Based on the results from the load measurements as discussed in chapter 8, flap △ at 95%c was selected for the PIV analysis. Multiple r/R locations were selected along the blade for data acquisition, which are listed in tables 6.2 and 6.3. Table 6.2 gives a general overview of the positions for the clean/no flap and flap configurations, while table 6.3 details the sequence in which the actual experiment was carried out and further parameters that were measured during the experiment. As can be seen from table 6.2 the main focus of the experiment was on the flapped blade since most measurements were reserved for this configuration. Furthermore, it was assumed that the region *(far)*-outside flap location would behave similarly to the flapped configuration. Therefore, only a few locations within the *region intended for flap* were selected in addition to a few locations just outside this region to compare the two configurations. The

Table 6.1: Load cases and their specifications

#	Root trip	Span trip	Spoiler	Chord-wise pos. [%]	Pitch [deg]
1					0.45 ± 0.05
2	✓				0.45 ± 0.05
3	✓		1	75	0.45 ± 0.05
4	✓		1	85	0.45 ± 0.05
5	✓		1	95	0.45 ± 0.05
6	✓		2	75	0.45 ± 0.05
7	✓		2	85	0.05 ± 0.05
8	✓		2	95	0.05 ± 0.05
9	✓		2	75	0.05 ± 0.05
10	✓				0.05 ± 0.05
11	✓	✓			0.05 ± 0.05
12	✓	✓	1	75	0.05 ± 0.05
13	✓	✓	1	85	0.05 ± 0.05
14	✓	✓	1	95	0.05 ± 0.05
15	✓	✓	2	75	0.05 ± 0.05
16	✓	✓	2	85	0.05 ± 0.05
17	✓	✓	2	95	0.05 ± 0.05
18	✓	✓	3	75	0.05 ± 0.05
19	✓	✓	3	95	0.05 ± 0.05

highlighted measurements in the tables fall in the region intended for flap, i.e. $0.31\ r/R$ to $0.46\ r/R$ and $0.57\ r/R$ is the maximum chord location.

The sequential and more detailed PIV configurations are given in table 6.3.

Table 6.2: PIV data acquisition locations r/R,
the region intended for flap is highlighted

Clean Configuration	Flap Configuration
	0.9
	0.8
	0.7
0.57	0.57
0.48	0.48
0.46	0.46
0.42	0.42
	0.38
	0.36
0.34	0.34
	0.33
	0.31
0.3	0.3
0.26	0.26
	0.22
0.17	0.17

Table 6.3: PIV data acquisition sequence and details,
the region intended for flap is highlighted

#	Flap	Painted	r/R	V	P	T	ρ
-	-	-	-	[m/s]	[hPa]	[C^o]	[kg/m^3]
1	✓		0.9	7.95	1007.26	20	1.197
2	✓		0.8	7.95	1007.28	20	1.197
3	✓		0.7	7.94	1007.24	20	1.197
4	✓		0.57	7.94	1007.2	20	1.197
5	✓		0.48	7.93	1007.12	19.9	1.19
6	✓		0.46	7.92	1007.1	19.9	1.197
7	✓		0.42	7.93	1007.2	19.9	1.197
8	✓		0.38	7.93	1007.35	19.9	1.198
9	✓		0.34	7.93	1007.48	19.9	1.198
10	✓		0.26	7.92	1007.49	19.9	1.198
11	✓		0.22	7.94	1007.9	19.7	1.199
12	✓		0.17	8.03	1007.88	19.9	1.198
13	✓	✓	0.26	8.03	1007.87	19.9	1.198
14	✓	✓	0.30	8.03	1007.97	20.2	1.197
15	✓	✓	0.31	8.03	1007.96	20.2	1.197
16	✓	✓	0.33	8.02	1008.24	19.4	1.200
17	✓	✓	0.36	8.02	1008.27	19.9	1.198
18		✓	0.57	8	1008.38	19	1.203
19		✓	0.48	8.01	1008.44	20	1.198
20		✓	0.46	8.02	1008.42	20.2	1.198
21		✓	0.42	8.02	1008.43	20.3	1.197
22		✓	0.34	8.03	1008.43	20.4	1.197
23		✓	0.30	8.02	1008.51	20.5	1.197
24		✓	0.26	8.02	1008.55	20.6	1.196
25		✓	0.17	8.02	1008.56	20.6	1.196

Chapter 7

PIV data processing

The data obtained from PIV was processed using LaVision Davis 8.4.0 software. A screen-shot of the processing window can be seen in figure A.1.

7.1   Image restoration and image enhancement

As mentioned earlier, PIV analyses depend on the light reflected from smoke particles in the air, which is captured as images during the data acquisition process. The light, however, gets reflected not only from the smoke particles but also any other reflective surface in its path. Moreover, not all areas of the images are equally exposed. The images obtained, therefore, are not optimal and in order to get good results, these images needed to be optimized. This process consist of image restoration and image enhancement, where restoration removes/minimizes the undesired artifacts from the images while enhancement amplifies the useful aspect of the images [40].

These filters even out the overly bright areas and increase the contrast to make the particles 'pop out' and increase the quality of the results. Three filters were used to fine-tune the images for the PIV analysis. namely:

   i. Subtract time filter
  ii. Subtract sliding minimum
 iii. Intensity normalization filter

Subtract time-filter   The concept of the subtract minimum filter is illustrated in figure 7.1 which also details the parameters that were selected. The subtract minimum filter is a non-linear filter and eliminates the background noise by subtracting the minimum intensity from the images. The result of using this filter are given in figure 7.5, where figure 7.5a shows the original image and figure 7.5b the processed image after the application of this filter. It is clearly evident that the reflection has been significantly reduced. This filter used all images and can therefore be equated to removing background noise/distortions.
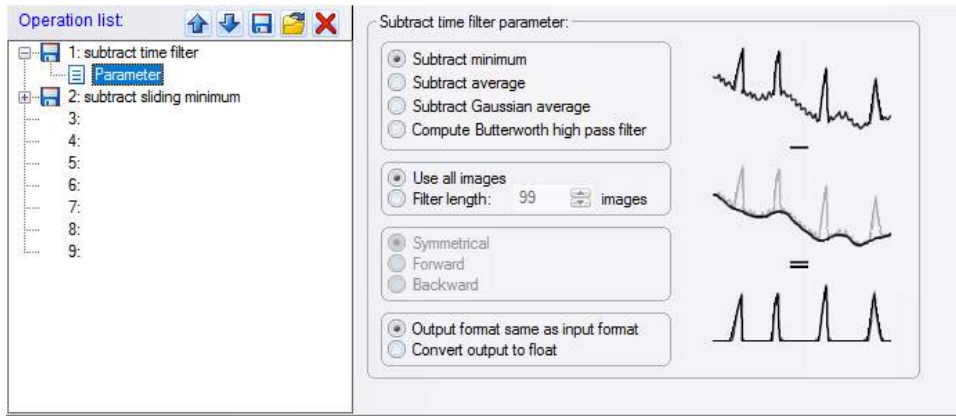
Figure 7.1: The details of the Subtract minimum filter and the parameters that were used and applied to all images.

Subtract sliding minimum filter   After the subtraction of the minimum filter, the sliding minimum filter was used to further improve the contrast and get rid of the reflections. The effects of the application of this filter can be seen in figure 7.5, going from sub-figure 7.5b to 7.5c. This filter is also non-linear but applied more locally, i.e. to smaller regions of the images. A scale length of 7 pixels was chosen after trial and error.
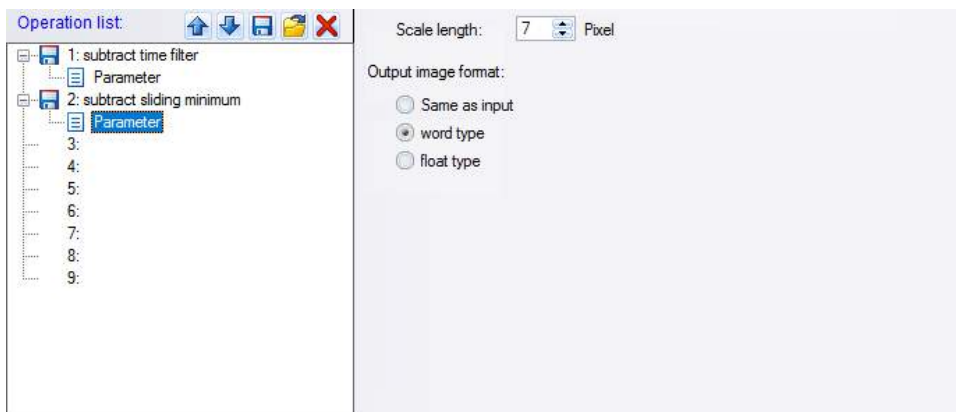
Figure 7.2: The details of the Subtract sliding filter and the parameters that were used and applied to all images.

Intensity normalization filter   Not all areas of captured images are equally illuminated, i.e. some parts have more reflected light or are overexposed even after subtracting time-filter and sliding minimum while other regions are underexposed. To compensate for these extremes, the images are 'normalized' to adjust the range to a more realistic or normal limits. This concept is visualized and elaborated by an example in figure A.6. A scale of 4 pixels was used for this normalization as shown in figure 7.3.
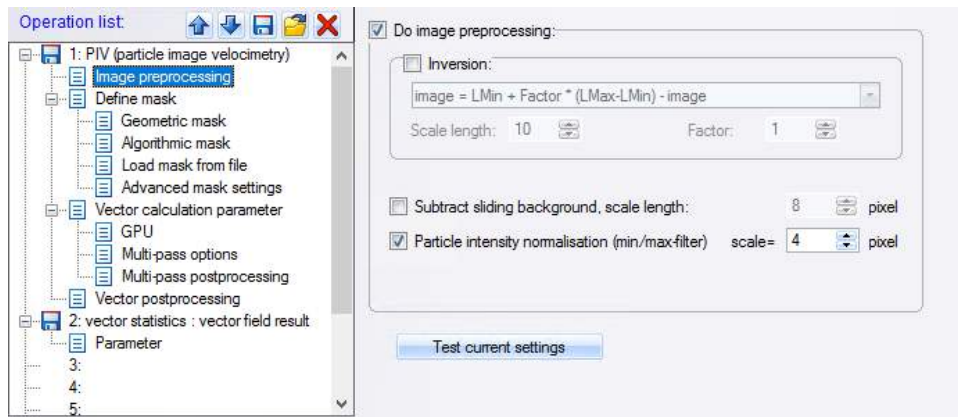
Figure 7.3: The details of the Intensity normalization filter and the parameters that were used and applied to all images.
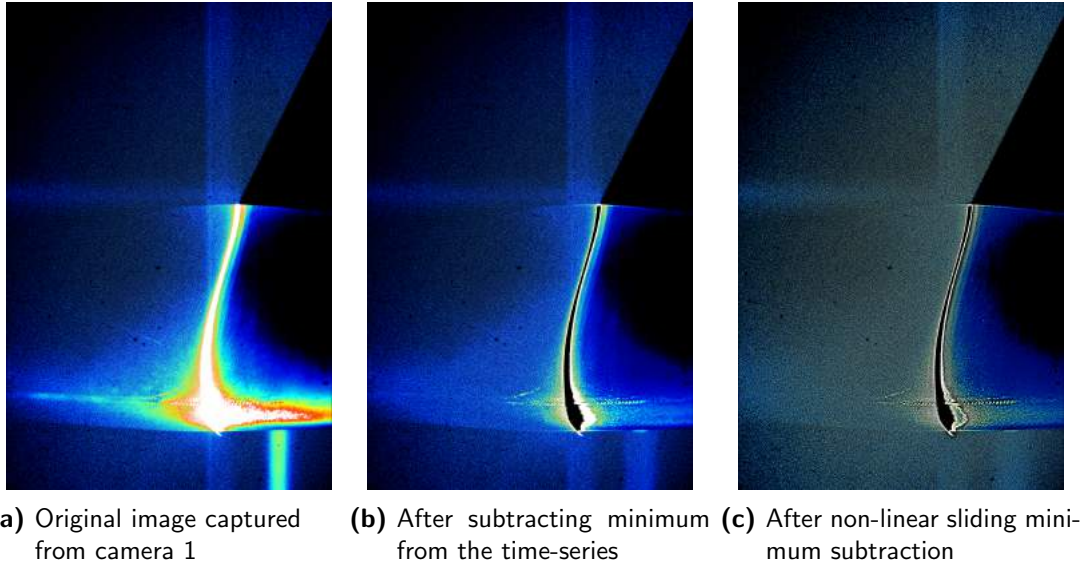

Figure 7.4: This picture clearly shows the extent of light being reflected from the wind turbine model blade. The reflected region is not usable for the analysis.

7.2 Calibration

An important step in the data processing involves the calibration of the data. This is done to correct the perceptive and the scale of the images. This is achieved by using a reference object; a calibration plate. For this case, a Type 30 calibration plate from LaVision was used. This plate has a dimension of $300 \times 300 \times 12$mm, is black and covered with 144 white dots of 2mm diameter ($12x \times 12y$).

This plate was erected parallel to the tip of the blade as shown in figure 5.1. An A4 paper with some text (12pt) on it was also taped on the calibration plate and used to focus the cameras for clarity. After this, a set of images were captured from both cameras 1 and 2. These were then

(a) Original image captured from camera 1   **(b)** After subtracting minimum from the time-series   **(c)** After non-linear sliding minimum subtraction

Figure 7.5: Image restoration and enhancement process steps of images captured at $0.57\ r/R$

processed in LaVision DaVis software. The images of the calibration plate from both camera 1 and 2 can be seen in figures 7.6a and 7.6b respectively. The resulting corrected image from the stereoscopic calibration is presented in figure 7.6d.
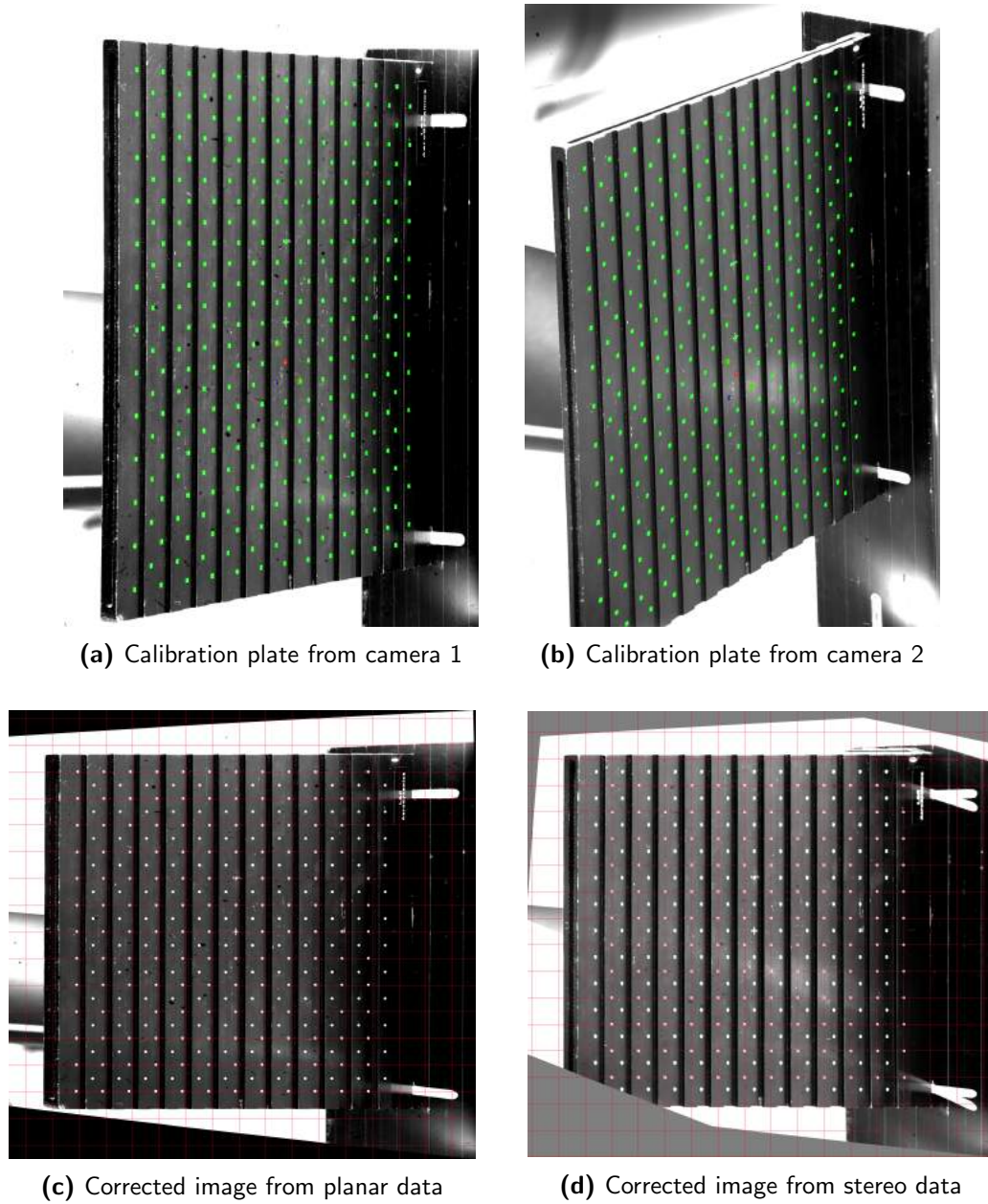
As mentioned earlier, a stereoscopic PIV was carried out. The results from the data processing were not completely satisfactory and therefore it was decided it also carry out analysis from the data from one camera that was aligned almost perpendicular to the plane of the blade. The software DaVis applies calibration automatically to the processing of stereoscopic analysis and therefore, it was assumed that this would also be the case for general PIV analysis. Later on it was realized that this was that this was not the case and the calibration for one camera case was not applied correctly to the process data. Figure A.1 shows the option that needed to be selected for calibration of a single camera set-up to be applied for the processing.

Initially, to avoid redoing all analyses again in LaVision DaVis (due to time constraints) the choice was made to come up with an alternative solution. This solution consisted of first using Adobe Photoshop CC's '*Perspective Wrap*' feature to scale the plate to its square dimension and then measure the scaled image and the original image to calculate the scaling matrices that would then be multiplied with the results to get the correctly calibrated results. The image manual scaling using the '*Perspective Wrap*' feature is shown in figure 7.6a.

It was assumed that the x-axis scaled linearly from left to right and for the y-axis the distance from the center to edges was measured for the calculation as depicted in figure 7.6a. The scale factors in both the x and y directions were calculated as given by equations 7.2, 7.2 and 7.3. For the y axis, two factors were required due to the different scaling of the top and bottom parts.

$$x_{scale} = \frac{x_{final}}{x_{initial}} \tag{7.1}$$

$$y_{scale,top} = \frac{y_{top}}{y_{initial}/2} - 1 \tag{7.2}$$

(a) Calibration plate from camera 1

(b) Calibration plate from camera 2

(c) Corrected image from planar data

(d) Corrected image from stereo data

Figure 7.6: Difference in planar and stereo calibration

$$y_{scale,bottom} = \frac{y_{bottom}}{y_{initial}/2} - 1 \tag{7.3}$$

All matrices had the same m x n dimensions as the original x and y matrices from the PIV data. In the x-direction the scaling factor x_{scale} was applied incrementally from the left side of the image to the right edge. This is evident from the matrix that goes from $0 \cdots m$ in equation 7.4.
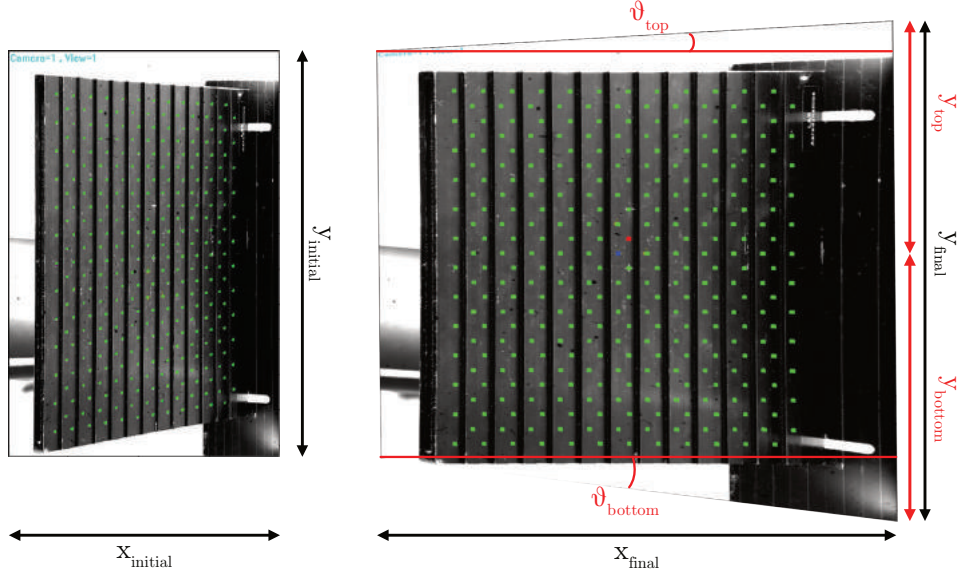
Figure 7.7: The scaled and unscaled/original images side by side with some of the dimensions labeled that are used to calculate the scaling/calibration.

$$x_{new} = \frac{x_{scale}}{m} \begin{bmatrix} 0 & \dots & 0 & \dots & 0 \\ \vdots & \ddots & \vdots & \ddots & \vdots \\ m/2 & \dots & m/2 & \dots & m/2 \\ \vdots & \ddots & \vdots & \ddots & \vdots \\ m & \dots & m & \dots & m \end{bmatrix} \cdot x \tag{7.4}$$

As the top and lower part does not scale equally in both directions, the top and the bottom part were scaled separately and these factors were also applied to the relevant y values using the y_{scale} matrix as given by equation 7.6. The scaling in the y direction was also dependent on the x scaling.

$$y_{new} = \begin{bmatrix} 0 & \dots & 0 & \dots & 0 \\ \vdots & \ddots & \vdots & \ddots & \vdots \\ m/2 & \dots & m/2 & \dots & m/2 \\ \vdots & \ddots & \vdots & \ddots & \vdots \\ m & \dots & m & \dots & m \end{bmatrix} \cdot y_{scale} \cdot y \tag{7.5}$$

$$y_{scale} = \begin{bmatrix} \frac{y_{top}}{n_{top}} \begin{bmatrix} n_{top} & \dots & n_{top}/2 & \dots & 0 \\ \vdots & \ddots & \vdots & \ddots & \vdots \\ n_{top} & \dots & n_{top}/2 & \dots & 0 \\ \vdots & \ddots & \vdots & \ddots & \vdots \\ n_{top} & \dots & n_{top}/2 & \dots & 0 \end{bmatrix} & \frac{y_{bot}}{n_{bot}} \begin{bmatrix} 0 & \dots & n_{bot}/2 & \dots & n_{bot} \\ \vdots & \ddots & \vdots & \ddots & \vdots \\ 0 & \dots & n_{bot}/2 & \dots & n_{bot} \\ \vdots & \ddots & \vdots & \ddots & \vdots \\ 0 & \dots & n_{bot}/2 & \dots & n_{bot} \end{bmatrix} \end{bmatrix} \tag{7.6}$$

where $n_{top} + n_{bot} = n$ and the matrix y_{scale} have the same $m \times n$ dimensions

Alternatively,

$$
y_{new} = x_{new} \left[\frac{\tan \vartheta_{top}}{n_{top}} \begin{bmatrix} n_{top} & \cdots & n_{top}/2 & \cdots & 0 \\ \vdots & \ddots & \vdots & \ddots & \vdots \\ n_{top} & \cdots & n_{top}/2 & \cdots & 0 \\ \vdots & \ddots & \vdots & \ddots & \vdots \\ n_{top} & \cdots & n_{top}/2 & \cdots & 0 \end{bmatrix} \frac{\tan \vartheta_{bot}}{n_{bot}} \begin{bmatrix} 0 & \cdots & n_{bot}/2 & \cdots & n_{bot} \\ \vdots & \ddots & \vdots & \ddots & \vdots \\ 0 & \cdots & n_{bot}/2 & \cdots & n_{bot} \\ \vdots & \ddots & \vdots & \ddots & \vdots \\ 0 & \cdots & n_{bot}/2 & \cdots & n_{bot} \end{bmatrix} \right]
$$

(7.7)

The scaling matrix of this method also follows the same pattern from the previous method, having the same $m \times n$ dimensions and $n_{top} + n_{bot} = n$. Both methods yielded similar results, however, this approach was chosen as it required less steps. The calibrated result from this method is shown in figure 7.8a.
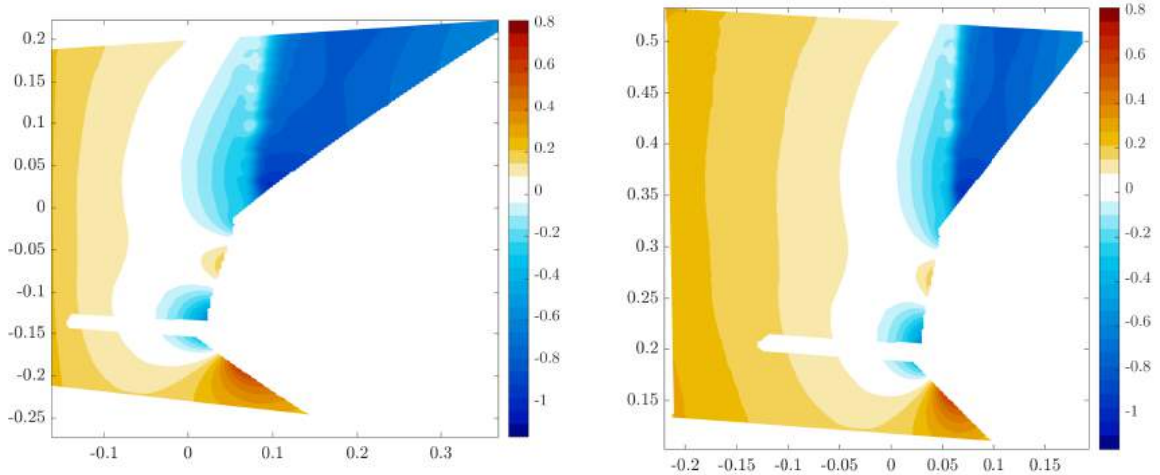
(a) Calibrated using manual image manipulation

(b) Calibrated using polynomial eq. from DaVis

Figure 7.8: Manually calibrated Velocity fields V_x as a function of V_D pressure side at $r/R = 0.9$

Another method that was used consisted of getting the 3rd order polynomial equation found in the "*Camera Calibration Information*" from LaVision DaVis (see figure A.2). However, this equation consisted some error and multiple attempts were made to change the signs of various variables in different combinations to no avail. The result from this method is given in figure 7.8b. The result from this were expected to match the shape given in figure 9.25c, 9.24d, 9.24e and 9.24f.

Before applying the calibration to all results, it was first compared to one result re-calculated with the corrected calibration in DaVis given in figure 9.2a. The shape of image-manipulation calibration has a some-what similar shape, however, the velocity field seems to be stretched towards the right-side which might be due to the assumption that the image expands from left to right. This also results in the different contours of the velocity field. Based on the discrepancies from both methods, the new corrected planar calibration was used to recalculate all results which are presented in chapter 9.

7.3 PIV data processing

Multi-grid interrogation   Multi-grid interrogation was selected for both the planar and stereoscopic, cross correlation analyses as this method uses a larger interrogation domain for each previous "pass" and thus assuring that the in-plane loss of the correlation remain small [40]. A window size of 128×128 was selected with a 75% overlap which converges to the desired window size of 32×32 with a 50% overlap. As the images were captured in portrait aspect-ration a somewhat similar weight was selected for the windows. The details for the planar case and the stereoscopic cases can be seen in figure A.1 and 7.9 respectively.
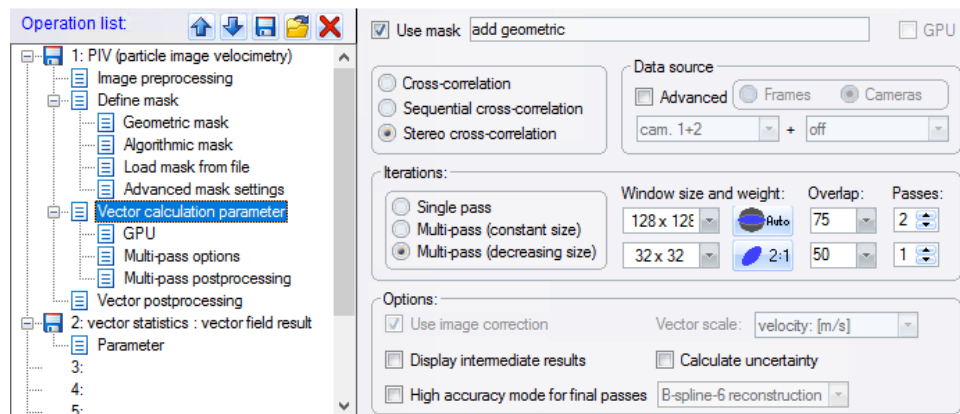
Figure 7.9: The parameters that were selected for the cross-correlation

Averaging   The cross-correlation analyses were done for the sets of 100 images and the final step, therefore, was to average all these 100 results into one. The averages of the different velocity components and their standard deviations were calculated in this final step.

Part III

Results and discussion

Analysis of the Experimental Data

This chapter will discuss the results that were obtained from the load measurements from the first part of this experiment. Details on the test case can be found in section 6.1.

The initial calculation of the ω and λ were mistakenly done for the complete blade, i.e. the uncut blade as explained in the section 3.3. The wrong value $R = 1.4167$ m was used. Only after the experiments this discrepancy was discovered. The rpm values that were used during the experiments were manually fed into the software to drive the turbine at the desired rpm as shown in figure A.3. Therefore, these fixed values were used to recalculate the correct λ tip speed ratios as given in table 8.1 and also for the generation of plots discussed in this chapter.

$$\lambda_{tip} = \frac{\Omega R}{V_\infty} \Rightarrow \frac{2\pi f \cdot R}{V_\infty} \tag{8.1}$$

Table 8.1: Tip speed ratios with corresponding rotor speeds and the corrected tip speed ratios

Initial λ_{tip}	Rotor Speed [rpm]	Corrected λ_{tip}
3	162	2.14
4	216	2.85
5	270	3.56
6.5	351	4.63
7	377	4.99
7.5	404	5.35
8	431	5.70
8.5	458	6.06
9	485	6.42
9.5	512	6.77
10	539	7.13

The x-axes of all the plots is occupied by these corrected λ_{tip}, while similar scales of y-axes were used for similar kinds of plots. Plots in figures 8.1, 8.2, 8.3 and 8.4 have combined C_P

C_T plots so their y-axis spans from 0 to 0.95. For all C_P plots namely figures 8.7, 8.11, 8.15, 8.19, 8.23 and 8.27 the y-axes scales from 0 to 0.3 and their corresponding detailed comparative plots 8.8, 8.12, 8.16, 8.20, 8.24 and 8.28 do not have the exact same limits but always the same scale/length of 105% points. This choice was made to prevent the plots from getting small but still keeping the same scale. For the C_T plots in figures 8.9, 8.13, 8.17, 8.21, 8.25 and 8.29 a scale of 0.2 to 0.8 was used for the y-axes while for their corresponding detailed comparative plots 8.10, 8.14, 8.18, 8.22, 8.26 and 8.30 the y-axes ranges from -15% to 40%.

8.1 The effects of tripping

As explained in section 4.5, initially only the section from the hub to $0.3r/R$ was tripped and eventually the rest of the blade. The C_P and C_T measurements were also carried out for the blade without any zigzag tapes. This presented an opportunity to analyze the effects of tripping on power and trust. In order to clearly differentiate the graphs from each other, the following symbols are used for the different tripping configurations;

    i.   No-tripping $\longleftrightarrow$
   ii.   Semi-tripped $\rightsquigarrow$
 iii.   Fully-tripped $\leftrightsquigarrow$

The first analysis consists of the comparison between the blade without any zigzag tape and the root zigzag tape case, given in the table 6.1 as case 1 and case 2, respectively. Both these measurements were carried out before the pitch of the blade was corrected as discussed in section 4.3.

From the graphs in figure 8.1, it can observed that the tripping clearly increased the thrust for all λ_{tip} values, approximately 10%, while the C_P values initially decline for lower λ_{tip} and increase with higher λ_{tip} values. This clearly indicates the positive effect, especially at higher rotational speeds.

Also the shift from semi (root-only) zigzag tape to the full-blade zigzag tape seems to have a positive influence on the C_P values, however, the C_T values display a negative trend with an average drop of 6%. This comparison is graphed in figure 8.2. The increase in the C_P values is more significant in comparison to the clean to semi-tripped case with an increase of around 40% for $3.5 > \lambda_{tip} < 6$.

This trend seems to continue to the flapped configurations. Figures 8.3 and 8.4 show the comparison between the semi-tripped and fully tripped cases for flap 2 $\angle$ at $75\%\,c$ and $95\%\,c$ respectively. The C_P plots of both fully tripped and flapped configurations follow a conventional pattern and have higher values between $3 \gtrsim \lambda_{tip} \lesssim 5.5$ while on the other hand the values of C_P and C_T for the semi-tripped flapped configurations see a sudden increase around the $\lambda_{tip} \approx 6$ mark and decreasing from thereon. A possible explanation for this phenomenon is that the blade experiences dynamic stall for the semi-tripped case.

8.2 The effects of blade pitching

The pitch of the blades was corrected during the load measurements as it was not initially set with a highly accurate measuring instrument, which was elaborated in sections 4.3 and 6.1.
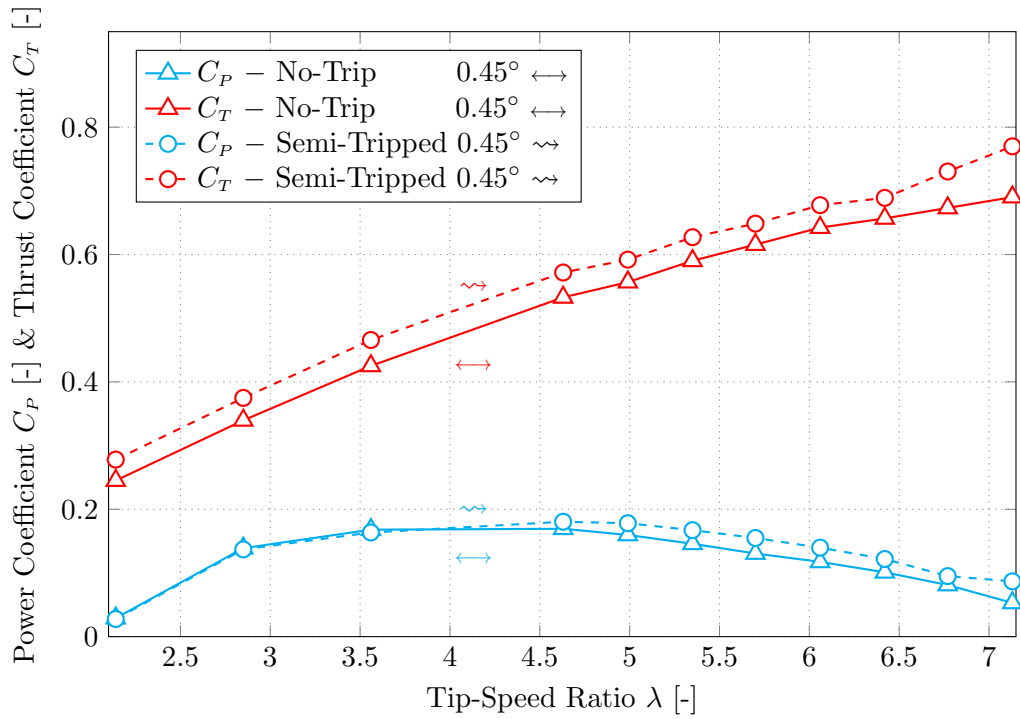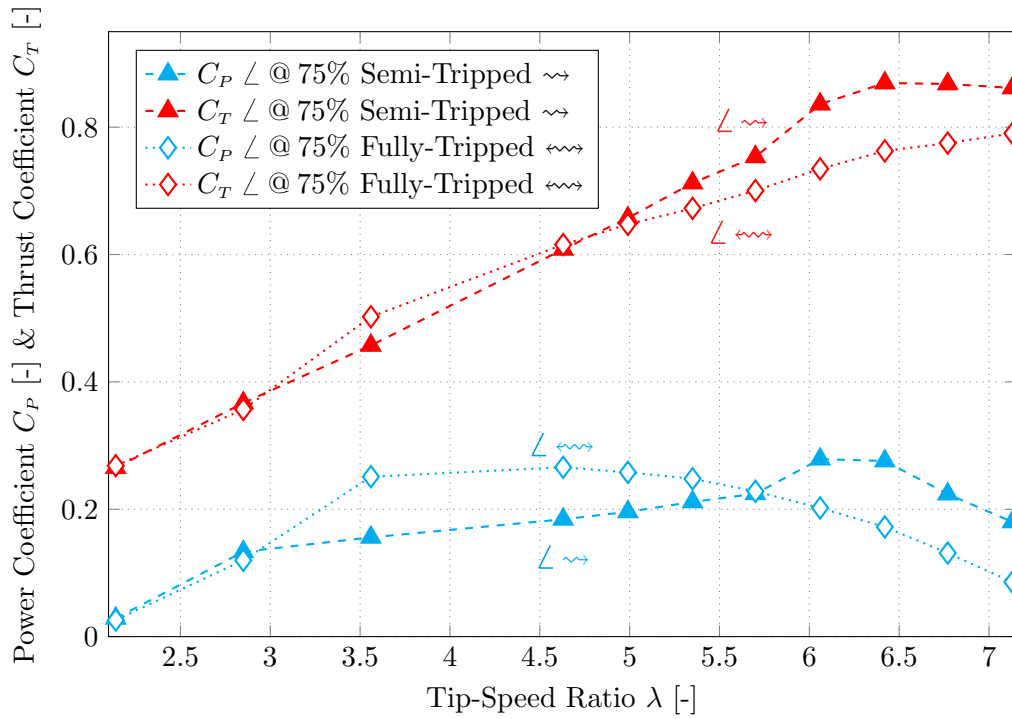
Figure 8.1: Effect of tripping on the C_P & C_T values - No-Trip vs. Semi-Tripped *(root section)* blades $\delta\theta = 0.45$
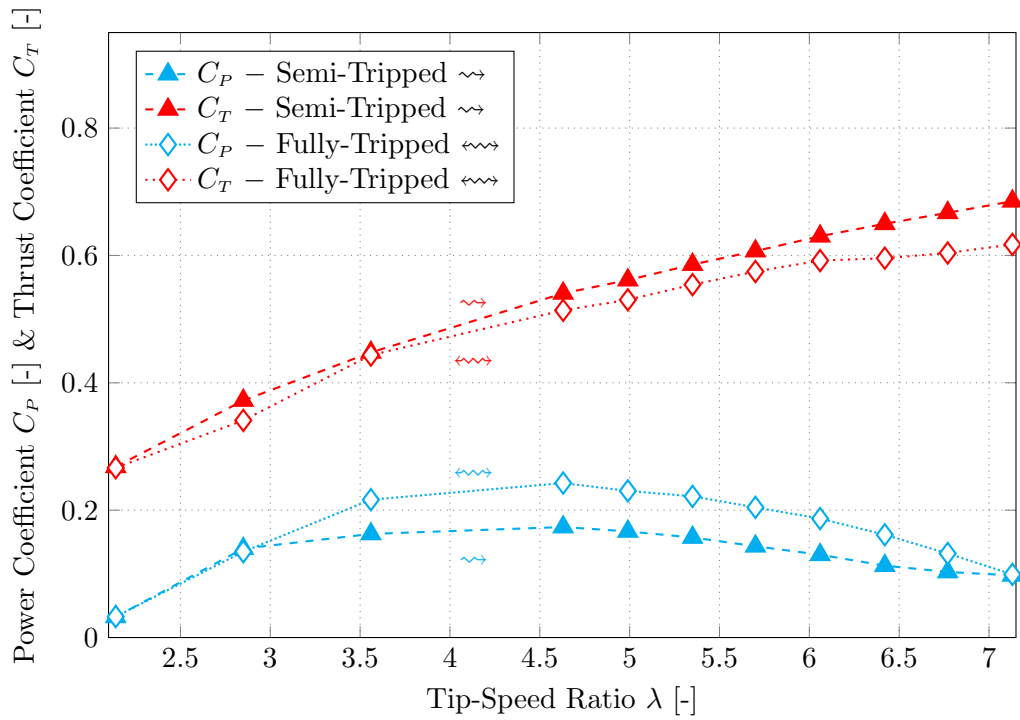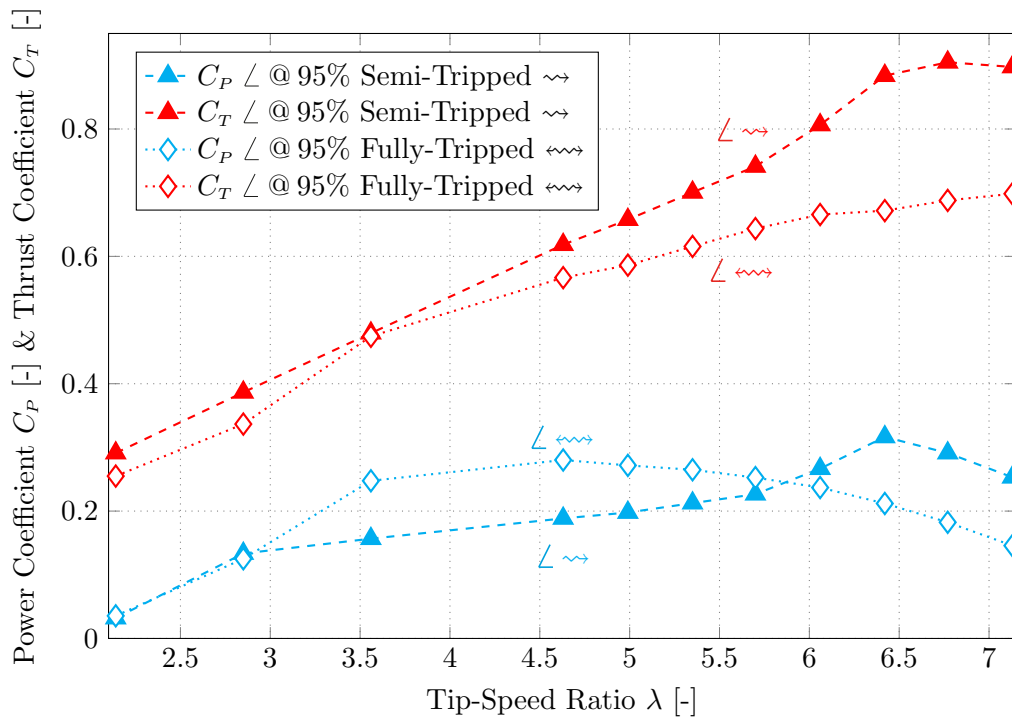

Figure 8.2: Effect of tripping on the C_P & C_T values - Semi-Tripped vs. Fully-Tripped blades

This opportunity was availed to compare and understand the effect of this pitch correction on
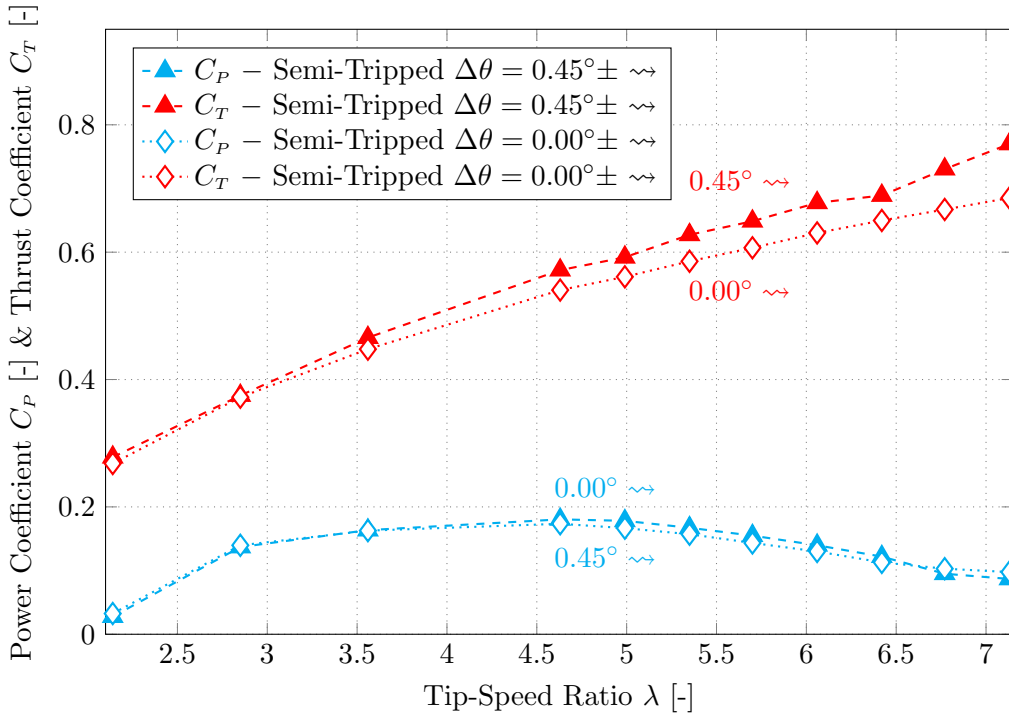
Figure 8.3: Effect of tripping on the C_P & C_T values - Semi-Tripped vs. Fully-Tripped blades with Flap ∠ at 75% chord

Figure 8.4: Effect of tripping on the C_P & C_T values - Semi-Tripped vs. Fully-Tripped blades with Flap ∠ at 95% chord

the thrust and power of the turbine. Only two configurations could be compared; one with Flap 2 $\angle$ @75% chord (case 2 vs. 10) and another without any flap (case 6 vs. 9) as given in table 6.1 and their load cases plotted in figures 8.5 and 8.6. As specified before the correction was only 0.45° and, therefore, not a significant change was expected in the C_P and C_T values. This is also evident from figures 8.5 and 8.6 where only a slight increase in value of C_P can be observed after the correction of the pitch, whereas, the values of C_T decrease somewhat. The changes are more prominent for higher tip speeds which makes sense due to the higher velocity experienced by the blade. The C_T on the other hand gives higher values for both cases.

It should also be noted that both the cases were semi-tripped, i.e. the zigzag tape was only applied to the root section. The similar pattern *(jump around $\lambda_{tip} \simeq 6$)* in the graphs of C_P and C_T for the pitch-corrected flap case is also evident in figure 8.6 as previously discussed in section 8.1 and shown in figures 8.3 and 8.4.

Figure 8.5: Effect of pitching $\Delta\theta = 0.45°$ on the C_P & C_T values - Semi-Tripped vs. Semi-Tripped $\Delta\theta = 0.45°$ blades

8.3 Effect of different flap location

The various flap positions were detailed In section 4.4, namely;

   i. 75% *chord*
  ii. 85% *chord*
 iii. 95% *chord*

In this section, the results for each flap at different locations will be compared to understand the effect of flap location on the C_P and C_T.
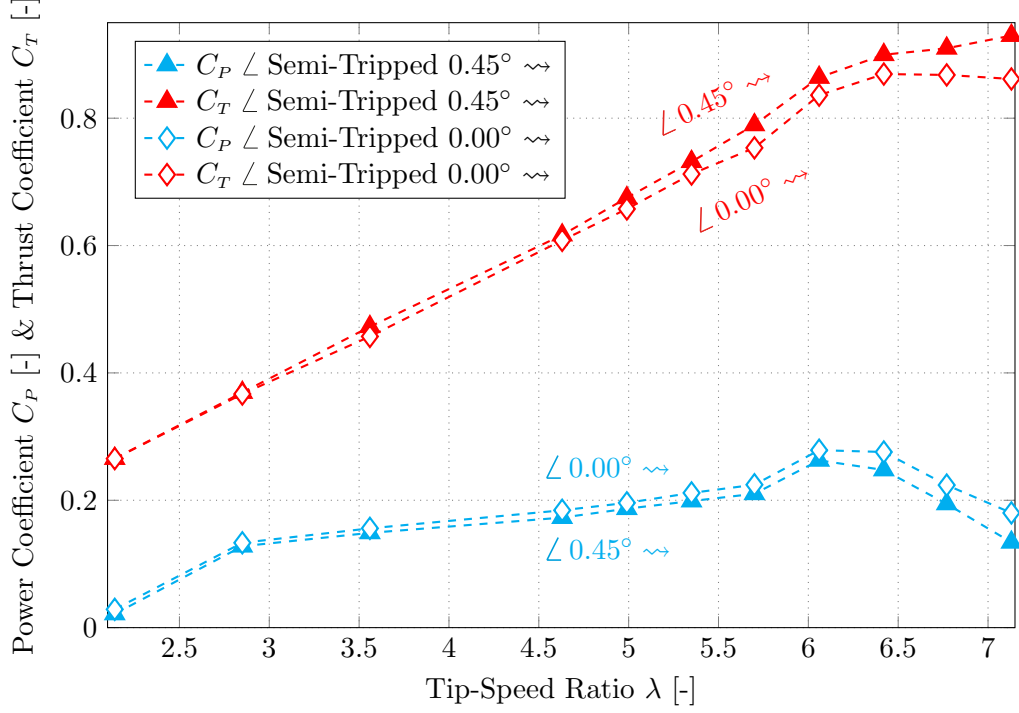
Figure 8.6: Effect of pitching $\Delta\theta = 0.45°$ on the C_P & C_T values - Semi-Tripped vs. Semi-Tripped $\Delta\theta = 0.45°$ blades

From figures 8.7, 8.11 and 8.15 it can clearly be seen that the C_P values in comparison to the no-flap configuration are generally higher, especially for $\lambda_{tip} > 2.85$. For $\lambda_{tip} \gtrsim 3$, the values always stay higher than the no-flap case and only for one case namely, flap 2 $\angle$ at 75% chord and $\lambda_{tip} > 6.77$ do the values of C_P go below the no-flap case as can be seen in figure 8.11. For $\lambda_{tip} \lesssim 3$, the values seem to be slightly lower than the no-flap case and the height of the flaps also seem to play a role and will be discussed in section 8.4.

The values of C_P diverge from each other at higher λ_{tip}. For the 75% and 85% chord locations, the values remain similar and only start diverging beyond $\lambda_{tip} \lessgtr 5.5$ as evident from figures 8.19 and 8.23. This similarity between the two locations in combination with time constraints were the reasons to skip the load case for flap 3 $\triangle$ at 85% chord. The 95% chord location gives the highest peak for all 3 flaps and the peaks always occur at $\lambda_{tip} = 4.63$ (351 rpm), which was also the λ_{tip} for the PIV test cases.

The differences between the various locations is greatest for flap 2 $\angle$ with the C_P for 75% and 85% locations starting below the no-flap configuration and completely converging with the 95% values at $\lambda_{tip} = 3.56$. From there on, the values for 75% and 85% overlap each other till $\lambda_{tip} = 5.35$ and eventually for higher λ_{tip} the values seem to drop a little and for 75% chord location the values end up going below the no-flap configuration. The 95% chord location however shows a constant positive trend as visible in figure 8.12.

The C_T are also mostly higher than the no-flap configuration and only slightly lower for certain load cases but always at low tip speed ratios $\lambda_{tip} < 3$, as observable in figures 8.21, 8.25 and 8.29. The 75% and 85% chord locations also give similar values for C_T. Even for the 95% chord position the differences are much smaller compared to the C_P values, with only flap 2 $\angle$ showing a significant difference at 95% chord as can be seen in figure 8.13, this will be discussed further

in section 8.4. For both flap 1 $\angle$ and flap 2 $\angle$, the lowest values generally occur at 95% chord, while for flap 3 $\triangle$, values for C_T at 95% chord are higher till $\Lambda_{tip} \leq 6$ than at 75% chord and then flip with a sudden jump and become lower as can be observed in figure 8.18.
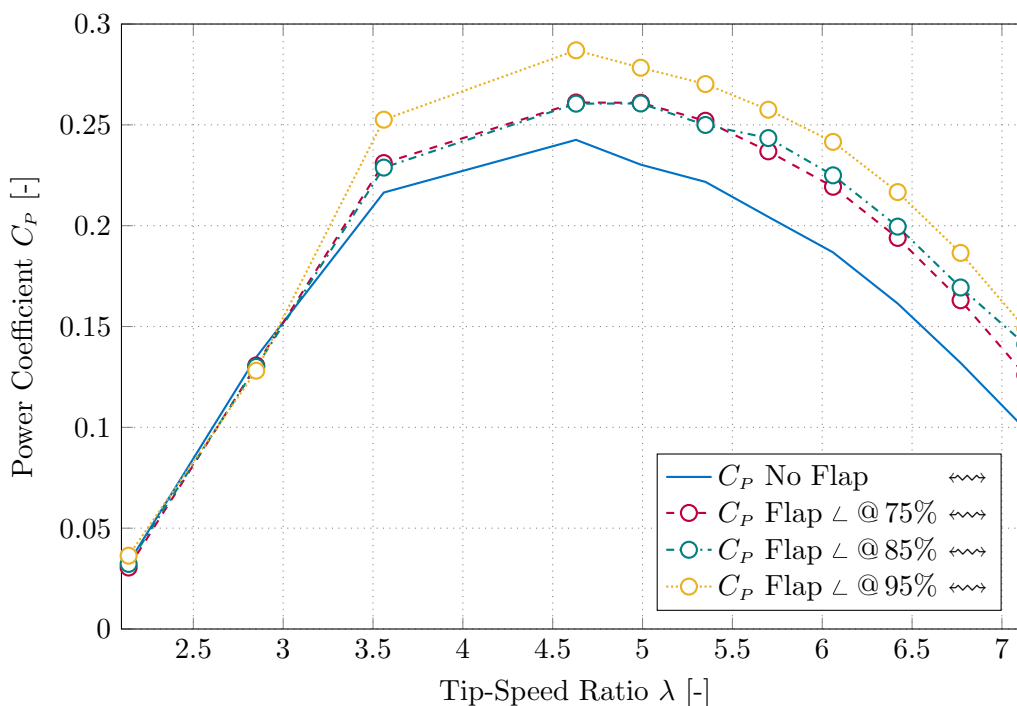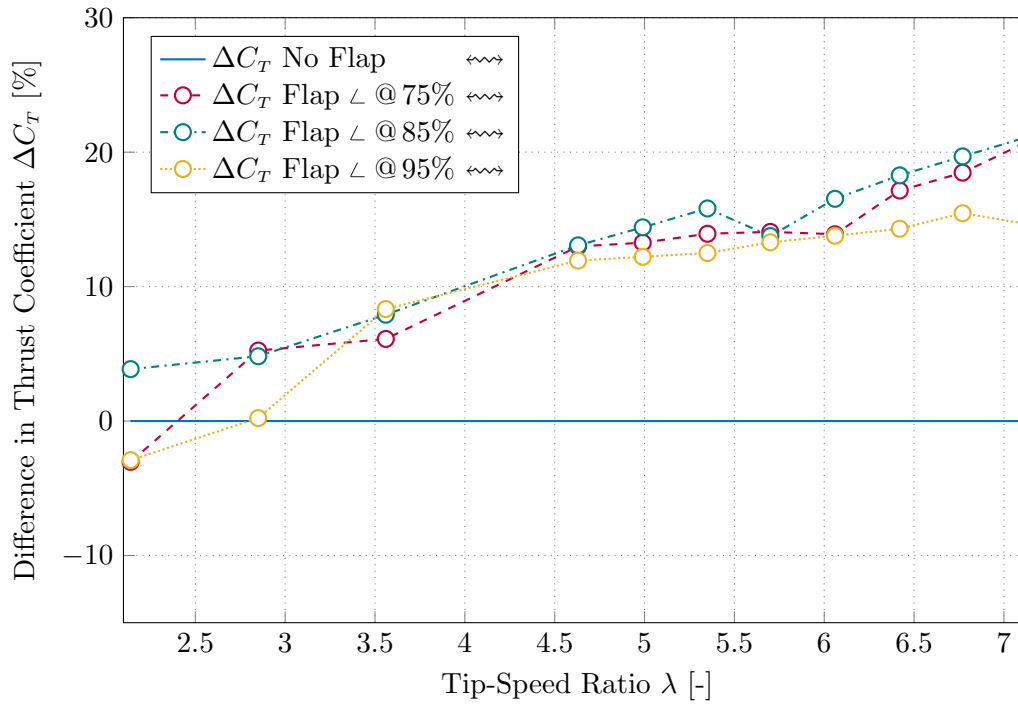

Figure 8.7: The effect of flap location on the value of C_P for Flap $\angle$
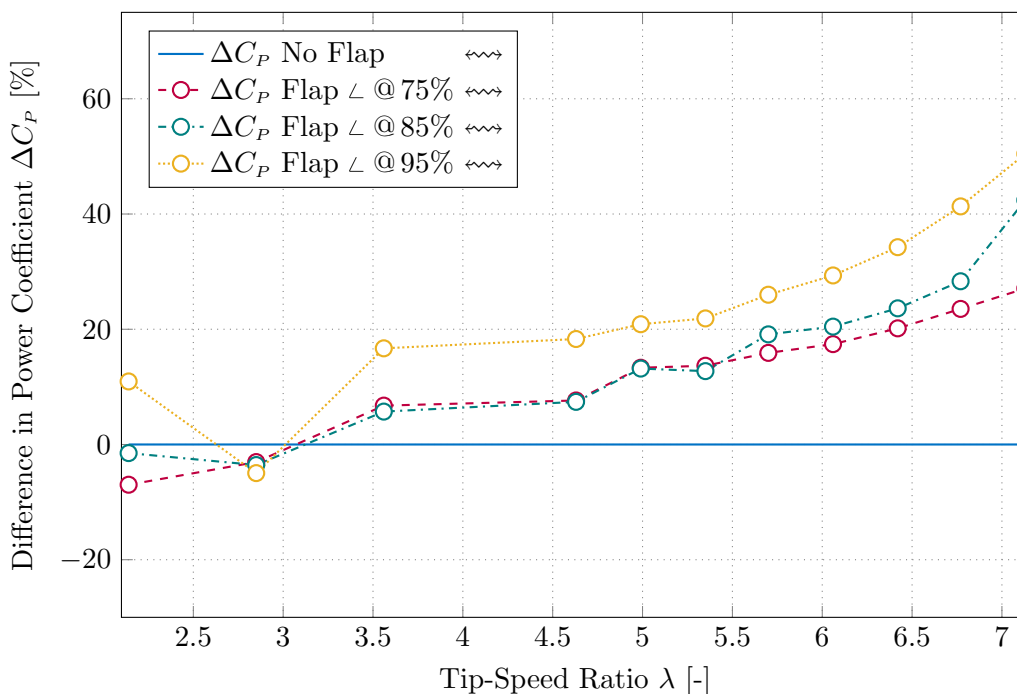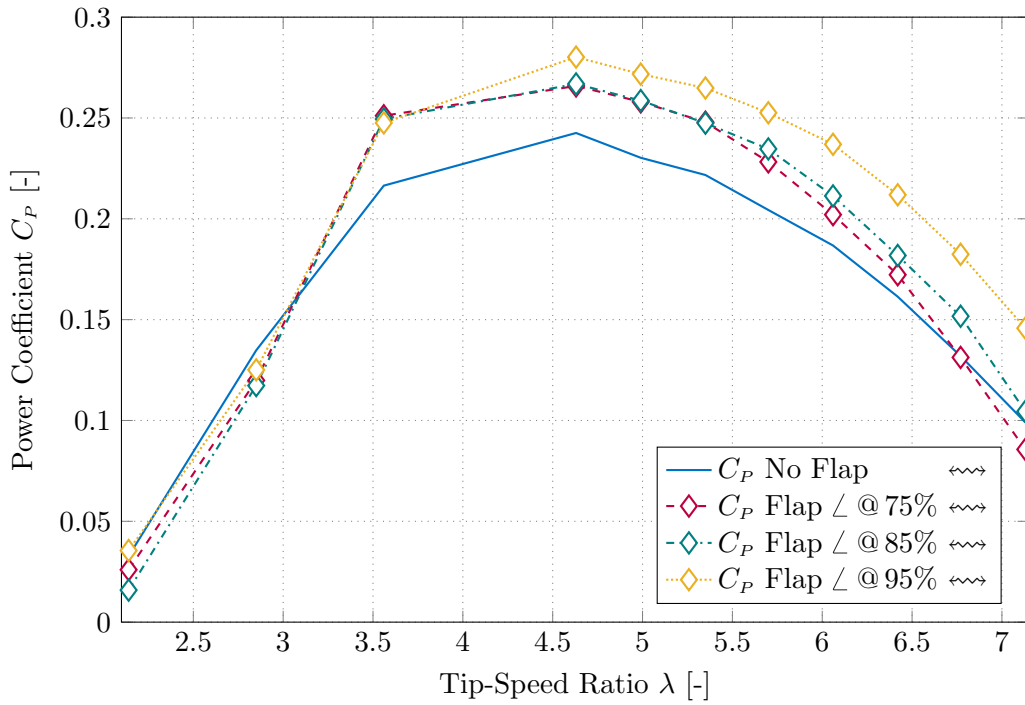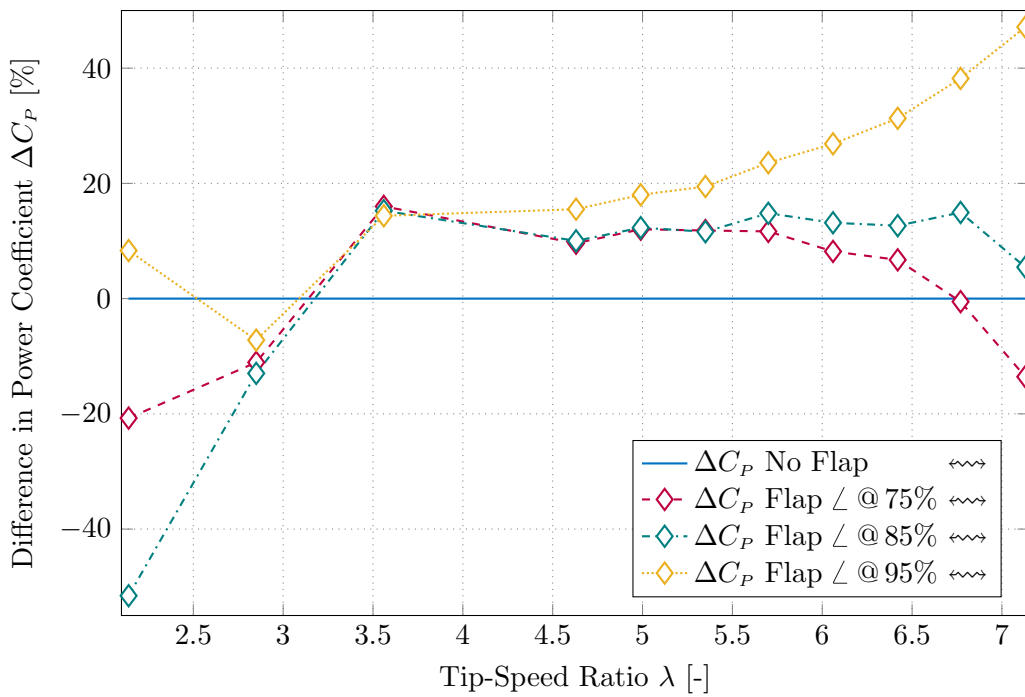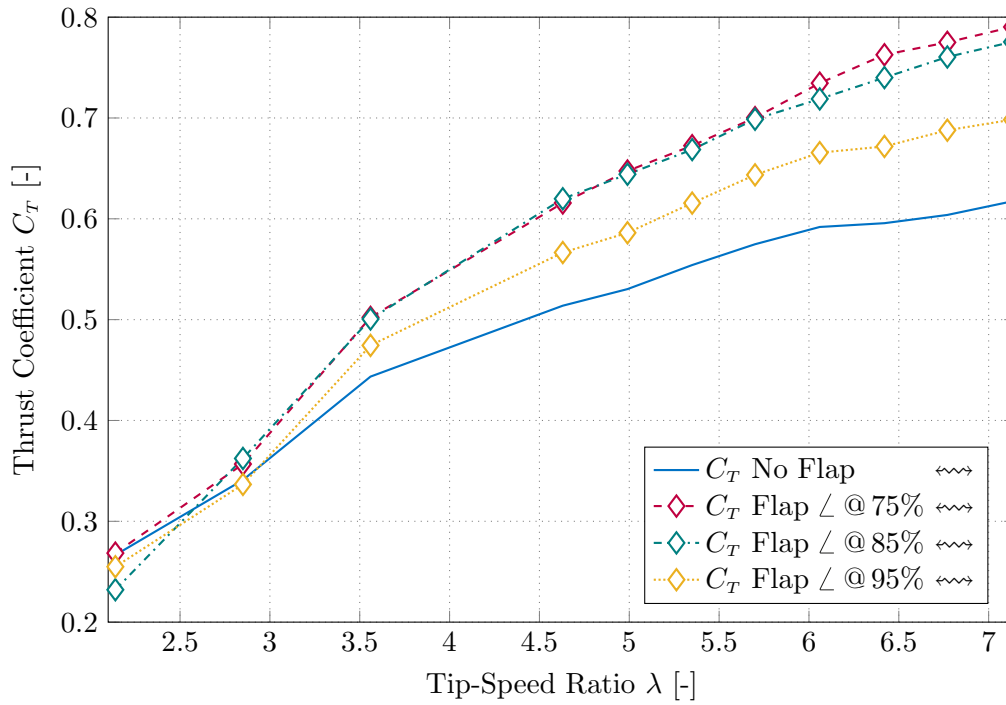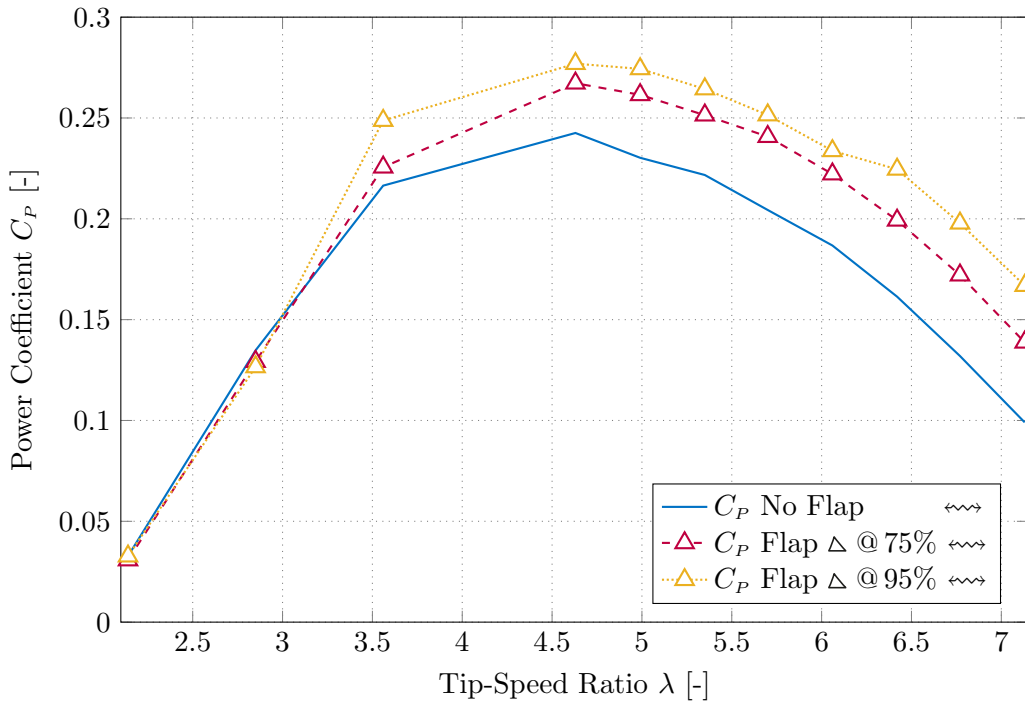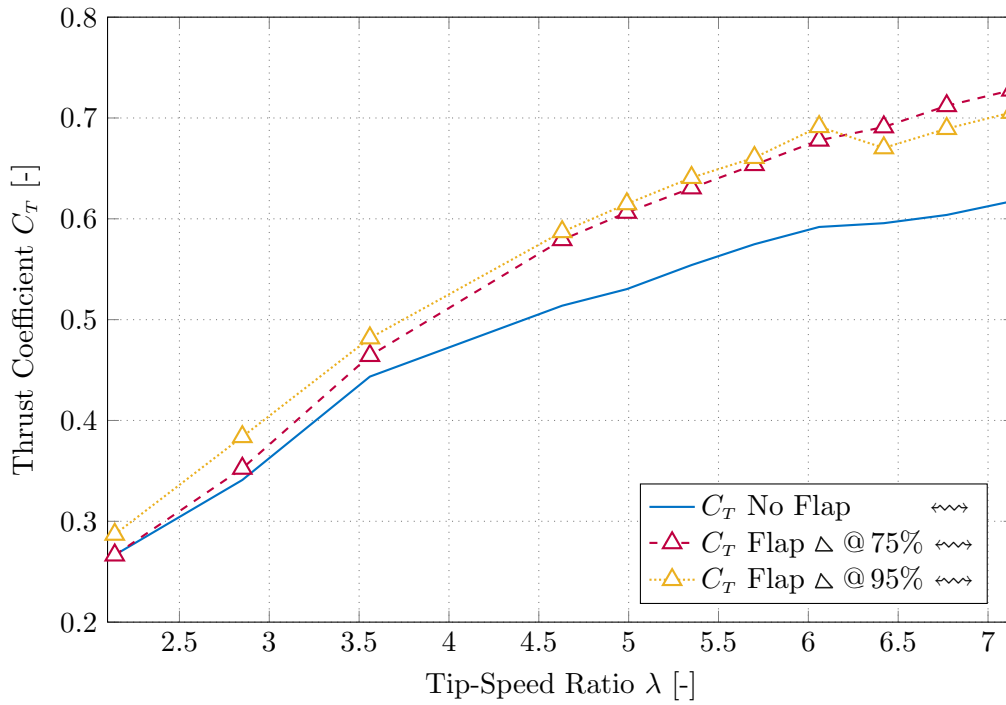

Figure 8.8: ΔC_P [%] for Flap $\angle$ as a percentage of the 'clean' No Flap case
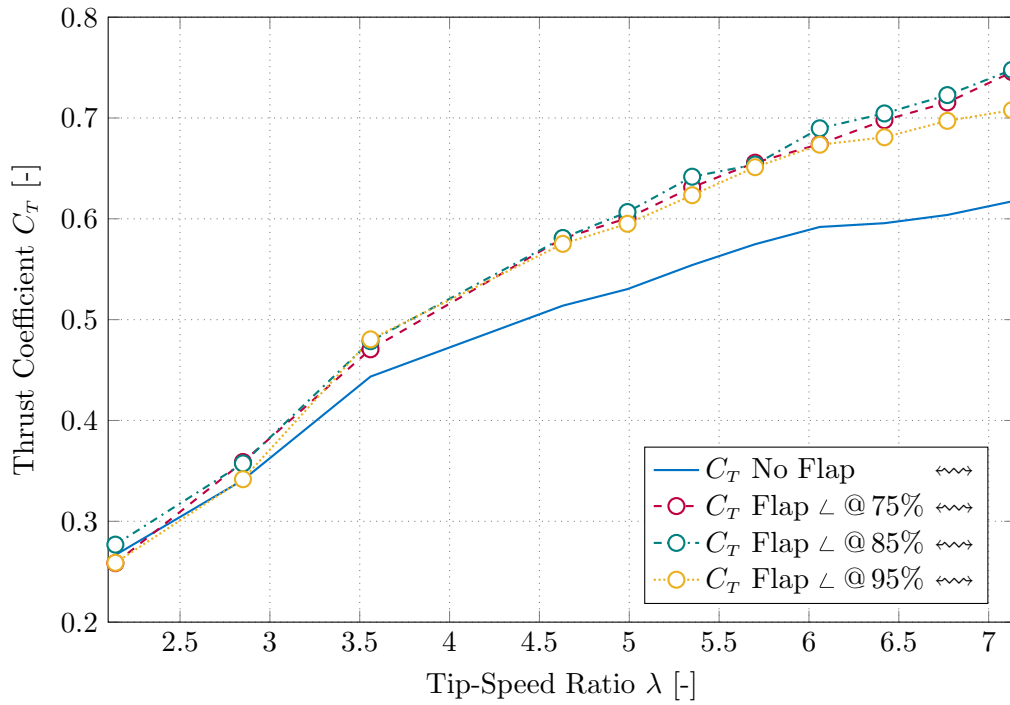
Figure 8.9: The effect of flap location on the value of C_T for Flap $\angle$

Figure 8.10: ΔC_T [%] for Flap $\angle$ as a percentage of the 'clean' No Flap case

70

Figure 8.11: The effect of flap location on the value of C_P for Flap $\angle$

Figure 8.12: ΔC_P [%] for Flap $\angle$ as a percentage of the 'clean' No Flap case

8.4   Comparison of the the different flap types

The different types of flaps were explained in section 3.4 and the exact dimensions were shown in figure 3.7. The flaps 1 $\angle$ and 3 $\triangle$ have almost similar heights, while flap 2 $\angle$ is almost twice

Figure 8.13: The effect of flap location on the value of C_T for Flap $\angle$
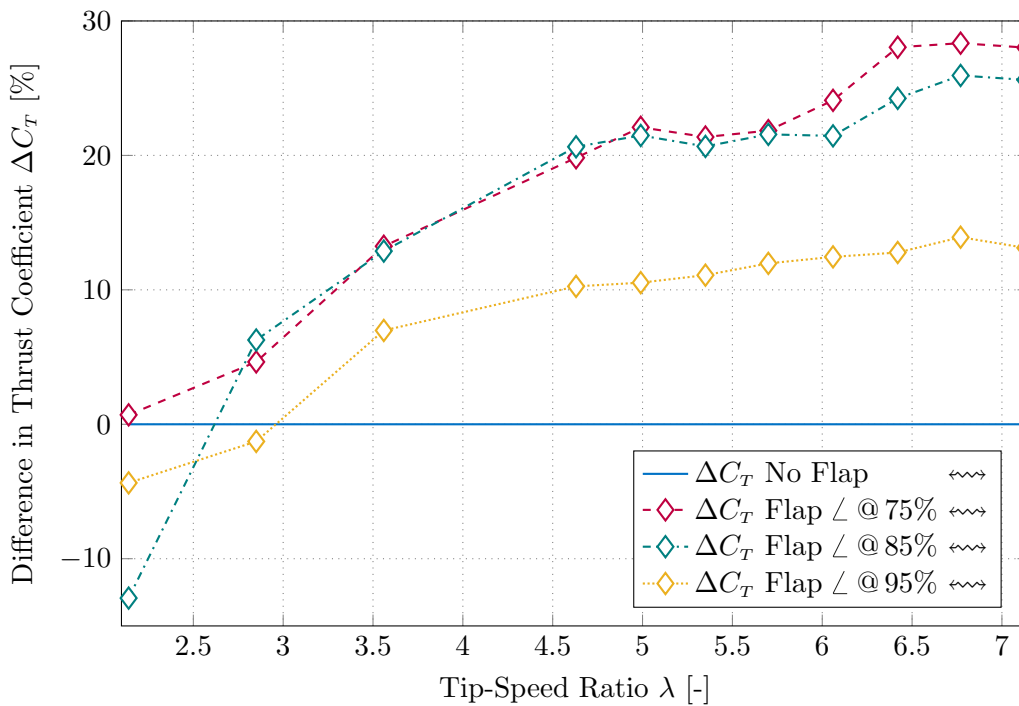
Figure 8.14: ΔC_T [%] for Flap $\angle$ as a percentage of the 'clean' No Flap case

in height. As mentioned in the previous section 8.3, the C_P and the C_T values for the shorter flaps are generally comparable and even for the taller flap 2 $\angle$ seem to get similar as the flaps move towards the trailing-edge. This effect can be observed when going from figure 8.19 to 8.23

Figure 8.15: The effect of flap location on the value of C_P for Flap △
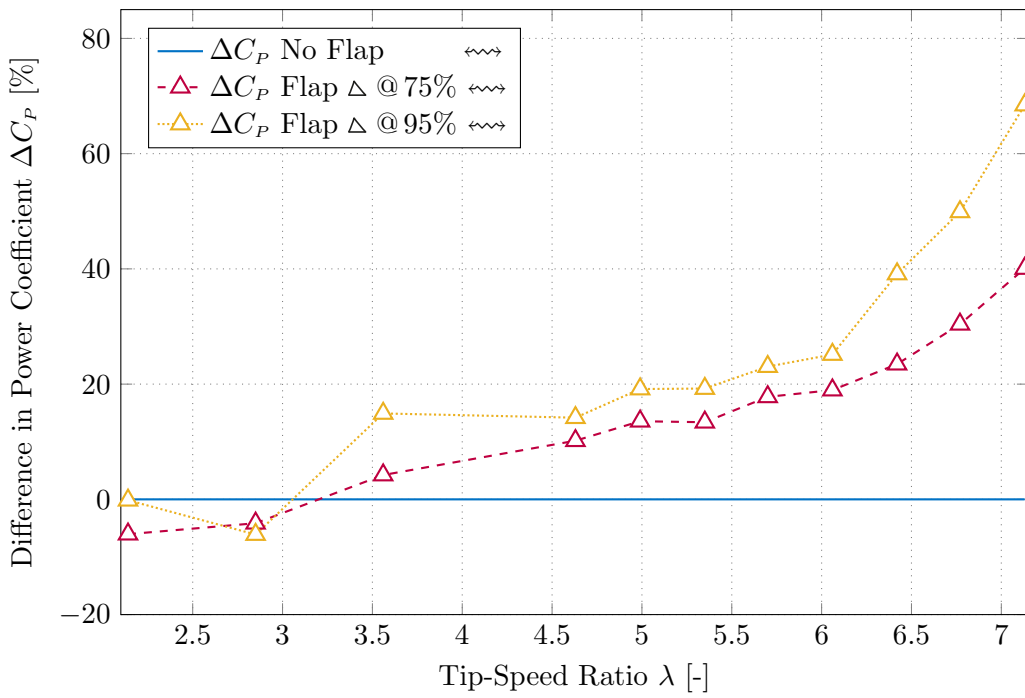
Figure 8.16: ΔC_P [%] for Flap △ as a percentage of the 'clean' No Flap case

and finally 8.27. The shape of the plots for flap 2 ∠ vary quite a lot for the three chord-wise locations, as can be seen in figure 8.12, and at 95% chord the C_P plots of all the flaps have very similar shape with the values for flap 3 △ jumping at around $\lambda_{tip} = 6$ and giving the highest values as observable from figure 8.24. It may also be concluded from this that height has less

Figure 8.17: The effect of flap location on the value of C_T for Flap $\triangle$
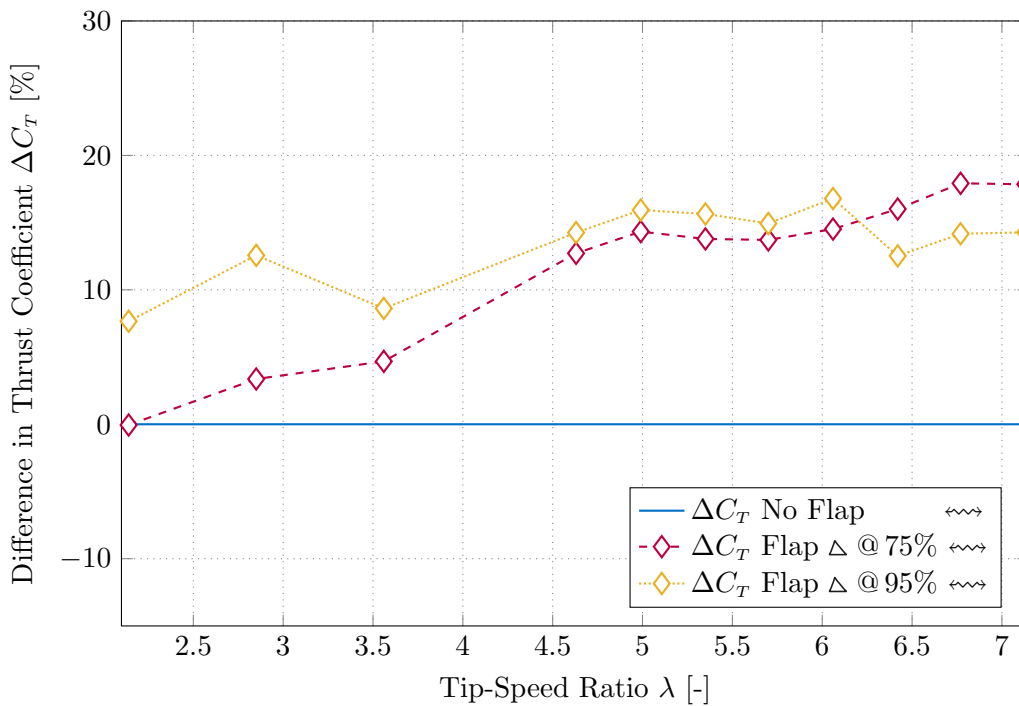
Figure 8.18: ΔC_T [%] for Flap $\triangle$ as a percentage of the 'clean' No Flap case

influence as the flaps move towards the trailing edge. Also from these plots it is clear that the peaks are similar and always occurring at $\lambda_{tip} = 4.63$ (351 rpm), which is also the value used for the stereoscopic PIV analysis.

The C_T values show a reversing pattern in relation to height as the flaps move from 75% chord to 95% chord, especially at higher λ_{tip}, which can be followed in figures 8.21, 8.25 and 8.29. The tallest flap, flap 2 $\angle$, starts of with approximately 10% higher values at 75% chord (figure 8.22) and the gap closes at 85% chord and reverses at 95% chord, where it has the lowest values. The difference, however, is not that significant and the shape of the C_T plot for flap 1 $\angle$ and flap 2 $\angle$ are practically the same (Figure 8.30).

The plots for flaps 1 $\angle$ and 3 $\triangle$ have a very similar pattern and the flap 1 $\angle$ is generally a few percentage points higher. This might be due to the slight height difference between these two flaps. The flap 2 $\angle$ at 75% chord has initially a gain of approximately 6% in comparison to the other two flaps but get almost at the same level at 95% chord, especially beyond $\lambda_{tip} \gtrsim 6$ where the C_T suddenly drops to the same level as flap 2 $\angle$.

Another aspect that might have played a role are the gaps between the sections of flap 1 $\angle$ and 2 $\angle$ as explained in section 4.4 and depicted in image 4.8. Flap 3 $\triangle$ being made of a softer material could contour much easily to the curvature of the blade and had no gaps.

Although the results of all flaps converge at 95% chord, as mentioned before and evident from figures 8.28 and 8.30, the C_T values are clearly higher and the C_P also jump at the end. Considering this the flap 3 $\triangle$ was selected for the final PIV analysis, which will be detailed in the following chapter.
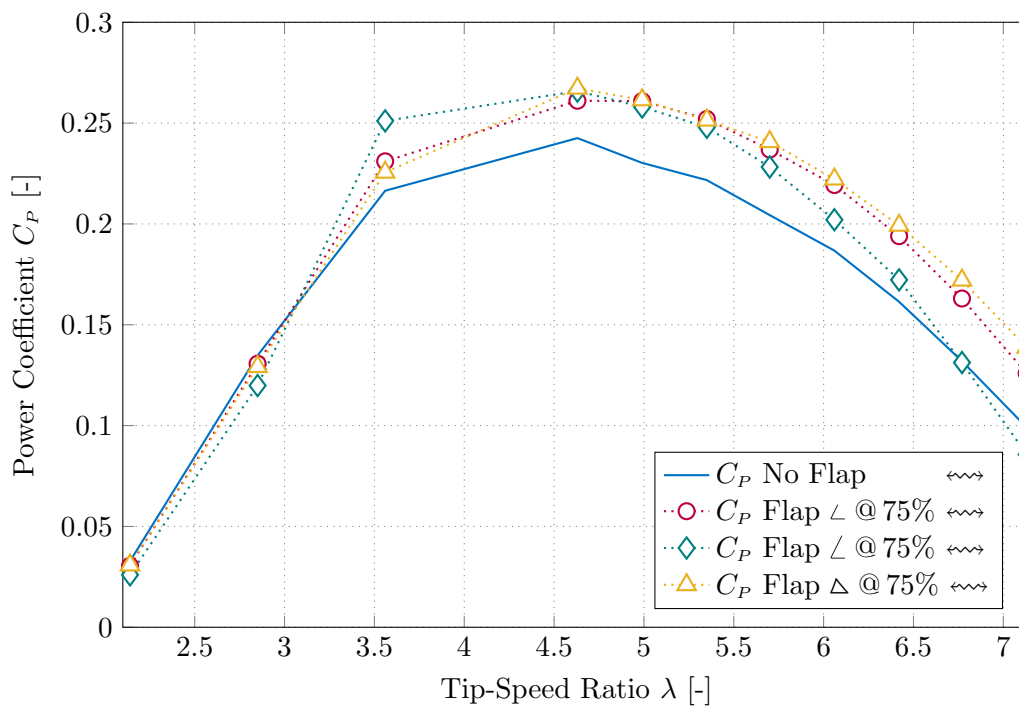
Figure 8.19: Comparing C_P of different types flaps at 75% chord location
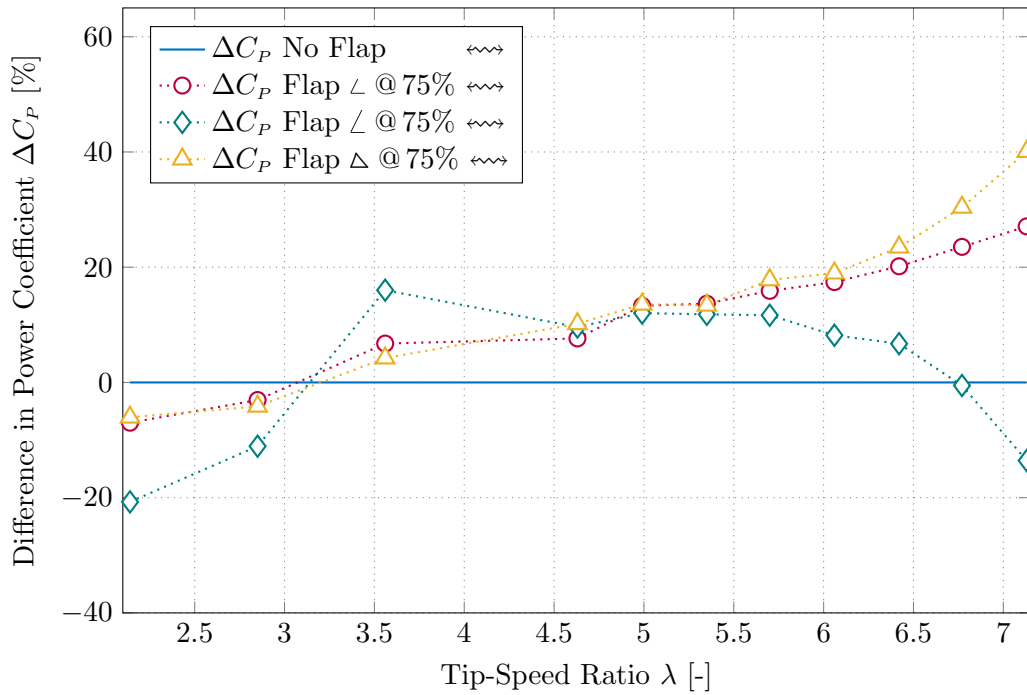
Figure 8.20: Comparison of ΔC_P as a percentage of the No Flap case for different types flaps at 75% chord location
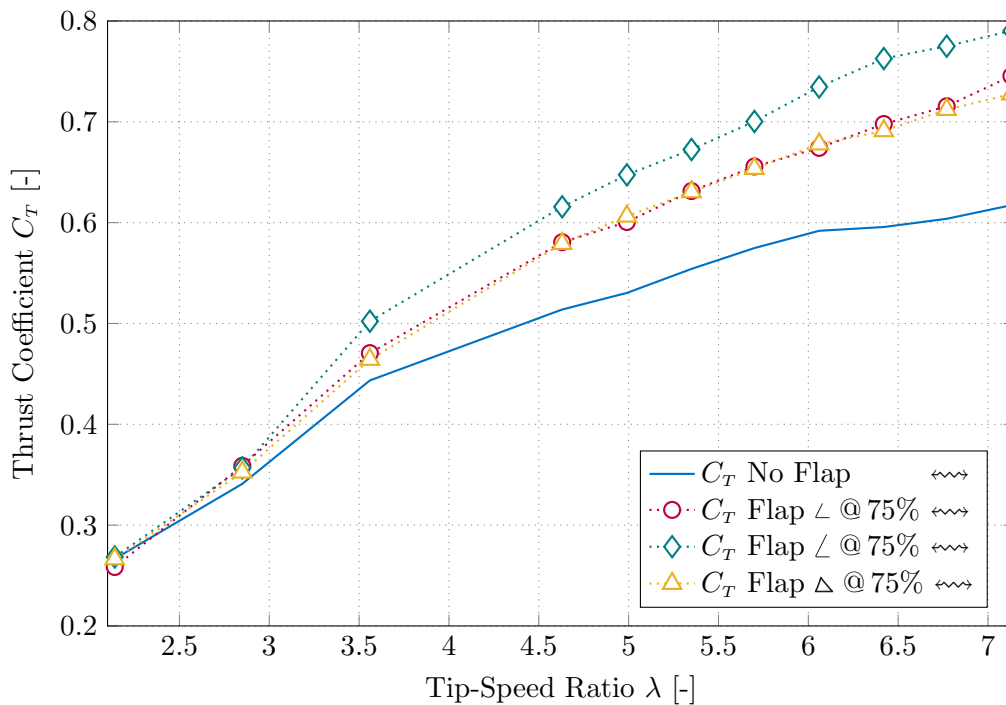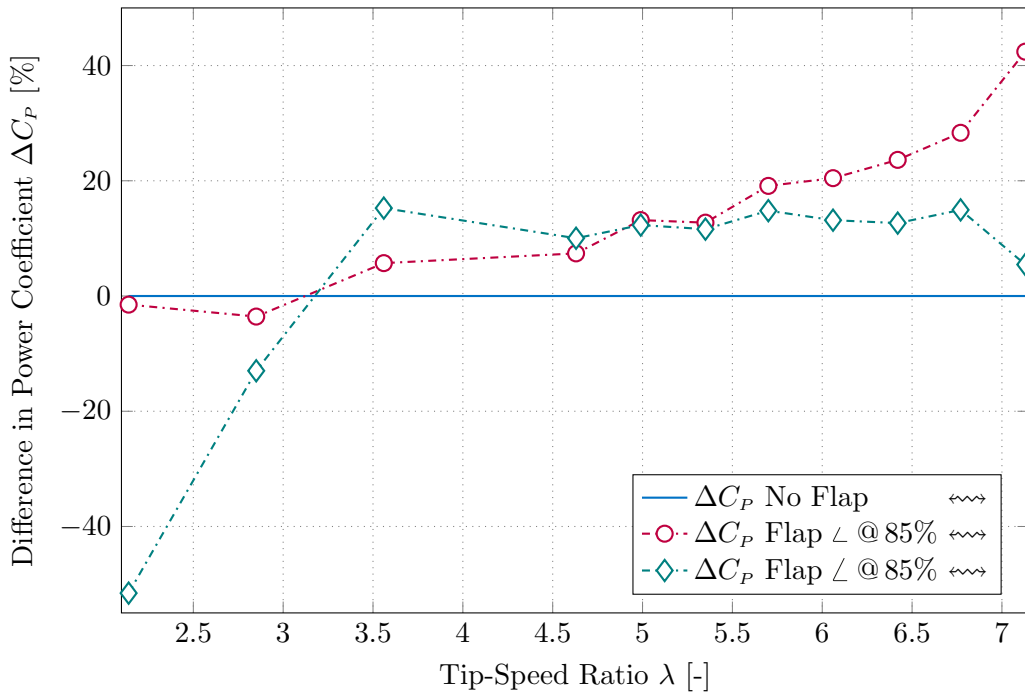

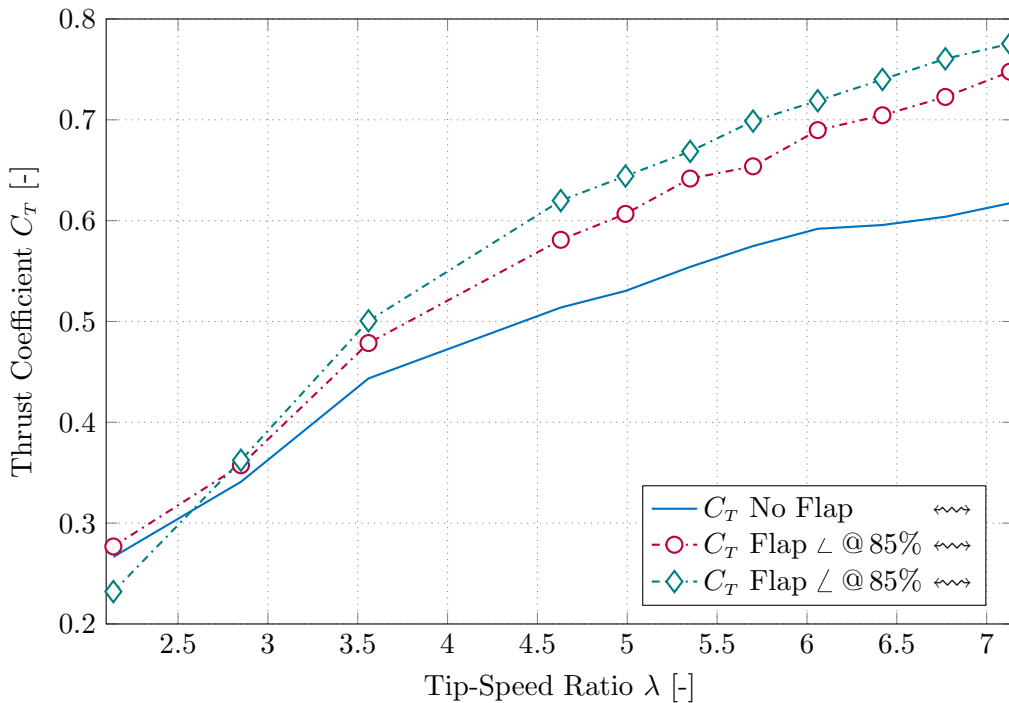**Figure 8.21:** Comparing C_T of different types flaps at 75% chord location
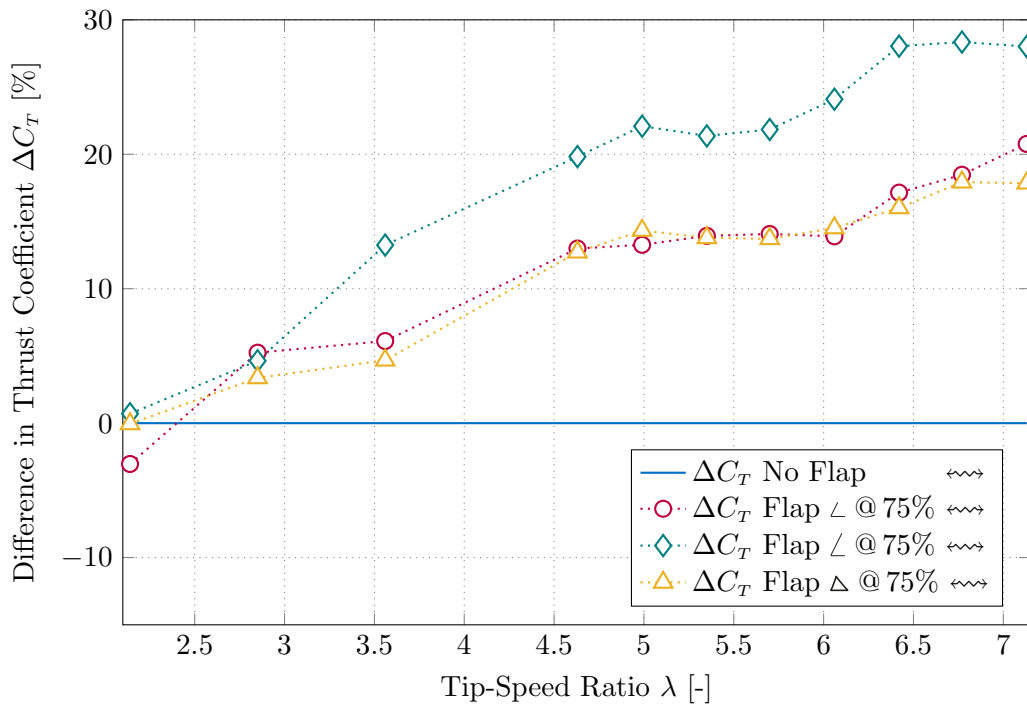
Figure 8.22: Comparison of ΔC_T as a percentage of the No Flap case for different types flaps at 75% chord location
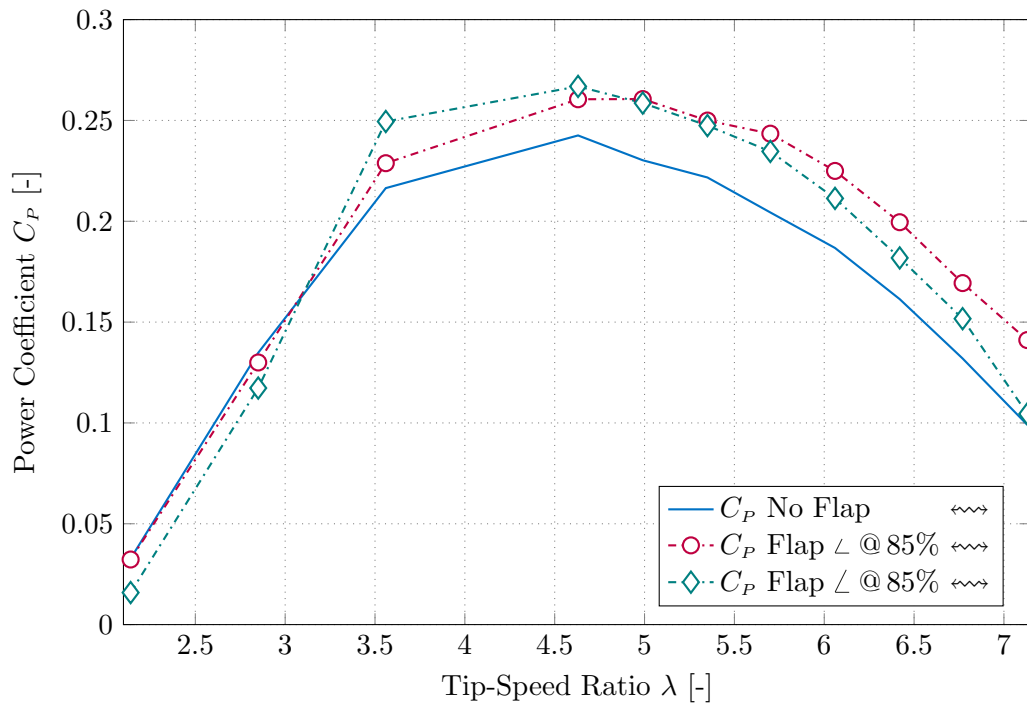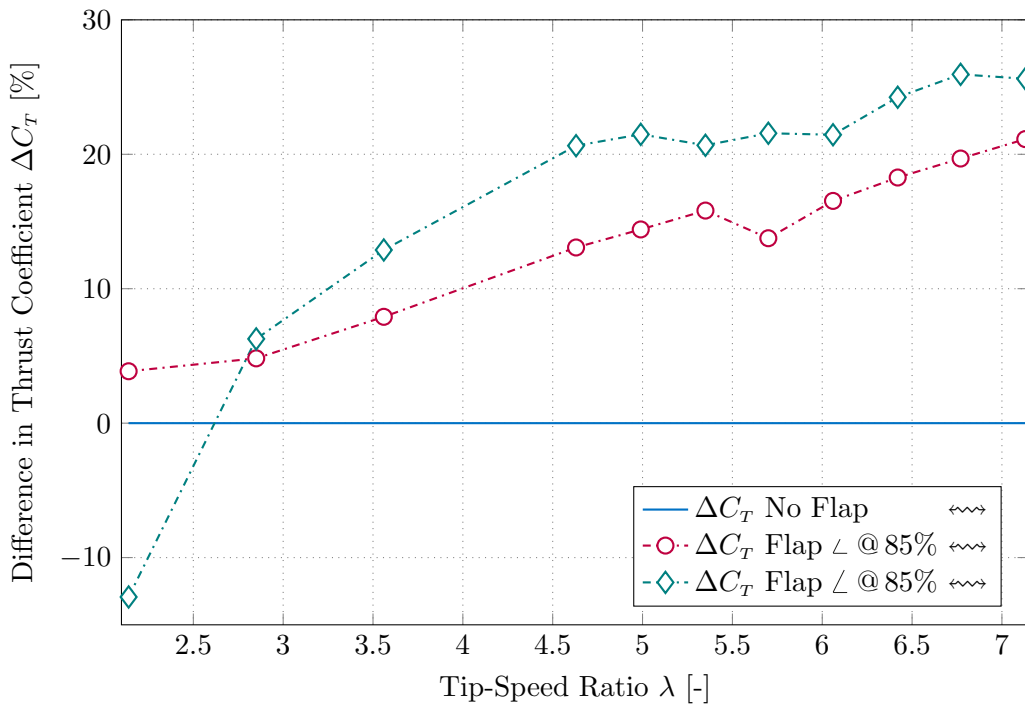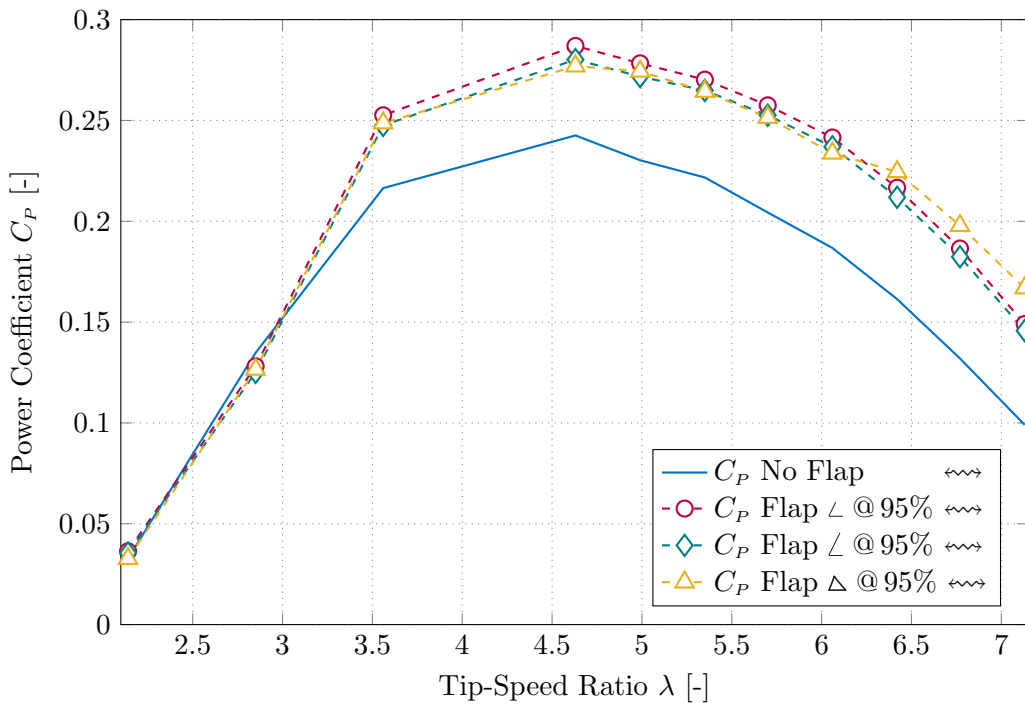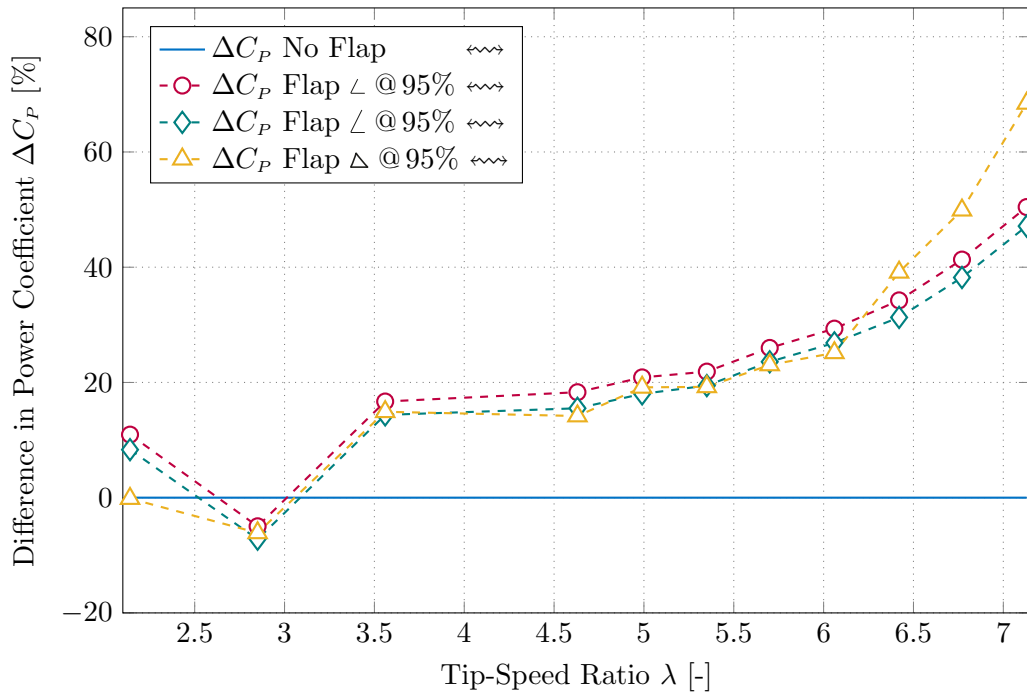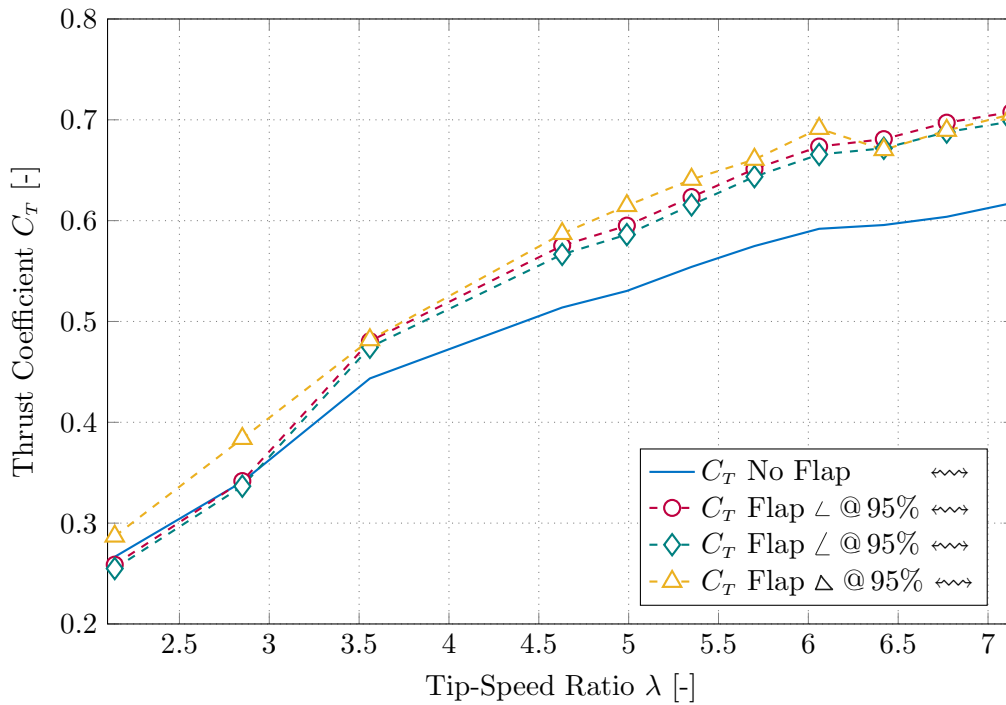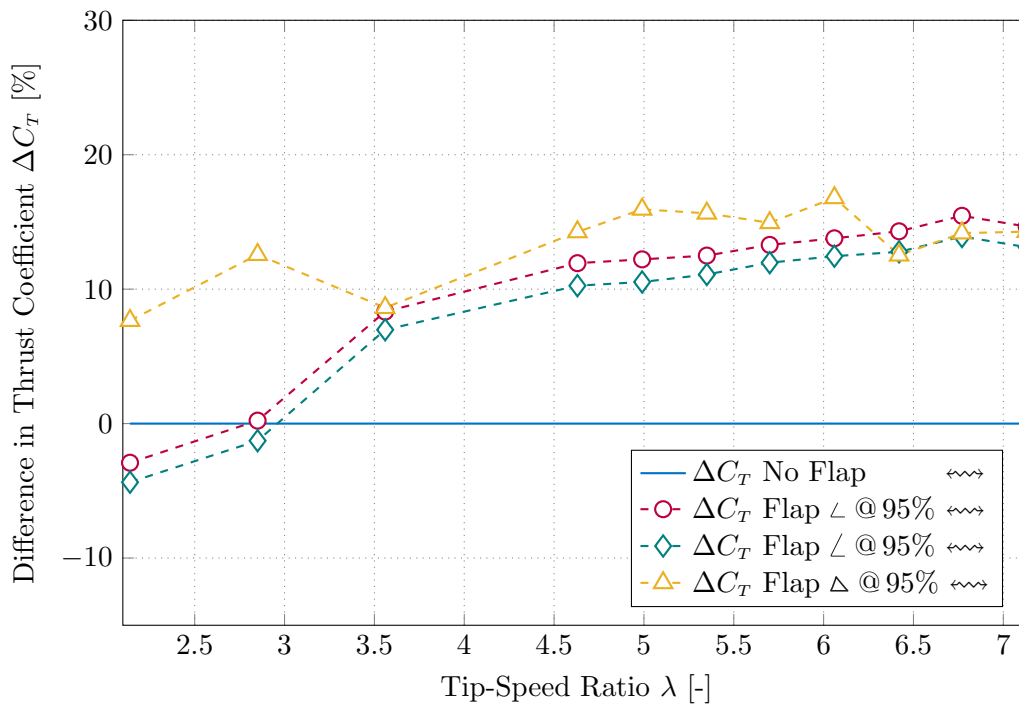

Figure 8.23: Comparing C_P of different types flaps at 85% chord location

Figure 8.24: Comparison of ΔC_P as a percentage of the No Flap case for different types flaps at 85% chord location

Figure 8.25: Comparing C_T of different types flaps at 85% chord location

Figure 8.26: Comparison of ΔC_T as a percentage of the No Flap case for different types flaps at 85% chord location

Figure 8.27: Comparing C_P of different types flaps at 95% chord location

Figure 8.28: Comparison of ΔC_P as a percentage of the No Flap case for different types flaps at 95% chord location

Figure 8.29: Comparing C_T of different types flaps at 95% chord location

Figure 8.30: Comparison of ΔC_T as a percentage of the No Flap case for different types flaps at 95% chord location

Chapter 9

Analysis of the PIV Data
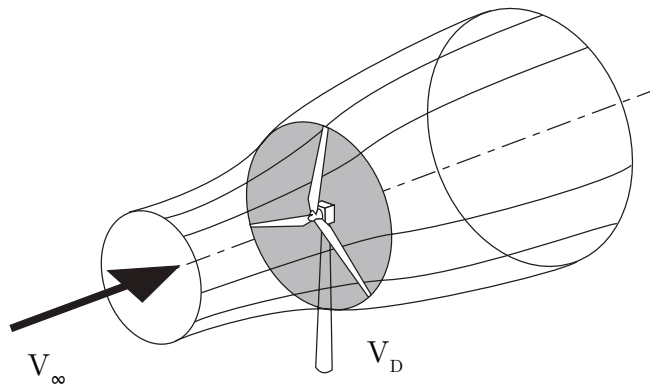
Figure 9.1: Stream-tube of a Wind Turbine [8]

From the momentum theory, also known as the disk actuator theory, the velocity at the turbine is related to the incoming velocity as;

$$V_D = V_\infty(1 - a) \tag{9.1}$$

Where a is the axial induction factor and is related to the C_T:

$$T = \frac{1}{2}\rho A V_\infty^2 [4a(1 - a)] \tag{9.2}$$

The C_T of the PIV configuration, as explained in section 6.2, was calculated using the load measurements and can be seen in figure 8.17. For the constant rpm of 351, relating to $\lambda_{tip} = 4.63$,

the value of $C_T = 0.5871$ was measured and calculated for the flap configuration used for the PIV analysis. Using this value and equation 9.2, the following quadratic equation can be derived;

$$C_T = 4a(1-a) \Rightarrow a^2 - a + \frac{C_T}{4} = 0 \qquad (9.3)$$

Solving for a (in matlab using; `roots([1 -1 0.5871/4])`) yields two results and only one is a reasonable value, namely, $a \cong 0.1787$. From this value and equation 9.1, a value of $V_D = 6.57 \text{m s}^{-1}$ was calculated at the rotor.

9.1 Velocity fields from the PIV analysis

To understand the behavior of flow around the blade, multiple sectional planes were selected and a phase-locked PIV analysis was carried out at these r/R locations. These locations were detailed in section 6.2 and listed in table 6.2. Not all span-wise locations in-and-outside the region designated for flap were analysed for the no-flap blade configuration due to time limitations. The data-actuation for the flapped case was carried out first, as starting directly after the load measurements, the blade was already configured with the flaps.

The original plan consisted of starting the data acquisition with the pressure-side and then moving the set-up and collecting the suction-side data. However, due to delays as a result of various technical issues during the experiments, only the data acquisition for the pressure-side could be completed. It is therefore important to mention that the plots in this chapter only paint half the picture and the discussion based on these results also tell only half the story.

In order to non-dimensionalize the value of V_x the value of V_D was used. The x direction is (parallel to V_∞).

$$\frac{V_x - V_D}{V_D} \qquad (9.4)$$

The values of V_y and V_z were non-dimensionalized simply by dividing by V_D as they are generally small and centered approximately around zero. The y-axis is parallel to the rotational plane of the blade where as the z-axis is parallel to the blade. The axes can be clearly visualized in figures 9.21, 9.22, 9.23, 9.18, 9.19 or 9.20.

Starting with $r/R = 0/9$ it can clearly be seen from figure 9.2 that velocities around the blade, and especially V_x are higher and become smaller when going towards the root as evident from figure 9.21. This could be due to the higher rotation speed which is higher with higher r/R values.

Almost for all r/R locations in the V_x velocity fields there is an area of low velocity around the cropped region (this crop was needed to remove the reflection of the tripping wire), which is around the stagnation point and this is also confirmed by the streamline analysis in section 9.2. Moving south-east towards the leading-edge of the blade, the flow experiences a sharp velocity increase, which is understandable as the flow has to go around the leading-edge and has to succumb the sharp curvature of the leading-edge. On the other side towards the middle of the blade, the flow also experiences a higher velocity but this region is not as dark as the leading-edge for V_x, indicating generally lower velocities in this region. The stagnation region also get larger while moving towards the root from the tip for both the flapped and no-flap configurations.
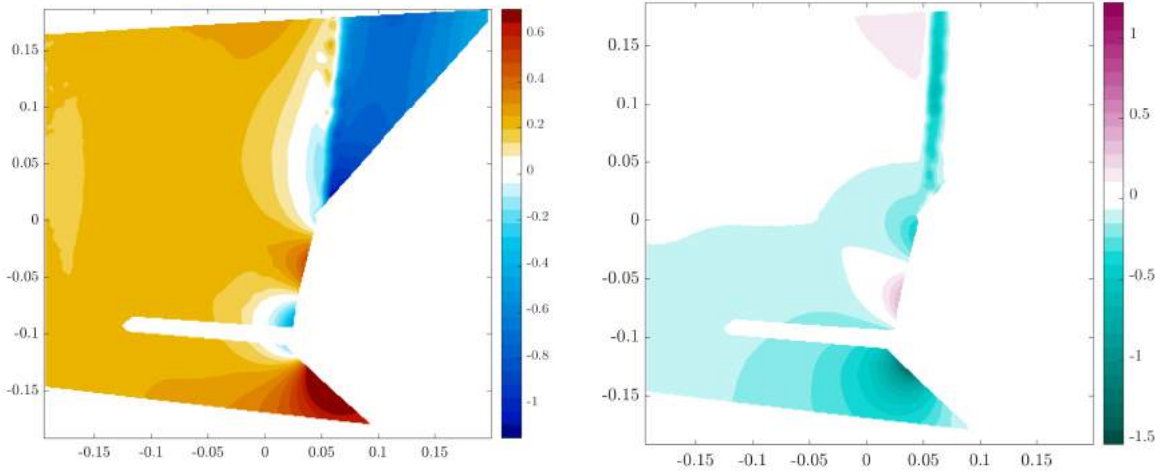
(a) Velocity field V_x as a function of V_D pressure side
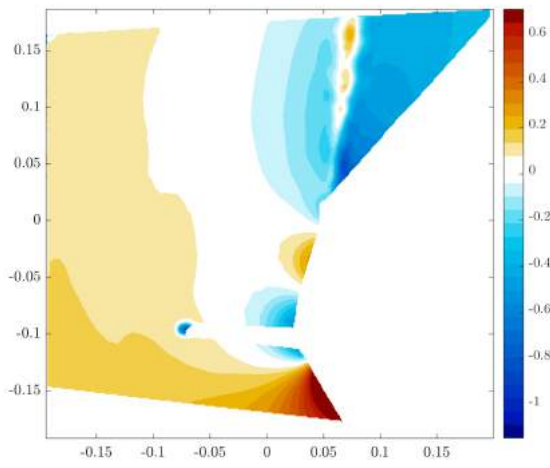
(b) Velocity field V_y/V_D pressure side

Figure 9.2: Velocity fields for V_x & V_y at $r/R = 0.9$

This region, however, seems to be larger for the flapped cases. The high-velocity region is more prominent in the non-flapped configuration and seems to have moved more towards the trailing-edge when comparing figures 9.18 and 9.21. For r/R values of 0.9, $0.8, 0.7 \& 0.57$ the trailing edge vortex sheet is clearly discernible in figures 9.2, 9.3, 9.4 and 9.5, respectively. The thickness of the sheet however, seems to be for higher for lower r/R values.

Comparing the V_x and V_y velocity fields at $r/R = 0.57$ in the sub-figures of 9.5, it can be confirmed that the flow is very similar for both the flapped and no-flap configurations. The assumption, that the flow 'far' outside the flap region is comparable for both configuration, is therefore valid. As the flaps was placed at the root region, the inboard outside the flap area is not that far is therefore, still under the influence of the flaps as can be in figure 9.15 for $r/R = 0.26$ where for the flapped-configuration the same larger lower velocity region around the stagnation point can be observed followed by the smaller high velocity region, as elaborated in the preceding paragraph.

For regions just outside the flap region namely, $r/R = 0.48$ outboard and $r/R = 0.3$ inboard, the higher intensity and more concentrated vortex is clearly evident in figures 9.6 and 9.14, respectively. The strength of V_x vortex is higher at $r/R = 0.31$ which can be attributed to the higher rotation speed in comparison to the $r/R = 0.48$. This vortex is also visible in the flapped regions $0.31 < r/R > 0.46$ but seems to be moving in a circular pattern as direction of the V_x vortex changes around $r/R = 0.34 \& 0.36$.

Comparing the V_z plots in figures 9.20 and 9.23, it can be observed that presence of the flaps increases the flow towards the outboard direction and unlike the V_x and V_y velocity fields at $r/R = 0.57$ the V_z velocity field for the flap configuration has slightly high flow in the positive z direction i.e. towards the tip of the blade.
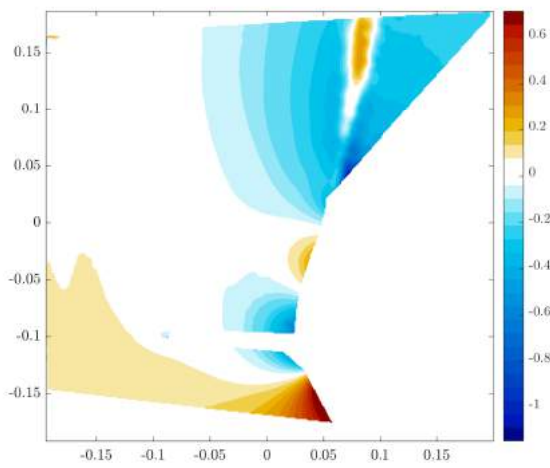
(a) Velocity field V_x as a function of V_D pressure side
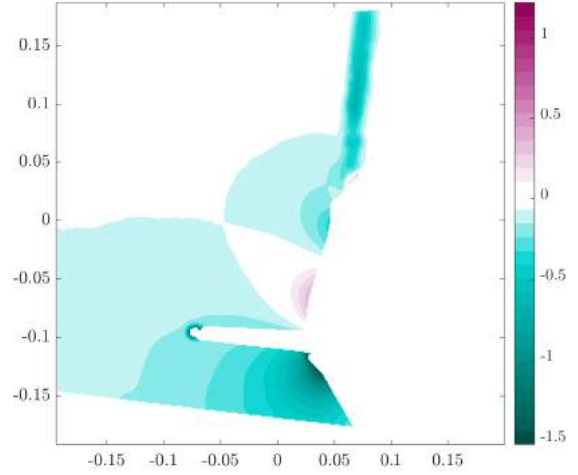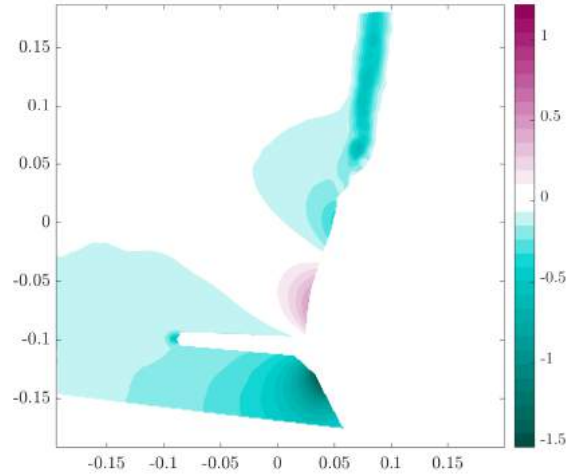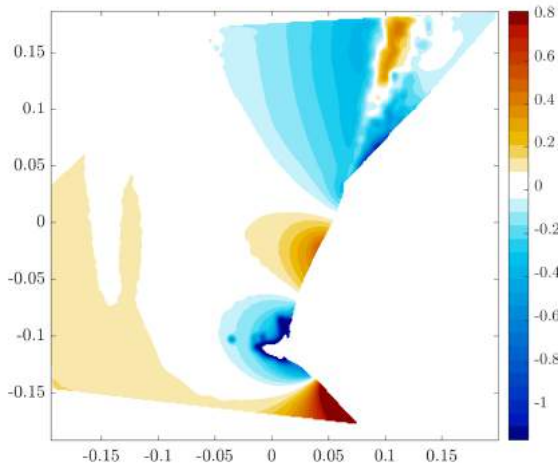
(b) Velocity field V_y/V_D pressure side

Figure 9.3: Velocity fields for V_x & V_y at $r/R = 0.8$

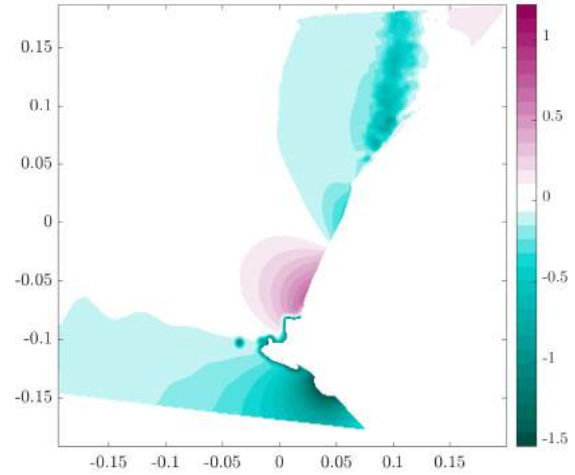**(a)** Velocity field V_x as a function of V_D pressure side
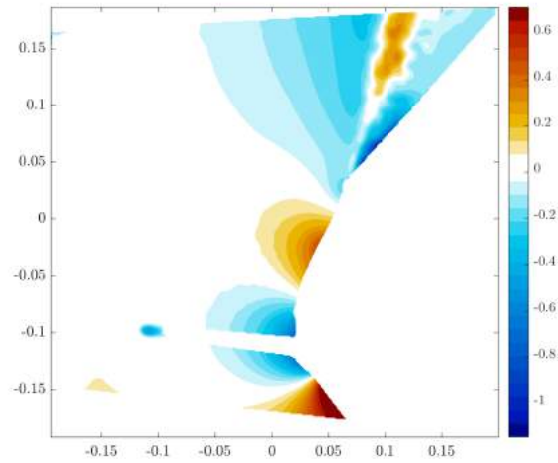
(b) Velocity field V_y/V_D pressure side

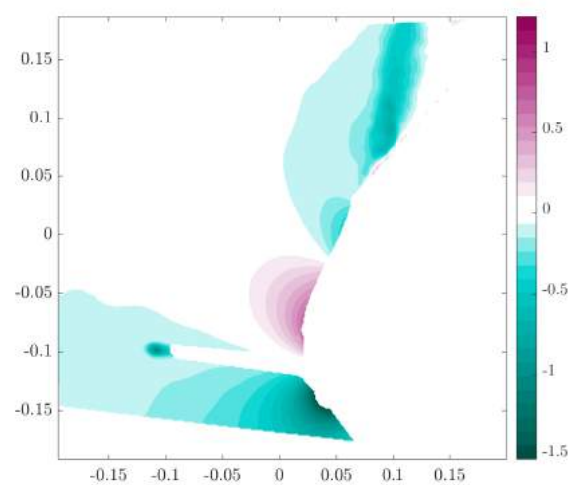**Figure 9.4:** Velocity fields for V_x & V_y at $r/R = 0.7$

(a) Velocity field V_x as a function of V_D pressure side

(b) Velocity field V_y/V_D pressure side

(c) Velocity field V_x as a function of V_D pressure side with flap

(d) Velocity field V_y/V_D pressure side with flap

Figure 9.5: Velocity fields for V_x & V_y $r/R = 0.57$ with and without flap

9.2   Stagnation point along the blade

LaVision® DaVis software offers the ability to visualize the streamlines of the flow. This visual analysis was carried out at multiple r/R locations both for planar and stereoscopic results to find out the locations of the stagnation point across the blade. This is presented in figure 9.24 where three r/R locations, namely 0.17, 0.57 and 0.9 are presented for both planar and stereoscopic cases. The results indicate the location of the stagnation point generally in the same area. The 0.17 and 0.9 r/R points clearly show that the stagnation occurs at the location where the tripping wire was placed. This would practically render the zigzag tape on the pressure-side ineffective for the λ_{tip} used for the PIV analysis. For 0.57 r/R, the stagnation point seems to be slightly above the location of the zigzag tape.
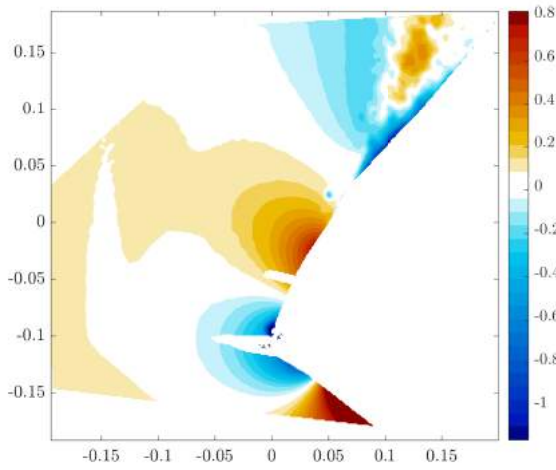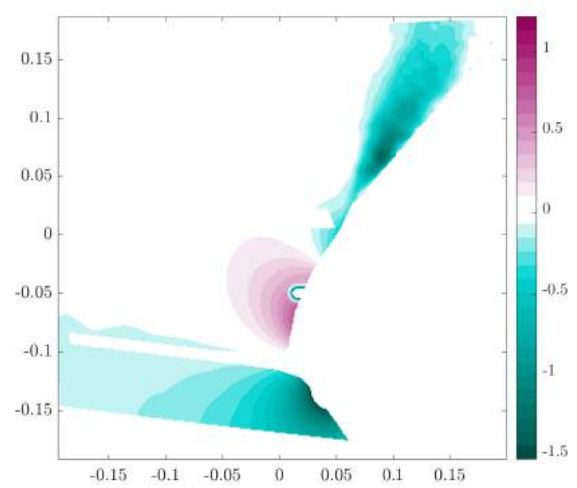
(a) Velocity field V_x as a function of V_D pressure side
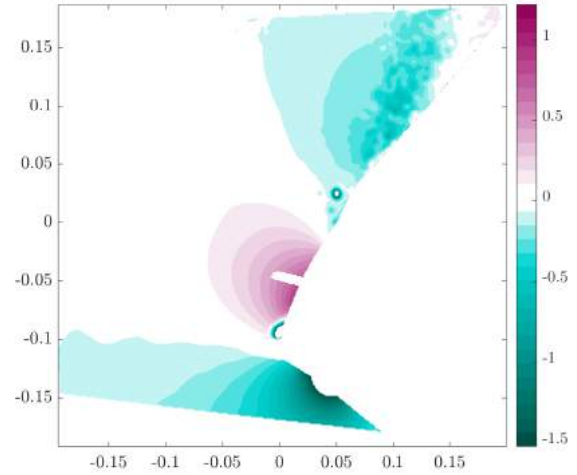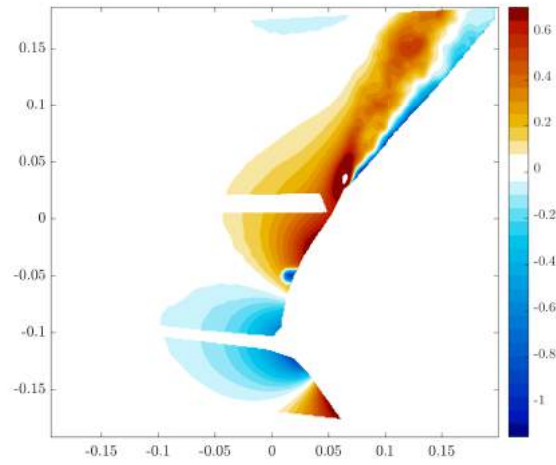
(b) Velocity field V_y/V_D pressure side

(c) Velocity field V_x as a function of V_D pressure side with flap

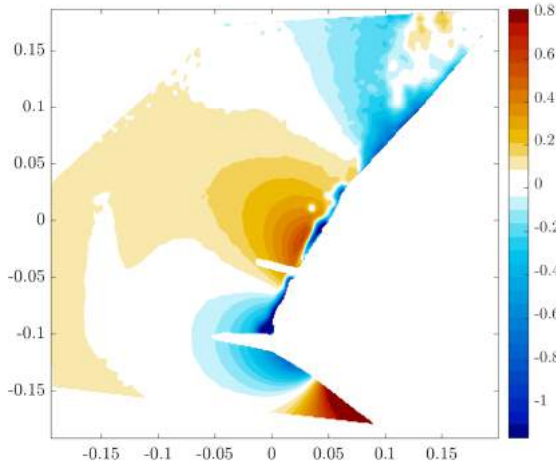**(d)** Velocity field V_y/V_D pressure side with flap

Figure 9.6: Velocity fields for V_x & V_y $r/R = 0.48$ with and without flap

9.3 Effect of manufacturing imperfections

The Small bump on the blade between $0.46 - 0.48$ r/R as explained in section 3.3.1 was in line with the chord and relatively small in size and from the figures 9.7 and 9.6 not an significant effect on the flow is observed. Therefore it can be concluded that the effects can be neglected.

The joining-line $r/R \lesssim 0.57$ also explained in section 3.3.1 similarly seems to have no effect on the flow but did effect the quality of the images captured due to the extra reflect light from it. This was dependent on the curvature of the blade and mainly effected the results at $r/R = 0.46$ & 0.48 as can be observed in figures 9.7 and 9.6.
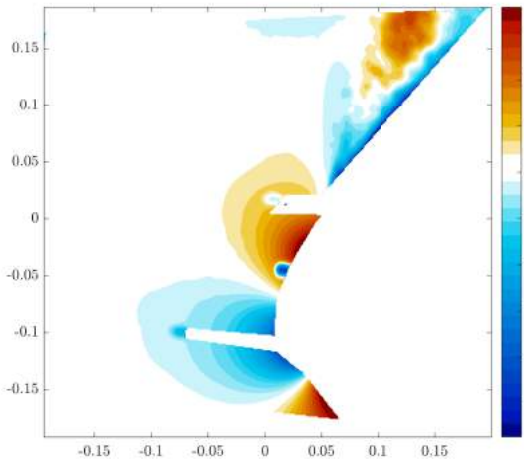
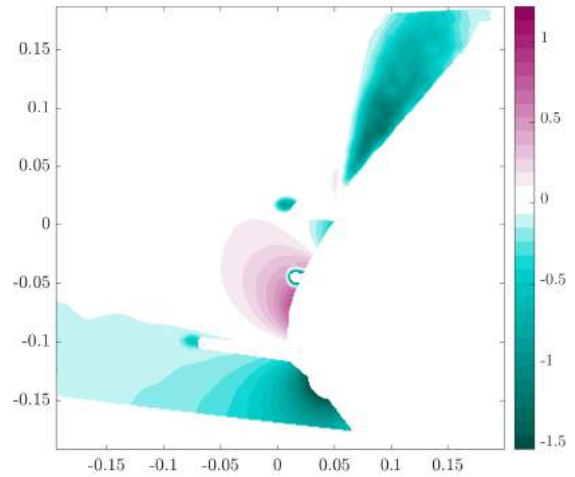The foam material used for the transition part did not have a smooth surface and therefore

(a) Velocity field V_x as a function of V_D pressure side no flap
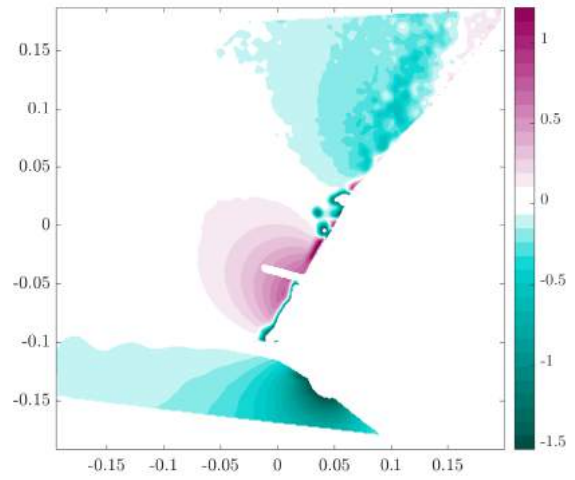
(b) Velocity field V_y/V_D pressure side no flap

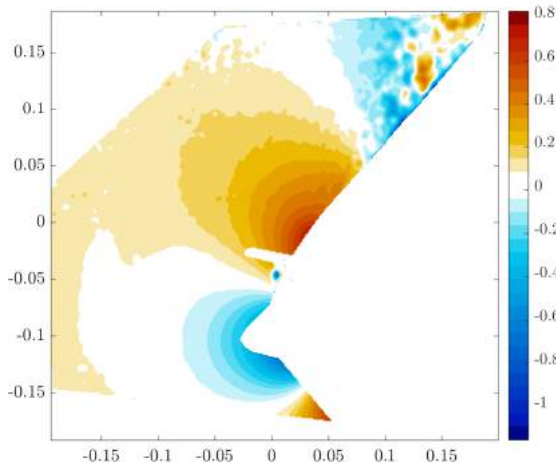**(c)** Velocity field V_x pressure side with flap

(d) Velocity field V_y/V_D pressure side with flap

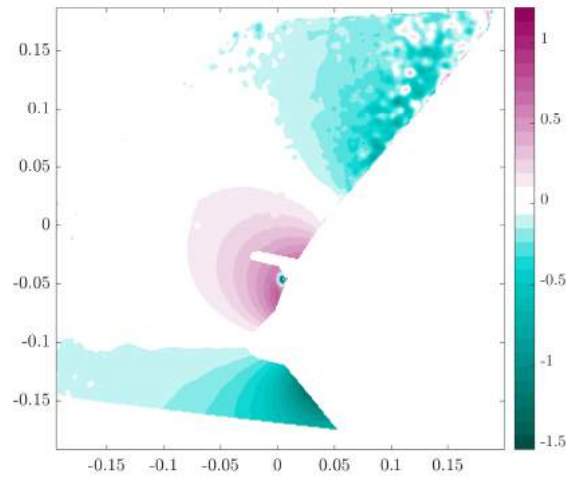**Figure 9.7:** Velocity fields for V_x & V_y at $r/R = 0.46$ with and without flap

dispersed light and

9.4 Effect of painting the tripping wire

The tripping wire is made of glossy plastic material and therefore reflects the laser light and in order to reduce this reflection for better results, it was painted black. This was explained in section 4.6 and furthermore a wrong type of paint was used, i.e. the paint that was not matt. Table 6.3 list all the measurement point for the PIV analysis and all cases with painted are indicated with a tick-mark in the second column. Two cases from table 6.3, namely cases 10 and 13 can be directly compared as both had the exact same configuration. This comparison is
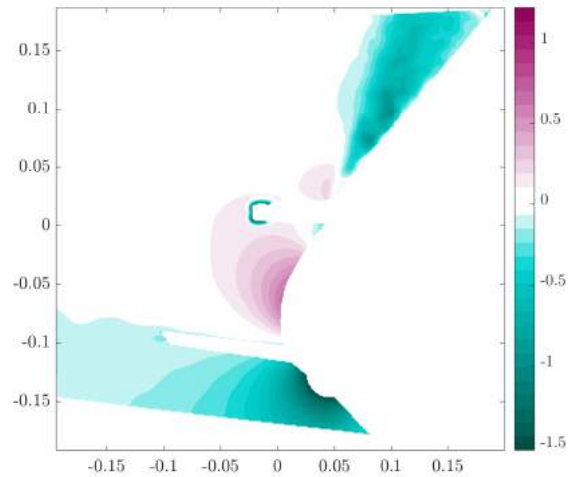
(a) Velocity field V_x as a function of V_D pressure side no flap

(b) Velocity field V_y/V_D pressure side no flap
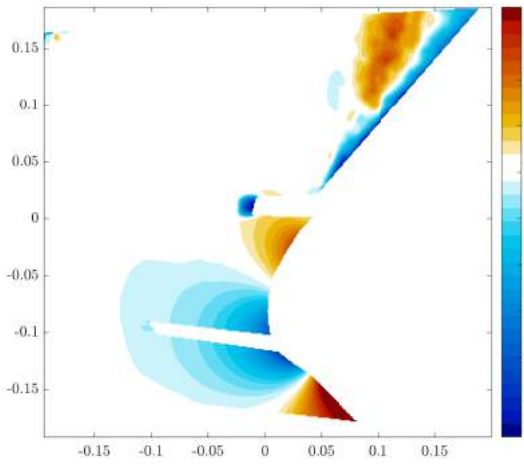
(c) Velocity field V_x as a function of V_D pressure side with flap
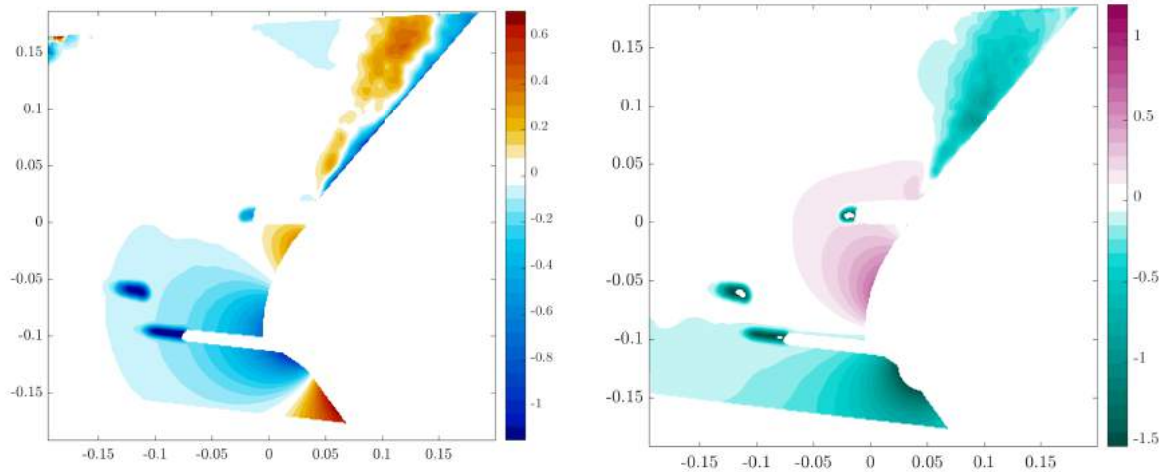
(d) Velocity field V_y/V_D pressure side with flap

Figure 9.8: Velocity fields for V_x & V_y at $r/R = 0.42$ with and without flap

given by figure 9.15, where the differences seem be almost negligible. However for other cases including the sub-figures 9.15a and 9.15b it can seen that a larger area needed to be cropped around the tripping-wire.

9.5 Effects of smoke inconsistency

Smoke/fog is an essential ingredient of the PIV analysis as it reflects the light being captured by the cameras. The right consistency of the air/fog mixture is crucial.

The fog machine was refilled and fog was injected into the flow after case 19, as given in table

(a) Velocity field V_x as a function of V_D pressure side   **(b)** Velocity field V_y/V_D pressure side

Figure 9.9: Velocity fields for V_x & V_y at $r/R = 0.38$ with flap
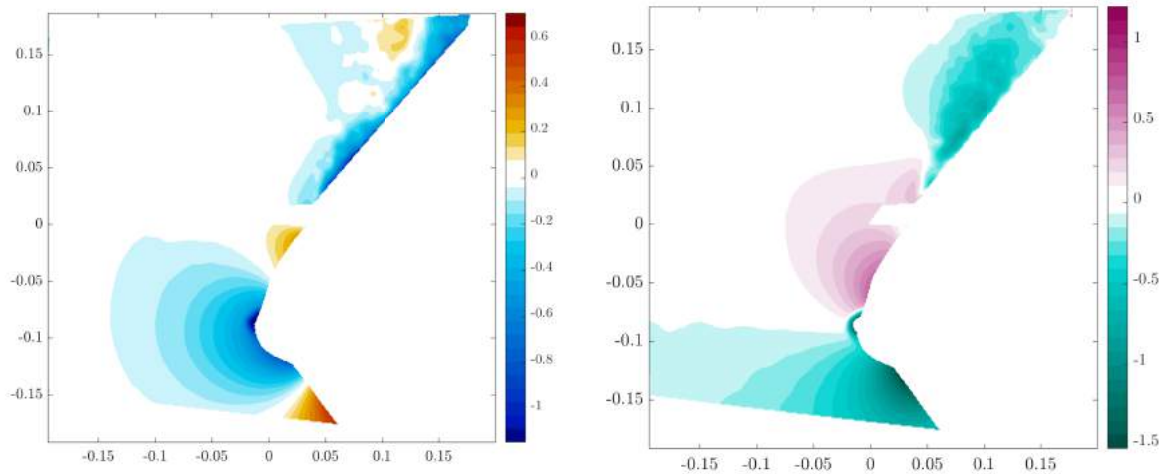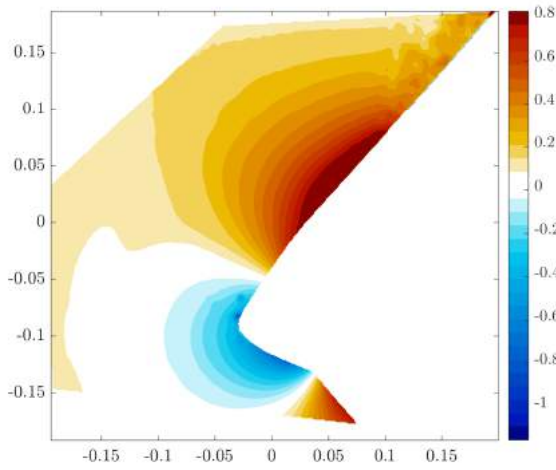

(a) Velocity field V_x as a function of V_D pressure side   **(b)** Velocity field V_y/V_D pressure side
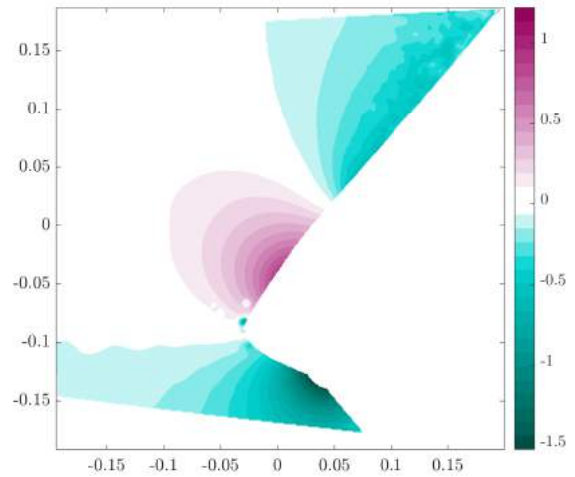
Figure 9.10: Velocity fields for V_x & V_y at $r/R = 0.36$ with flap

6.3. Either too much fog was injected or not enough time was given for the fog to evenly mix into the flow resulting in the discrepancies that can be seen in figures 9.7a, 9.7b, 9.8a and 9.8b.
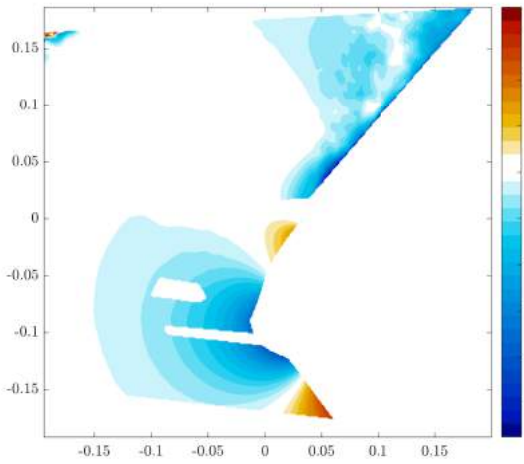
The flow was injected with fog from time to time at other measurement points as well but unfortunately a record of this was not kept. This was also difficult as there was no way to trace the amount of fog that was being injected into the flow.
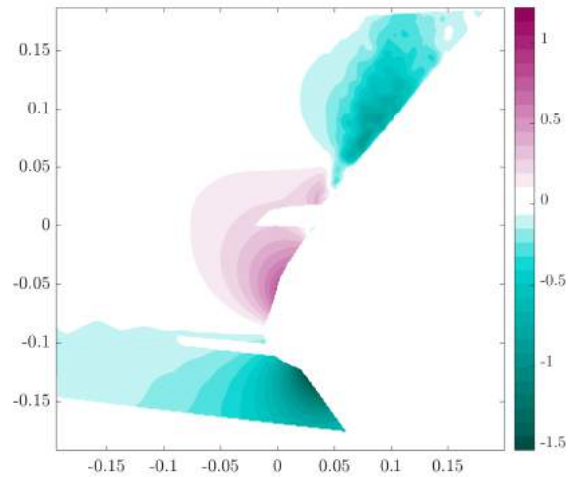
(a) Velocity field V_x as a function of V_D pressure side no flap

(b) Velocity field V_y/V_D pressure side no flap

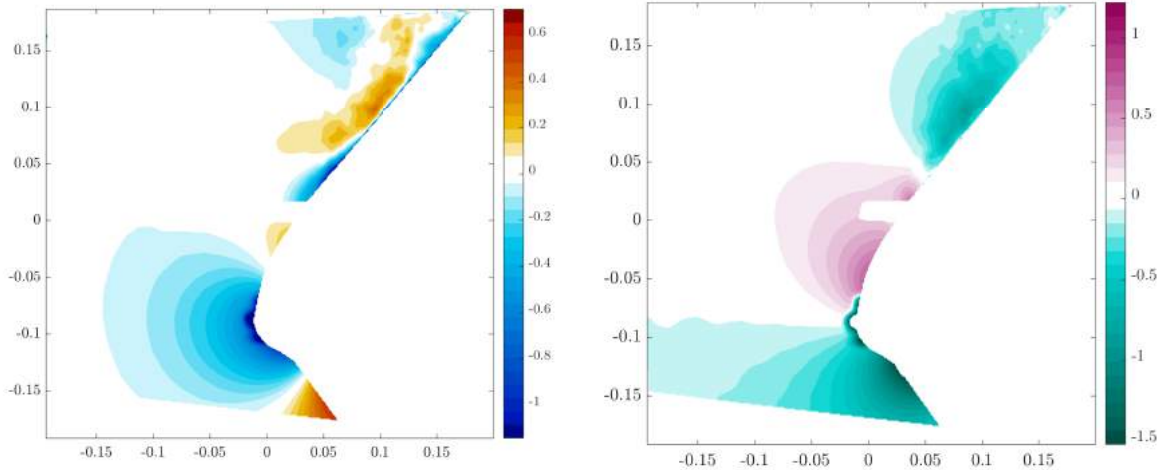**(c)** Velocity field V_x as a function of V_D pressure side with flap

(d) Velocity field V_y/V_D pressure side with flap

Figure 9.11: Velocity fields for V_x & V_y at $r/R = 0.34$ with and without flap

## 9.6   Comparing the Planar PIV with Stereoscopic PIV results

9.6.1   Issues with the Stereoscopic Case

Reduced area: The Stereoscopic PIV analysis requires data from both cameras. Due to the angle of the camera certain areas of field of view are only captured by one camera and not the other. This means that this single data would not be used. This is clearly apparent from figure 7.6. Where it can be seen from figure 7.6b that the lower left corner of the calibration plate is not in view of the second camera and therefore the resulting corrected image for stereoscopic PIV in figure 7.6d is also missing that corner.

(a) Velocity field V_x as a function of V_D pressure side

(b) Velocity field V_y/V_D pressure side

Figure 9.12: Velocity fields for V_x & V_y at $r/R = 0.33$ with flap
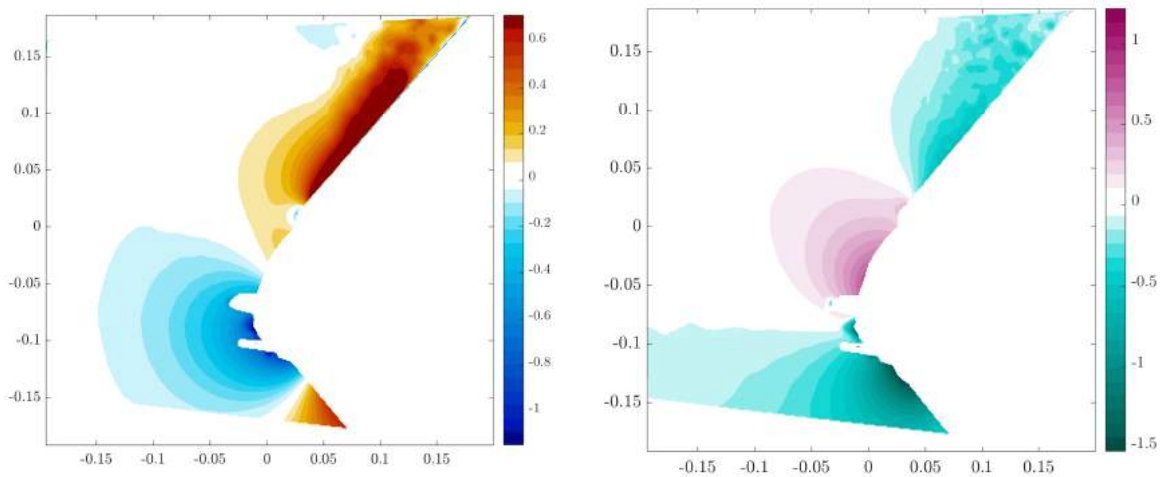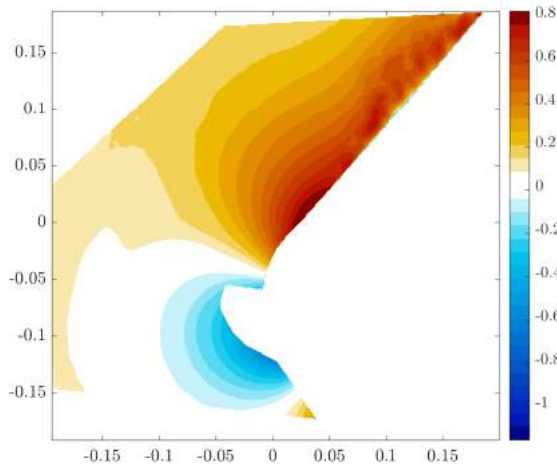

(a) Velocity field V_x as a function of V_D pressure side
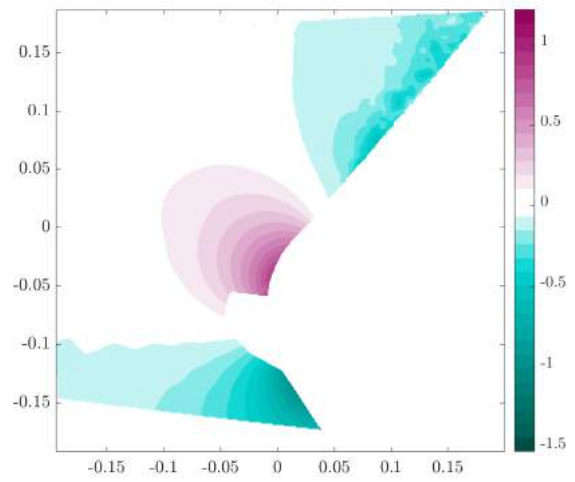
(b) Velocity field V_y/V_D pressure side

Figure 9.13: Velocity fields for V_x & V_y at $r/R = 0.31$ with flap

Twice the reflection/defects: As specified in the previous paragraph overlap is a necessary prerequisite for Stereoscopic PIV analysis and this phenomenon unfortunately also is valid for defects and reflections in the images. This can be observed in figure 9.25, where figures 9.25a and 9.25b show the processed captured images from the camera 1 and 2 respectively, with the crop that was applied highlighted by red lines. It can clearly be seen from image 9.25c that much more area is lost in comparison to the planar case in figure 9.25d.
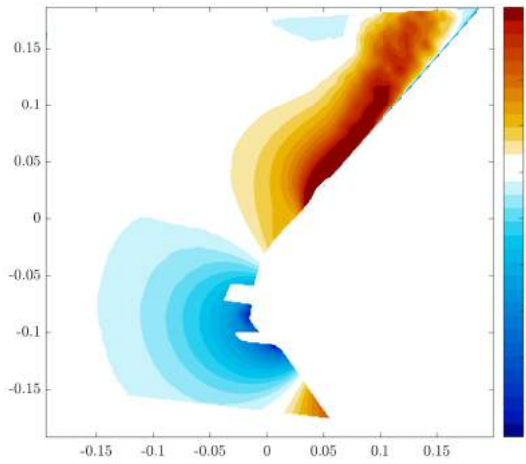
Difference in Exposure: Another factor that effects the stereoscopic PIV results is the difference in exposure of the images. As data from both images is used and the differences in
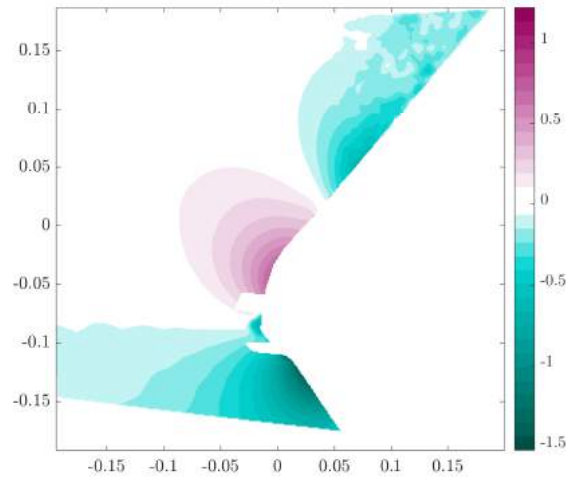
(a) Velocity field V_x as a function of V_D pressure side no flap

(b) Velocity field V_y/V_D pressure side no flap

(c) Velocity field V_x as a function of V_D pressure side with flap

(d) Velocity field V_y/V_D pressure side with flap

Figure 9.14: Velocity fields for V_x & V_y at $r/R = 0.30$ with and without flap

the exposure of the images results in more noise in the result which is discernible from figure 9.25. Where the difference in exposure especially on the edges of figure 9.25a and 9.25b can be clearly seen.

(a) Velocity field $V_x(V_D)$ no flap

(b) Velocity field V_y/V_D pressure side no flap

(c) Velocity field $V_x(V_D)$ with flap
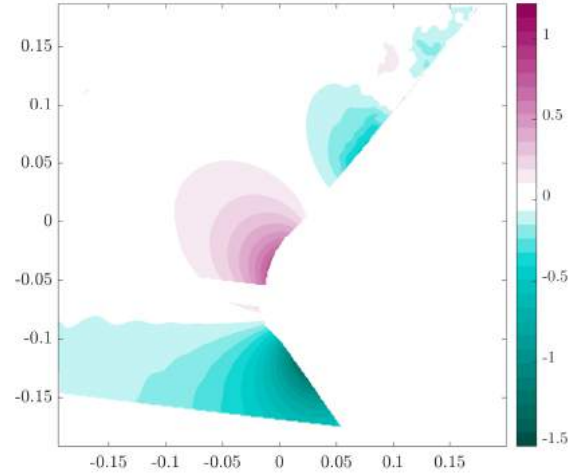
(d) Velocity field V_y/V_D pressure side with flap
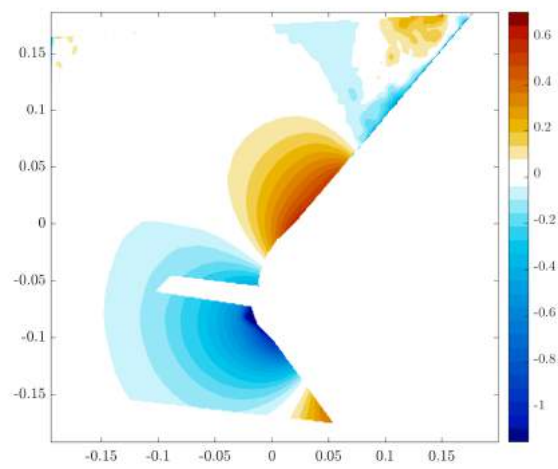
(e) Velocity field $V_x(V_D)$ with flap - **Painted**
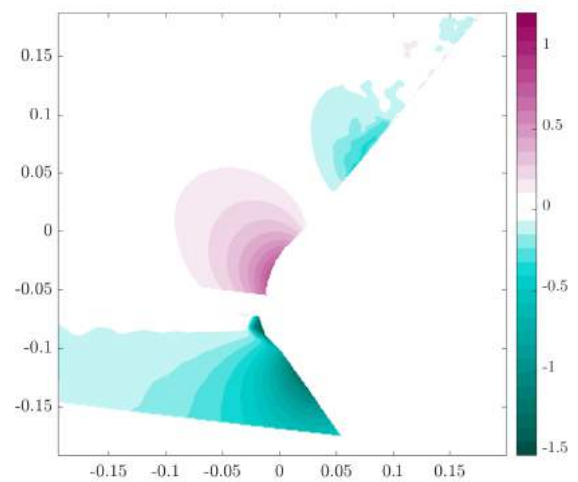
(f) Velocity field V_y/V_D pressure side with flap - **Painted**

Figure 9.15: Velocity fields for V_x & V_y at $r/R = 0.26$ with and without flap, plus flap and the tripping-wires spray painted. **95**

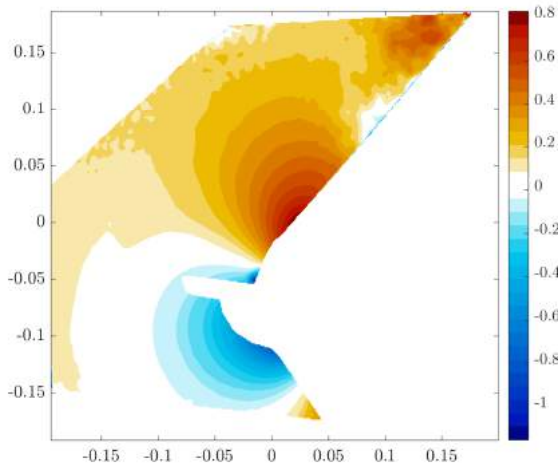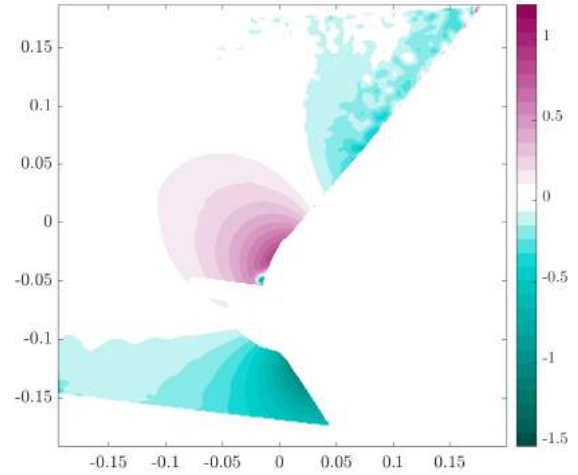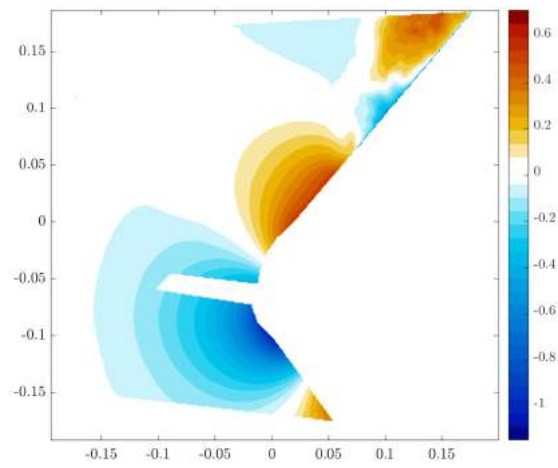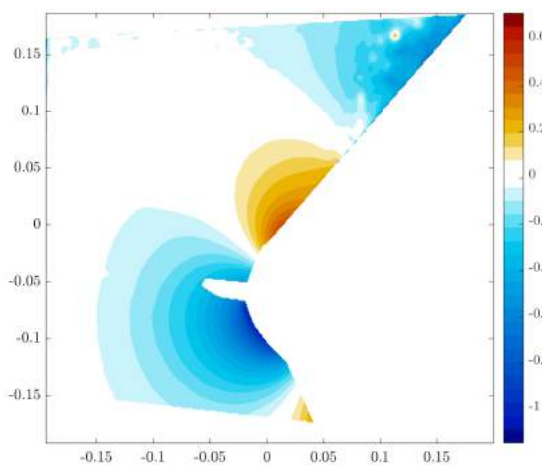**(a)** Velocity field V_x as a function of V_D pressure side
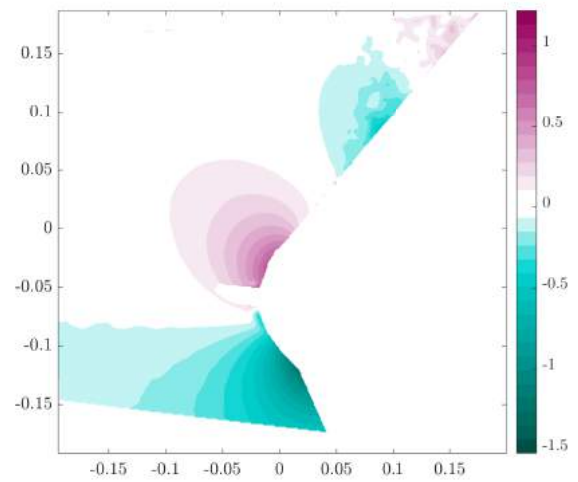
(b) Velocity field V_y/V_D pressure side

Figure 9.16: Velocity fields for V_x & V_y at $r/R = 0.22$
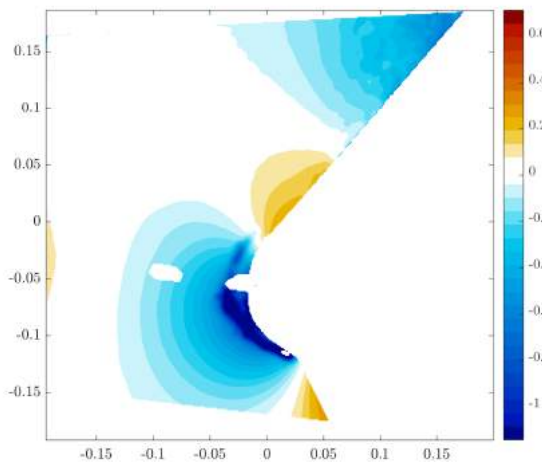
(a) Velocity field V_x as a function of V_D pressure side
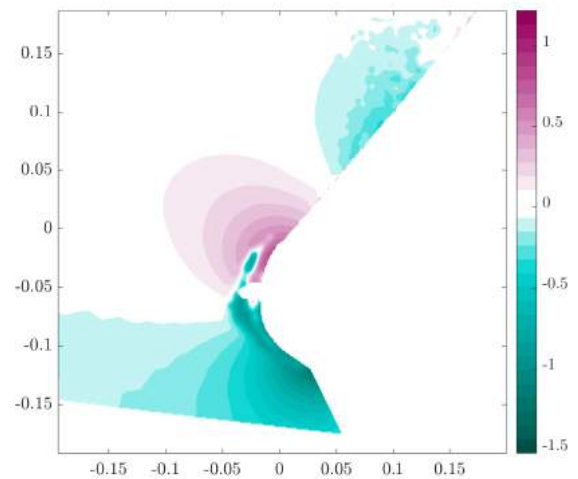
(b) Velocity field V_y/V_D pressure side

Figure 9.17: Velocity fields for V_x & V_y at $r/R = 0.17$
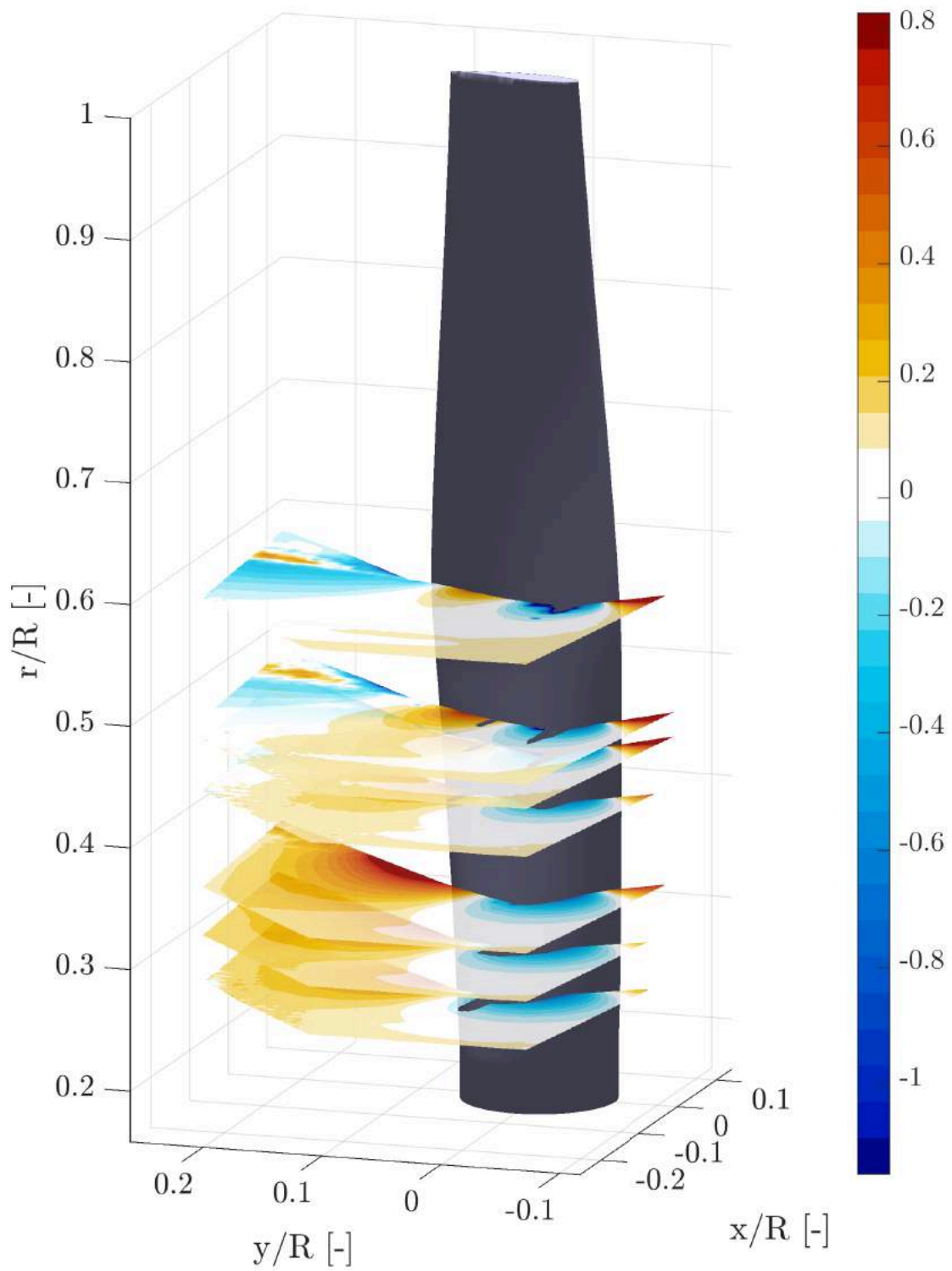
Figure 9.18: Velocity Field V_x as function of V_D pressure-side of blade at multiple r/R locations for no-flap configuration.
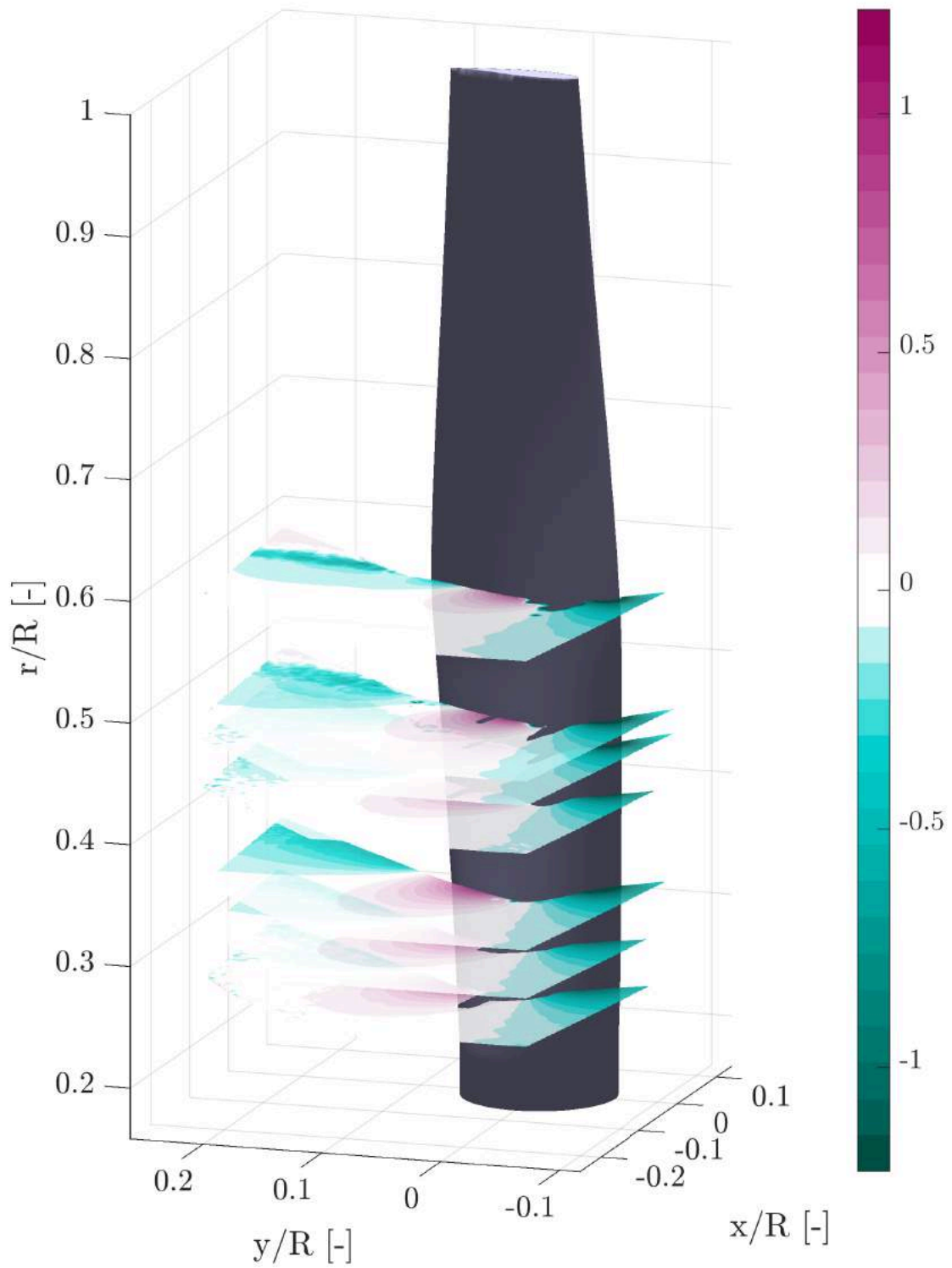
Figure 9.19: Velocity Field V_y/V_D pressure-side of blade at multiple r/R locations for no-flap configuration.
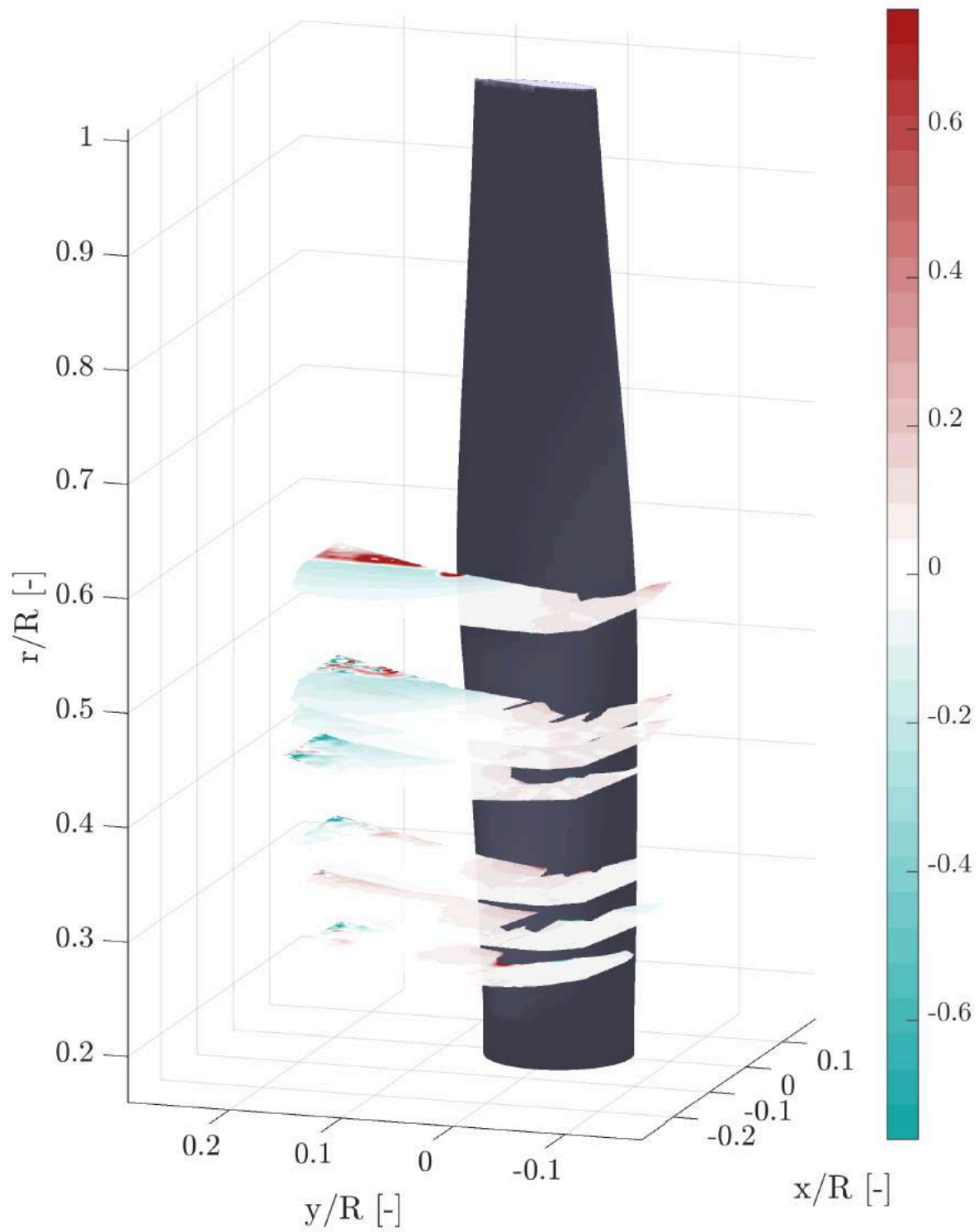
Figure 9.20: Velocity Field V_z/V_D pressure-side of blade at multiple r/R locations for no-flap configuration.
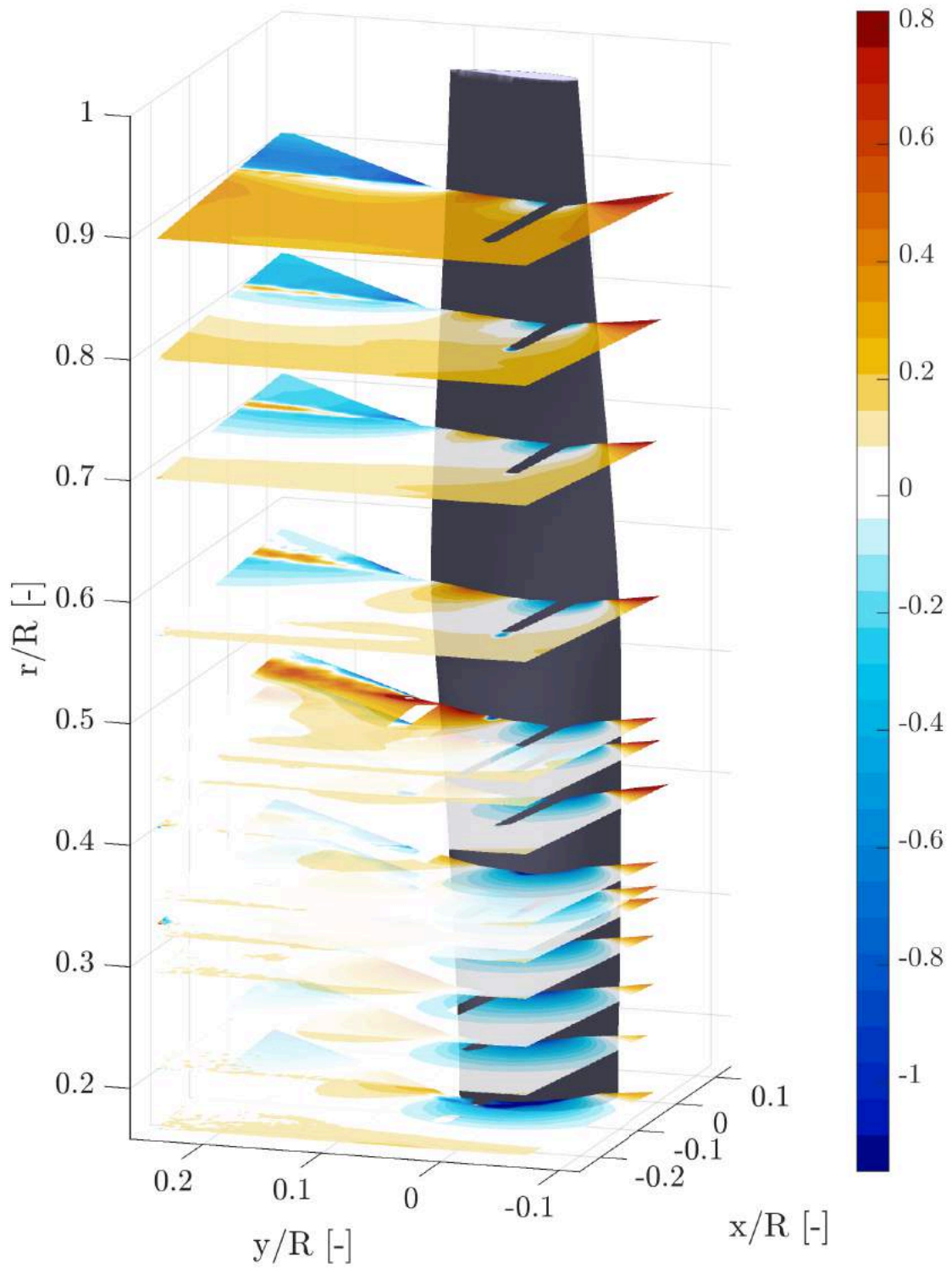
Figure 9.21: Velocity Field V_x as function of V_D pressure-side of blade at multiple r/R locations - flapped configuration
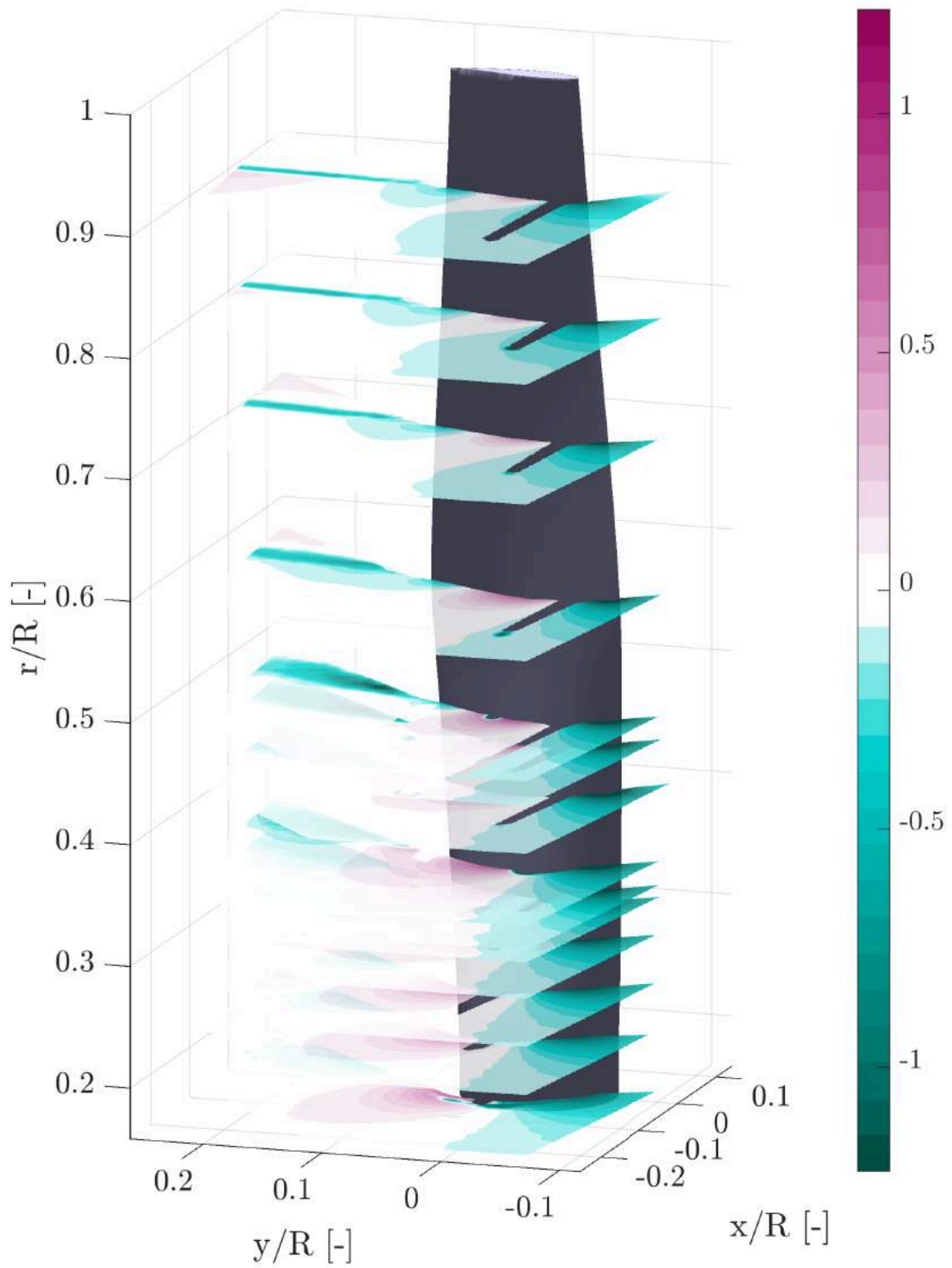
Figure 9.22: Velocity Field V_y/V_D pressure-side of blade at multiple locations - flapped configuration
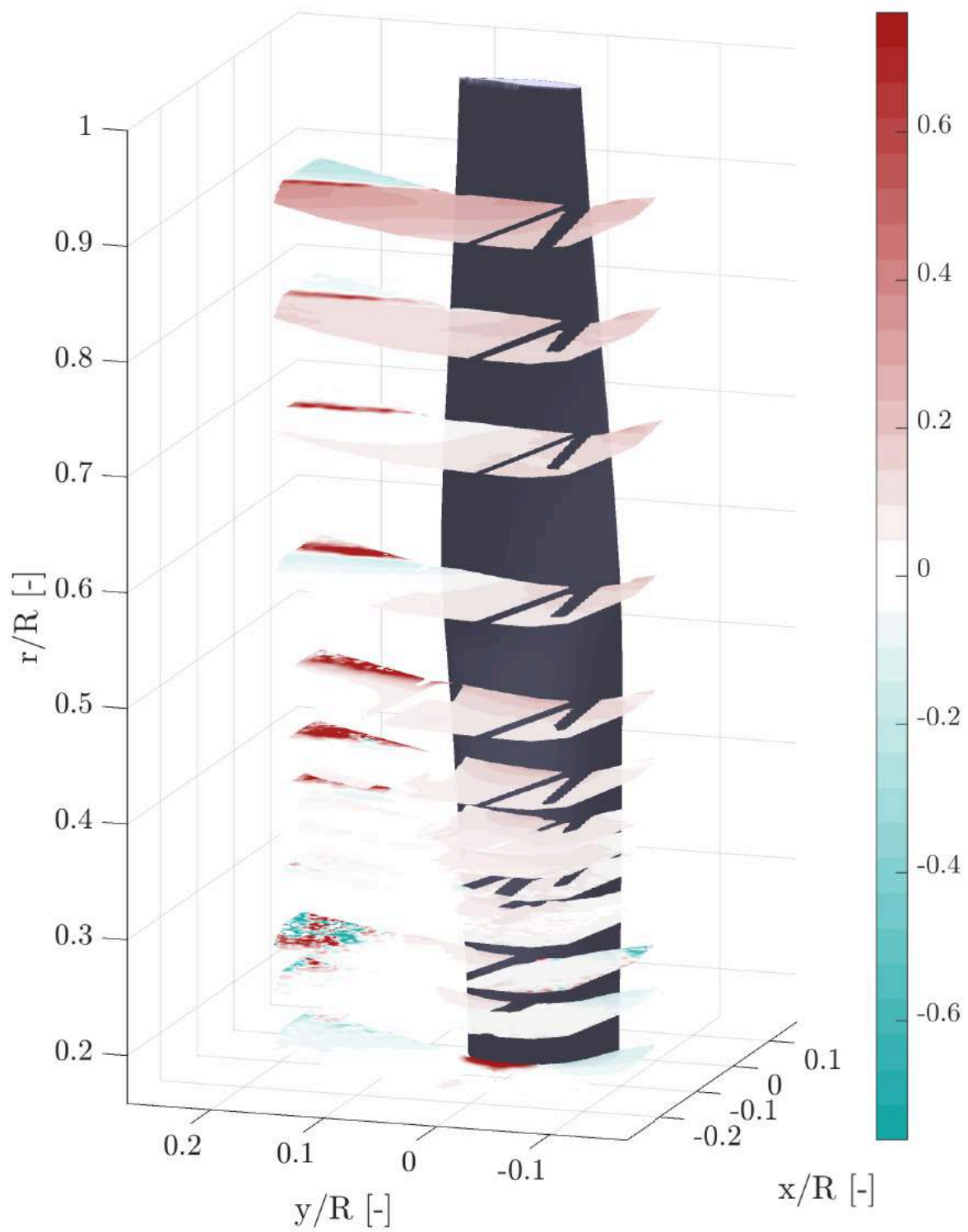
Figure 9.23: Velocity Field V_z/V_D obtained from stereoscopic PIV for the pressure-side of blade at multiple locations - flapped configuration

(a) $0.9\ r/R$ planar PIV

(b) $0.57\ r/R$ planar PIV

(c) $0.17\ r/R$ planar PIV

(d) $0.9\ r/R$ stereo PIV

(e) $0.57\ r/R$ stereo PIV

(f) $0.17\ r/R$ stereo PIV
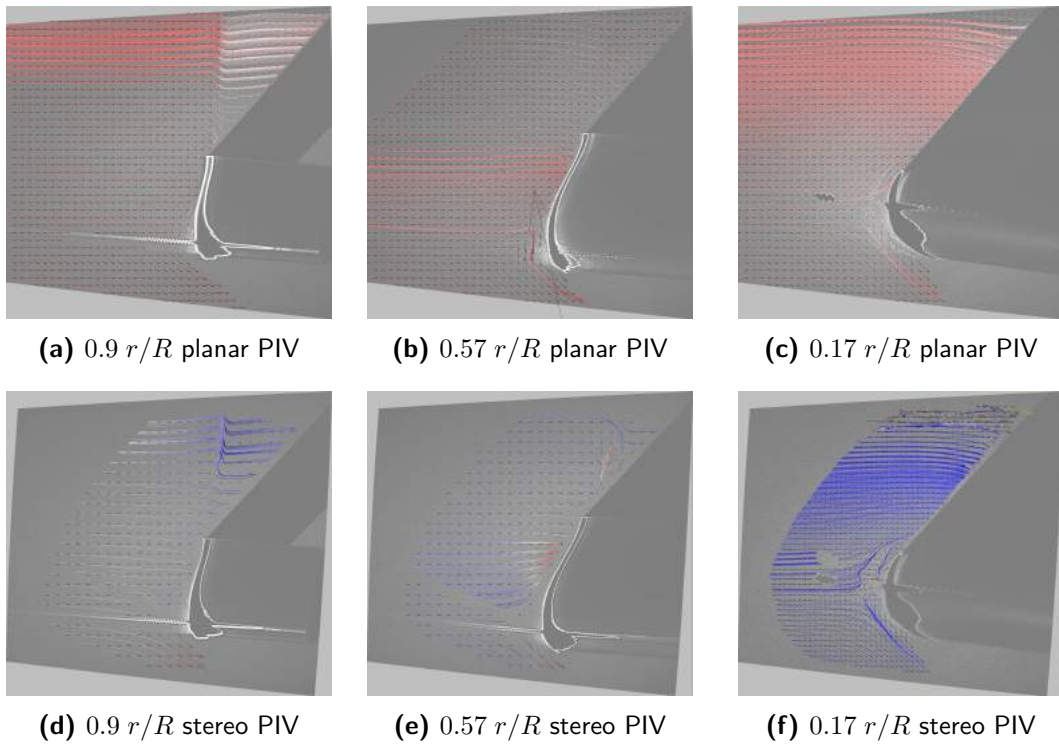
Figure 9.24: Stagnation Point determination based on the streamlines analysis of the planar and stereo PIV results
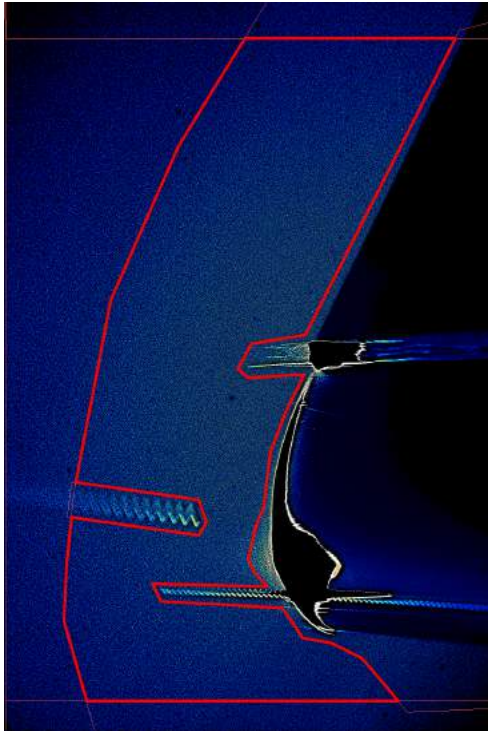
(a) Geometric mask camera 1
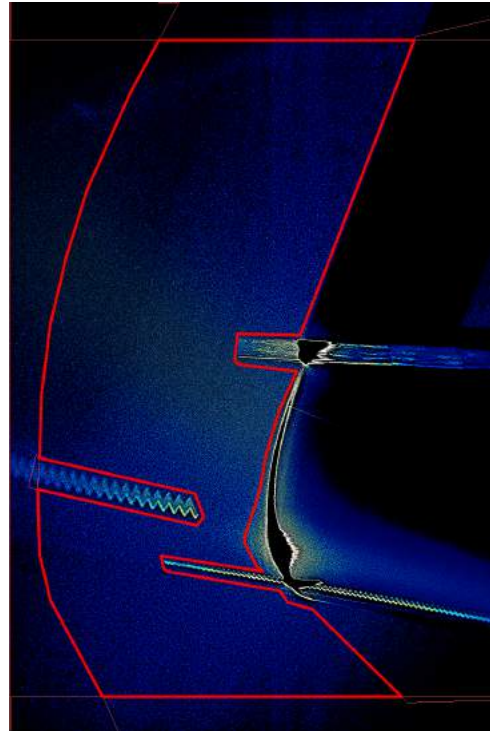
(b) Geometric mask camera 2
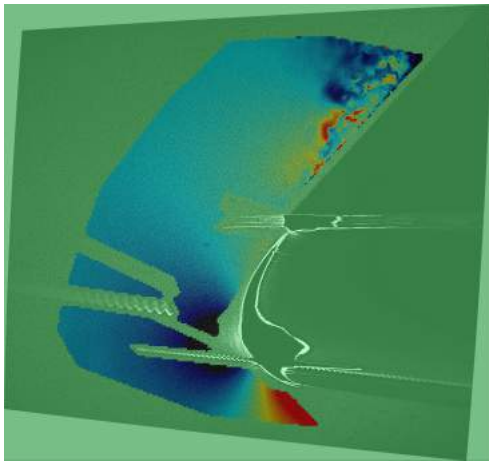
(c) Velocity field V_{avg} Stereoscopic PIV
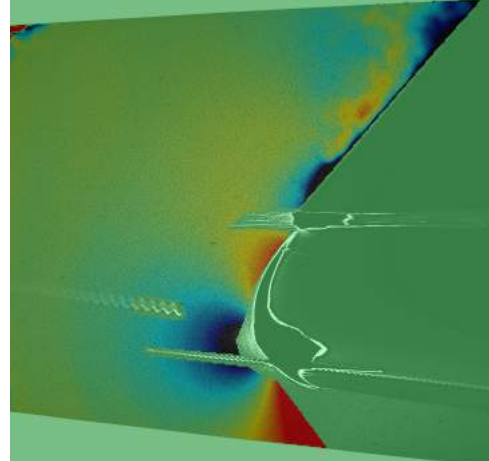
(d) Velocity field V_{avg} Planar PIV

Figure 9.25: Screen capture of the geometric masks applied to the images captured at $r/R = 0.34$ and the resulting stereoscopic and planar velocity fields.

Part IV

Conclusion

Chapter 10

Conclusions & recommendations

This masters thesis investigated the augmentation of flaps to the suction-side of a model HAWT. The study consisted of understanding the effects of different chord-wise locations and shape on the performance enhancement of the wind turbine blades. As a first step load measurements were carried-out and results calculated and compared. Also, the effects of adding zigzag tape and blade pitching angle were studied during the load measurements. To further understand how the flaps effect the performance of the blade a SPIV investigation was carried out on one selected flap configuration and compared with no-flap configuration to get insights from the flow visualizations. Additionally, a manual calibration, i.e. image correction technique was developed and compared to the automated calibration done by the LaVision DaVis software.

10.1   Conclusions

From the load measurements and SPIV analyses the following conclusions can be drawn:

   i. The augmentation of the flaps to the pressure side increase the C_P and C_T values for almost all configurations when comparing with no-flap configuration. Only for certain configurations and for $3 \gtrsim \lambda_{tip} \lesssim 6.5$ do the values slightly go below the no-flap configuration. This is particularly the case for taller flap $\angle$.

  ii. Moving the flaps closer to the trailing edge generally increases the C_P at the cost of slight decrease in C_T except for flap $\triangle$ which overcomes the decrease in C_T.

 iii. The height of the flap seem to play a less significant role as the flap moves closer to the trailing edge as the plots of the different configurations start to coverage.

 iv. Flap $\triangle$ seems to offer the best overall performance improvement located at 95% chord. The values from other flaps also have similar values but generally higher C_T values and higher values of C_P for $\lambda_{tip} > 6$

  v. The stagnation points along the blade of the model for $\lambda_{tip} = 4.63$ (351 rpm) seem to occur around the location of the zigzag tape.

vi. The V_x velocity fields show a higher low-speed area on the pressure-side of the flapped configuration in comparison to the no-flap configuration, i.e. higher pressure.

vii. The flaps seems to generate a higher intensity vortex, whose intensity is even higher on the outboard edge of the flap at $r/R = 0.3$ due to the higher rotational velocity at the aforementioned span-wise location.

viii. The aerodynamic flow for the flapped configuration seems to have higher movement in the span-wise direction. Having a more slightly prominent out-board flow when comparing V_z velocity fields.

ix. Calibration used by the LaVision DaVis software is more complex than initially expected and seems to work more locally then just simply stretching the image. However, the 3rd order polynomial function for calibration generated by DaVis contains some error and does not give correct results.

10.2 Recommendations and future work

The following recommendation can be made to built upon this research and to improve the quality of similar experiments in the future.

i. Due to time constrains and technical issues, the SPIV analyses was only carried out for the pressure-side of the blade and therefore to get a complete picture of the flow around the blade a SPIV analyses on the suction side of the same blade with the same configuration is recommended to complete the analysis.

ii. To place the zigzag tapes more precisely and have them function more effectively a Surface Oil Flow Visualization is advised during the initial phases of the experiment.

iii. The unwanted reflections from the different elements of the set-up degrade the image quality of the PIV data and a simple trick to use orange highlighter marker could absorb the light of the green wavelength, which was the color and the wavelength of the laser used for the PIV analyses.

iv. Another significant aspect the effects the quality of the PIV data is the consistency of the tracer particles in the flow. There is at the moment no way of uniformly seeding these particles into the flow and is done just at random and with interventions based on the visual quality of data being gathered. A way to measure and uniformly and automatically seed the correct amount of tracer particles could really help with the quality of the data.

References/Bibliography

[1] R. H. Liebeck, "Design of subsonic airfoils for high lift," *Journal of Aircraft*, vol. 15, no. 9, pp. 547 – 561, 9 September 1978. (pages v, 10, 10, 11)

[2] B. Akay, D. Ragni, C. J. Simão Ferreira, and G. J. W. van Bussel, "Experimental investigation of the root flow in a horizontal axis wind turbine," *Wind Energy*, vol. 17, no. 7, pp. 1093–1109, 2014. (pages v, 4, 28)

[3] H. Dumitrescu and V. Cardos, "Rotational effects on the boundary-layer flow in wind turbines," *American Institute of Aeronautics and Astronautics (AIAA) Journal*, vol. 42, no. 2, pp. 408 – 411, February 2004. (pages v, 4)

[4] N. Bao, H. Ma, and Z. Ye, "Experimental study of wind turbine blade power augmentation using airfoil flaps, including the gurney flap," *Wind Engineering*, vol. 24, no. 1, pp. 25–34, 2000. (pages 11, 11, 12, 12)

[5] M. A. Woodgate, V. A. Pastrikakis, and G. N. Barakos, "Method for calculating rotors with active gurney flaps," *Journal of Aircraft*, vol. 53, no. 3, pp. 605 – 626, February 2016. (pages 11, 12)

[6] S. Jain, N. Sitaram, and S. Krishnaswamy, "Effect of reynolds number on aerodynamics of airfoil with gurney flap," *International Journal of Rotating Machinery*, vol. 2015, 2015. (pages 14, 15)

[7] B. McKeon, G. Comte-Bellot, J. Foss, J. Westerweel, F. Scarano, C. Tropea, J. Meyers, J. Lee, A. Cavone, R. Schodl, M. Koochesfahani, Y. Andreopoulos, W. Dahm, J. Mullin, J. Wallace, P. Vukoslavčević, S. Morris, E. Pardyjak, and A. Cuerva, "Velocity, vorticity, and mach number," in *Springer Handbook of Experimental Fluid Mechanics*, C. Tropea, A. L. Yarin, and J. F. Foss, Eds. Springer Berlin Heidelberg, 2007, no. 5, pp. 215–471. (pages xiii, 19, 19, 20, 21, 21)

[8] D. S. Tony Burton, Nick Jenkins and E. Bossanyi, *Wind Energy Handbook.* John Wiley & Sons, Ltd, 2011, ISBN: 978-1-119-99271-4. (pages xv, 83)

[9] "Adwen and LM wind power partner to present the longest blade in the world," 21 Jun 2016. [Online]. Available: www.adwenoffshore.com/

adwen-and-lm-wind-power-partner-to-present-the-longest-blade-in-the-world-2/ (pages 3, 7)

[10] J. L. Sawin, "Renewables 2017 global status report," Renewable Energy Policy Network for the 21st Century, Paris, ISBN 978-3-9818107-6-9, 2017. (page 3)

[11] D. Hu, O. Hua, and Z. Du, "A study on stall-delay for horizontal axis wind turbine," *Renewable Energy*, vol. 31, no. 6, pp. 821 – 836, May 2006. (page 4)

[12] E. Hau and H. von Renouard, *Wind Turbines: Fundamentals, Technologies, Application, Economics.* Springer Berlin Heidelberg, 2005. (page 4, 4)

[13] R. McKenna, P. O. v.d. Leye, and W. Fichtner, "Key challenges and prospects for large wind turbines," *Renewable and Sustainable Energy Reviews*, vol. 53, pp. 1212 – 1221, 2016. (page 7)

[14] I. Aramendia, U. Fernandez-Gamiz, J. A. Ramos-Hernanz, J. Sancho, J. M. Lopez-Guede, and E. Zulueta, *Energy Harvesting and Energy Efficiency: Technology, Methods, and Applications.* Springer, 2017, no. 21, ch. Flow Control Devices for Wind Turbines, pp. 629–655. (pages 7, 9, 9)

[15] J. A. Franco, J. C. Jauregui, and M. Toledano-Ayala, "Optimizing wind turbine efficiency by deformable structures in smart blades," *Journal of Energy Resources Technology*, vol. 137, no. 17, 17 December 2015. (pages 7, 8, 9)

[16] K. Lenz and P. Fuglsang, "Wind turbine blade having a spoiler with effective separation of airflow," European Patent Application EP 2 141 358 A1, 12 December, 2008. (page 8, 8, 8)

[17] P. Quell and M. Petsche, "Rotor blade for a wind power station," U.S. Patent US 7 585 157 B2, 8 September, 2009. (pages 8, 10)

[18] H. D. Taylor, "The elimination of diffuser separation by vortex generators," United Aircraft Corporation, Report no. R-4012-3, June 1947. (page 7)

[19] G. Godard and M. Stanislas, "Control of a decelerating boundary layer. part 1: Optimization of passive vortex generators," *Aerospace Science and Technology*, vol. 10, no. 3, pp. 181 – 191, 2006. (page 8)

[20] B. L. Storms and C. S. Jang, "Lift enhancement of a airfoil using a gurney and vortex generators," in *31st Aerospace Sciences Meeting*, Reno, NV, U.S.A., Jan. 11–14 1993, paper AIAA-93-0647. (pages 8, 15, 15, 16)

[21] S. Oerlemans, J. Schepers, G. Guidati, and S. Wagner, "Experimental demonstration of wind turbine noise reduction through optimized airfoil noise reduction through optimized airfoil shape and trailing-edge serrations," Nationaal Lucht en Ruimtevaartlaboratorium, Report no. NLR-TP-2001-324, 10 July 2001. (page 9)

[22] I. Herráez, B. Stoevesandt, and J. Peinke, "Insight into rotational effects on a wind turbine blade using navierstokes computations," *Energies*, vol. 7, no. 10, pp. 6798–6822, 2014. (pages 10, 17)

[23] J. A. Cole, B. A. O. Vieira, J. G. Coder, A. Premi, and M. D. Maughmer, "Experimental investigation into the effect of gurney flaps on various airfoils," *Journal of Aircraft*, vol. 50, no. 4, pp. 1287–1294, July 2013. (page 10)

[24] D. R. Troolin, E. K. Longmire, and W. T. Lai, "The effect of gurney flap height on vortex shedding modes behind symmetric airfoils," in *13th Int Symposium on Applications of Laser Techniques to Fluid Mechanics*, Lisbon, Portugal, Jun. 26–29 2006. (page 10)

[25] C. S. Jang, J. C. Ross, and R. M. Cummings, "Numerical investigation of an airfoil with a Gurney flap," *Aircraft Design*, vol. 1, no. 2, pp. 75 – 88, June 1998. (pages 10, 11)

[26] P. Giguère, J. Lemay, and G. Dumas, "Gurney flap effects and scaling for low-speed airfoils," in *13th Applied Aerodynamics Conference*, San Diego, CA, U.S.A., Jun. 19–22 1995, paper AIAA-95-1881-CP. (page 10)

[27] J. Wang, Y. Li, and K.-S. Choi, "Gurney flaplift enhancement, mechanisms and applications," *Progress in Aerospace Sciences*, vol. 44, no. 1, pp. 22 – 47, 2008. (pages 10, 11, 11, 11, 12, 13)

[28] A. B. Bach, "Gurney flaps and micro-tabs for load control on wind turbines," Ph.D. dissertation, Technische Universität Berlin, 9 Feb 2016. (pages 10, 11, 13, 13)

[29] M. D. Maughmer and G. Bramesfeld, "Experimental investigation of gurney flaps," *Journal of Aircraft*, vol. 45, no. 6, pp. 2062 – 2067, Nov 2008. (pages 10, 13)

[30] L. Brown and A. Filippone, "Aerofoil at low speeds with gurney flaps," *The Aeronautical Journal (1968)*, vol. 107, no. 1075, pp. 539 – 546, 2003. (page 11)

[31] M. A. Woodgate, V. A. Pastrikakis, and G. N. Barakos, *Advances in Fluid-Structure Interaction*. Springer International Publishing, 2016, ch. Rotor Computations with Active Gurney Flaps, pp. 133–166. (pages 11, 13, 13)

[32] R. Chow and C. van Dam, "Computational investigations of deploying load control microtabs on a wind turbine airfoil," in *45th AIAA Aerospace Sciences Meeting and Exhibit*, Reno, Nevada, USA, Jan. 8–11, 2007. (page 13)

[33] S. J. Johnson, J. P. Baker, C. P. van Dam, and D. Berg, "An overview of active load control techniques for wind turbines with an emphasis on microtabs," *Wind Energy*, vol. 13, no. 2-3, pp. 239–253, 2010. (page 13)

[34] C. P. van Dam, D. T. Yen, and P. M. H. W. Vijgen, "Gurney flap experiments on airfoil and wings," *Journal of Aircraft*, vol. 36, no. 2, pp. 484–486, 1999. (page 14)

[35] E. Mayda, C. van Dam, and D. Nakafuji, "Computational investigation of finite width microtabs for aerodynamic load control," in *43rd AIAA Aerospace Sciences Meeting and Exhibit*, Reno, Nevada, USA, Jan. 10–13, 2005. (page 14)

[36] A. D. Mohammad Mohammadi and M. Doosttalab, "The effect of various gurney flap shapes on the performance of wind turbine airfoils," in *ASME Early Career Technical Conference*, Atlanta, GA, U.S.A., Nov. 2–3 2012. (pages 15, 16)

[37] M. Raffel, C. E. Willert, S. T. Wereley, and J. Kompenhans, *Particle Image Velocimetry*, ser. Experimental Fluid Mechanics. Berlin, Heidelberg: Springer Berlin Heidelberg, 2007. (pages 17, 18, 18)

[38] F. Scarano, "Experimental aerodynamics," Delft University of Technology, Course Reader AE4180, February 2013. (pages 17, 18, 19, 20)

[39] M. H. Farias, R. S. Teixeira, J. Koiller, and A. M. Santos, "Brief review of uncertainty quantification for particle image velocimetry," *Journal of Physics: Conference Series*, vol. 733, no. 1, 2016. (page 18)

[40] R. J. Adrian and J. Weterweel, *Particle Image Velocimetry*, ser. Cambridge Aerospace Series. Cambridge University Press, 2011, ISBN: 978-0-521-44008-0. (pages 18, 21, 53, 60, 119)

[41] E. J. Stamhuis, "Basics and principles of particle image velocimetry (PIV) for mapping biogenic and biologically relevant flows," *Aquatic Ecology*, vol. 40, no. 4, pp. 463–479, 2006. (page 19)

[42] A. K. Prasad and R. J. Adrian, "Stereoscopic particle image velocimetry applied to liquid flows," *Experiments in Fluids*, vol. 15, no. 1, pp. 49–60, 1993. (pages 19, 20, 20, 20)

[43] A. P. K. Sekar, "Investigation of root spoiler on horizontal axis wind turbines," MSc Thesis, Delft University of Technology, 24 Feb 2016. (page 19)

[44] R. J. Adrian, "Twenty years of particle image velocimetry," *Experiments in Fluids*, vol. 39, no. 2, pp. 159–169, 2005. (page 19)

[45] A. K. Prasad and K. Jensen, "Scheimpflug stereocamera for particle image velocimetry in liquid flows," *Applied Optics*, vol. 34, no. 30, pp. 7092–7099, Oct 1995. (page 20)

[46] H. Hu, *Handbook of 3D Machine Vision: Optical Metrology and Imaging*. Taylor & Francis, Inc., 2013, no. 4, ch. Stereo Particle Imaging Velocimetry Techniques: Technical Basis, System Setup, and Application. (pages 21, 22, 22, 23)

[47] K. Imaichi and K. Ohmi, "Numerical processing of flow-visualization pictures measurement of two-dimensional vortex flow," *Journal of Fluid Mechanics*, vol. 129, p. 283311, 1983. (page 22)

[48] F. Noca, D. Shiels, and D. Jeon, "A comparison of methods for evaluating time-dependent fluid dynamic forces on bodies, using only velocity fields and their derivatives," *Journal of Fluids and Structures*, vol. 13, no. 5, pp. 551 – 578, 1999. (page 23, 23)

[49] V. del Campo, D. Ragni, D. Micallef, F. J. Diez, and C. F. Simão Ferreira, "3D load estimation on a horizontal axis wind turbine using SPIV," *Wind Energy*, vol. 17, no. 11, pp. 1645–1657, 11 August 2013. (pages 23, 24)

Appendix A
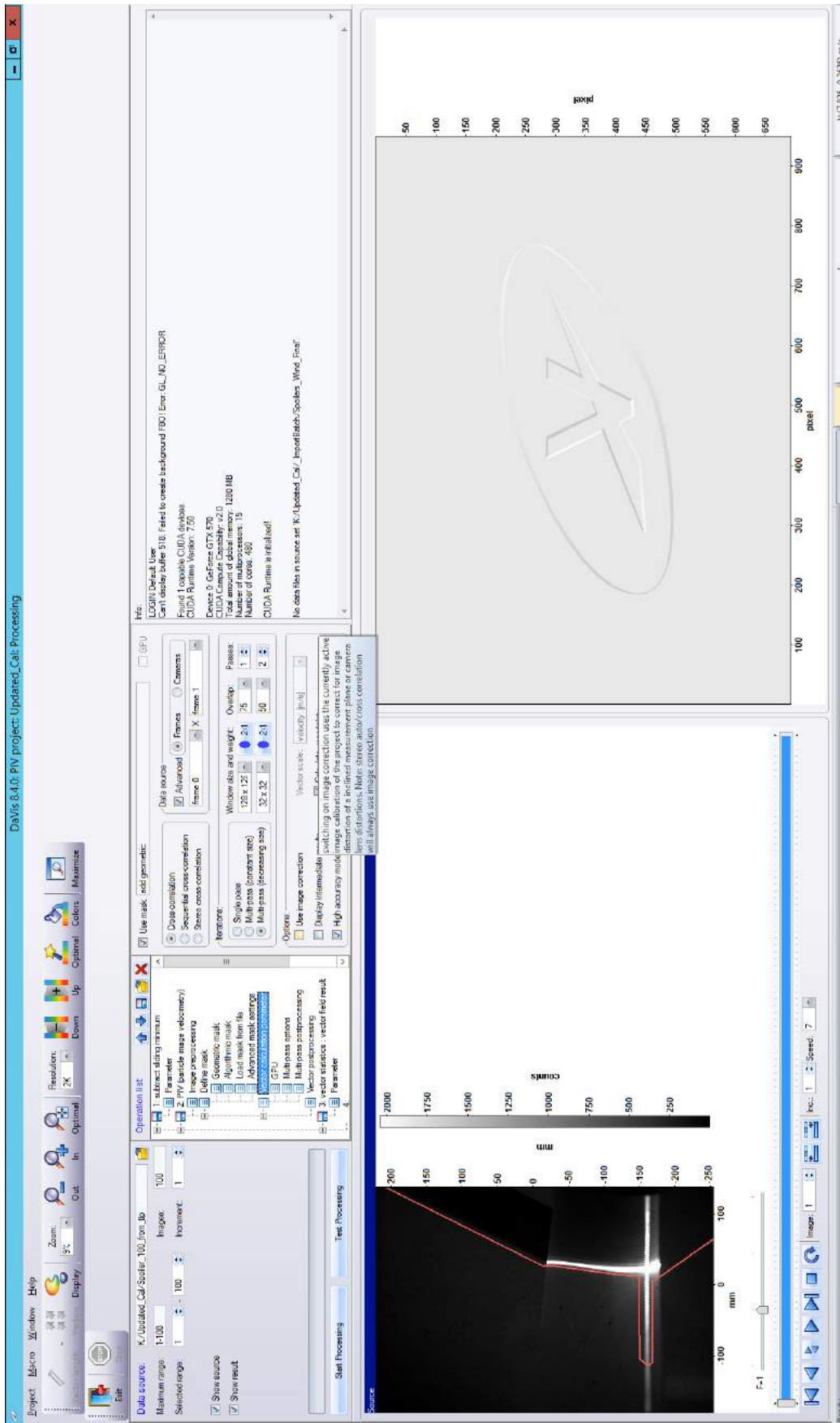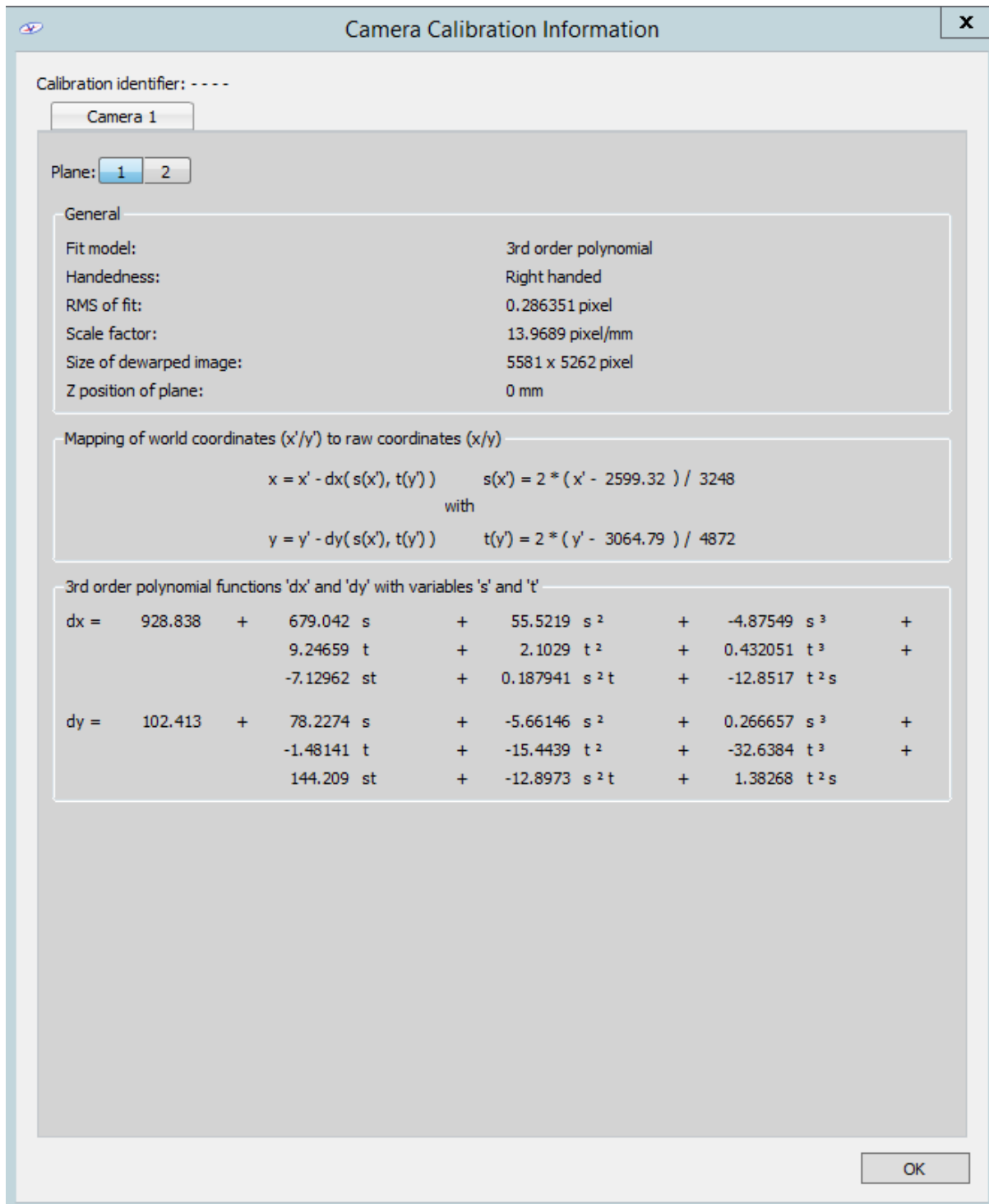
Additional visuals

Figure A.1: LaVision DaVis 8.4.0 processing window.

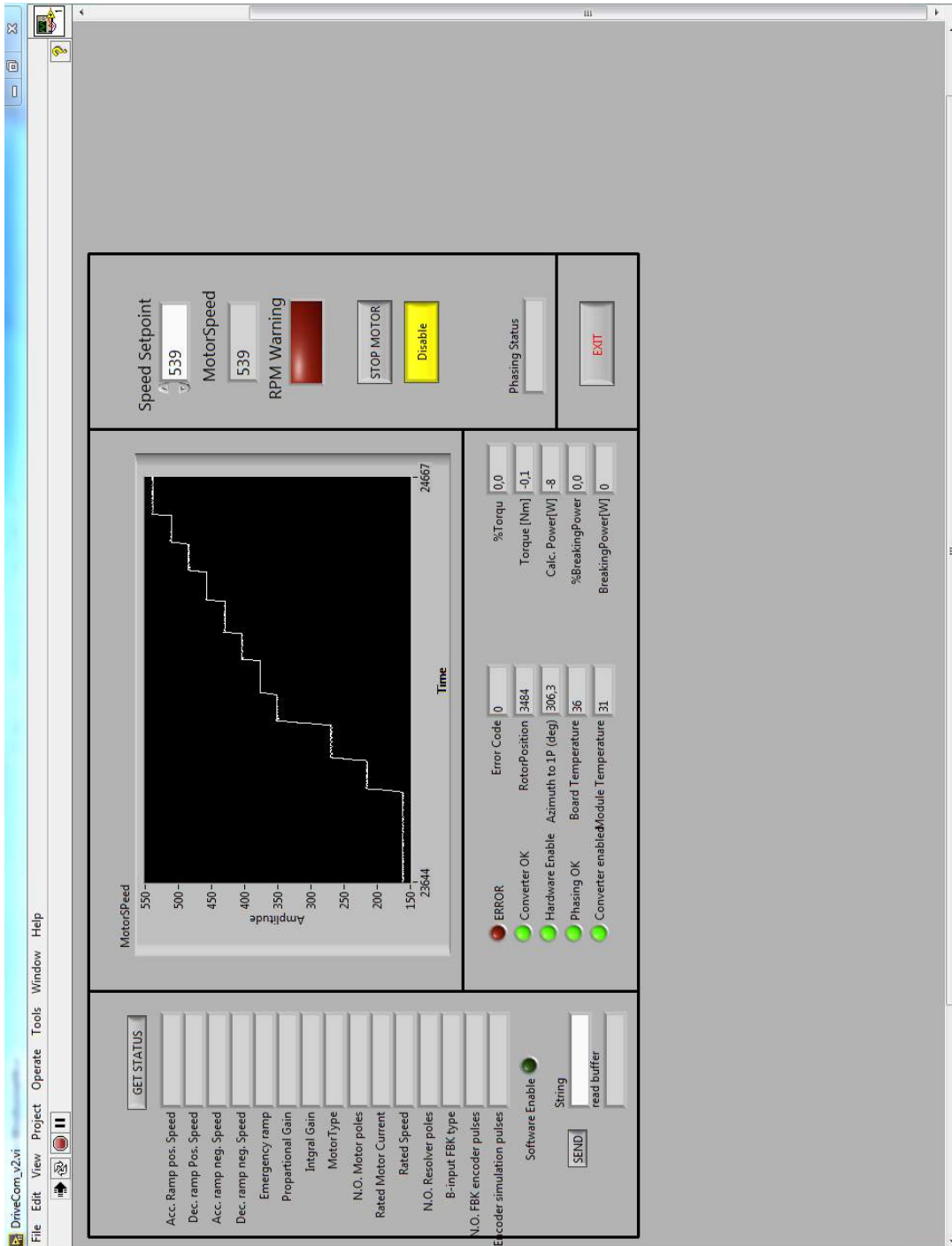**Figure A.2:** Camera Calibration Information window - LaVision DaVis 8.4.0

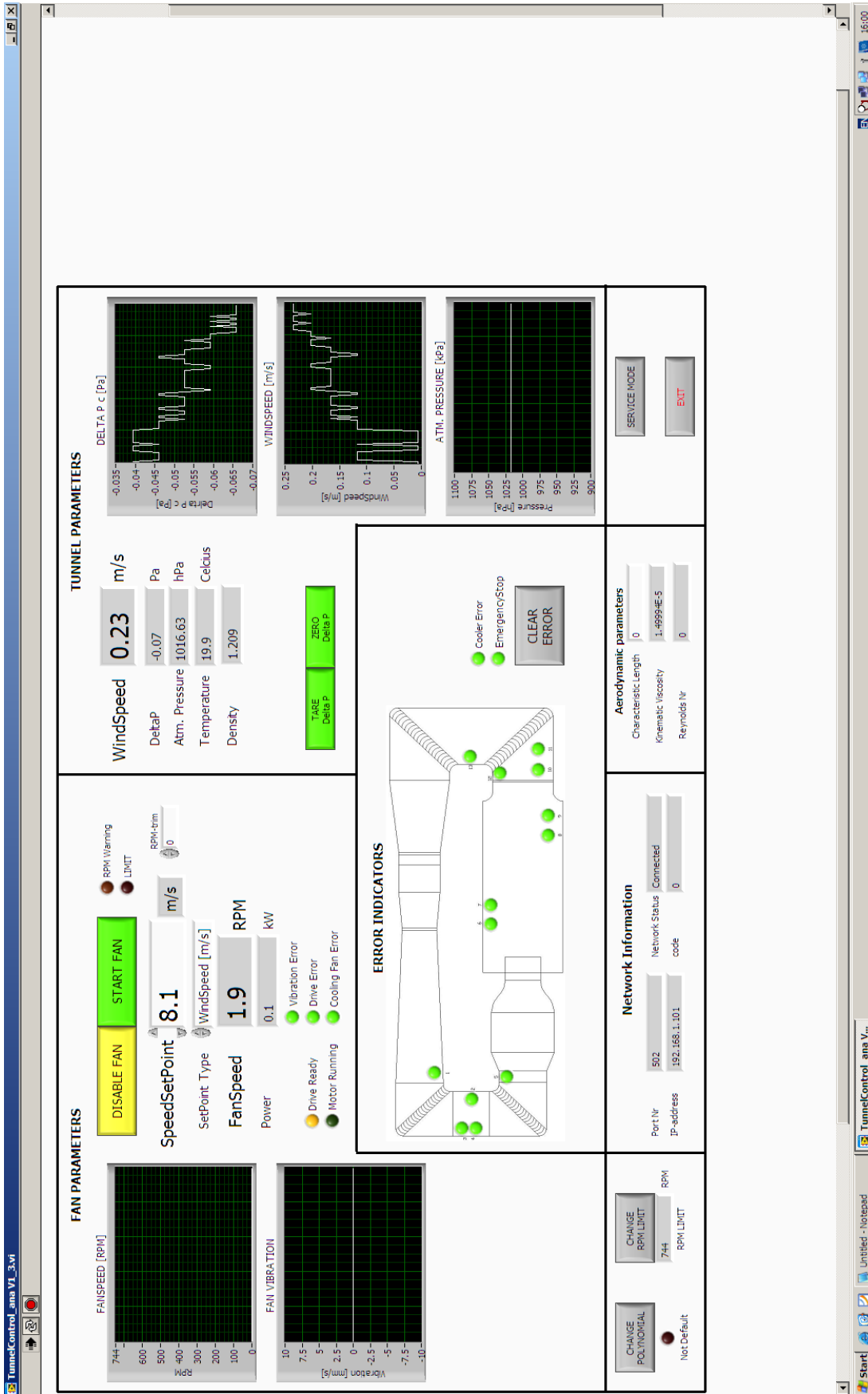**Figure A.3:** Screen capture of the Drive Com software that controlled the rpm of the turbine.
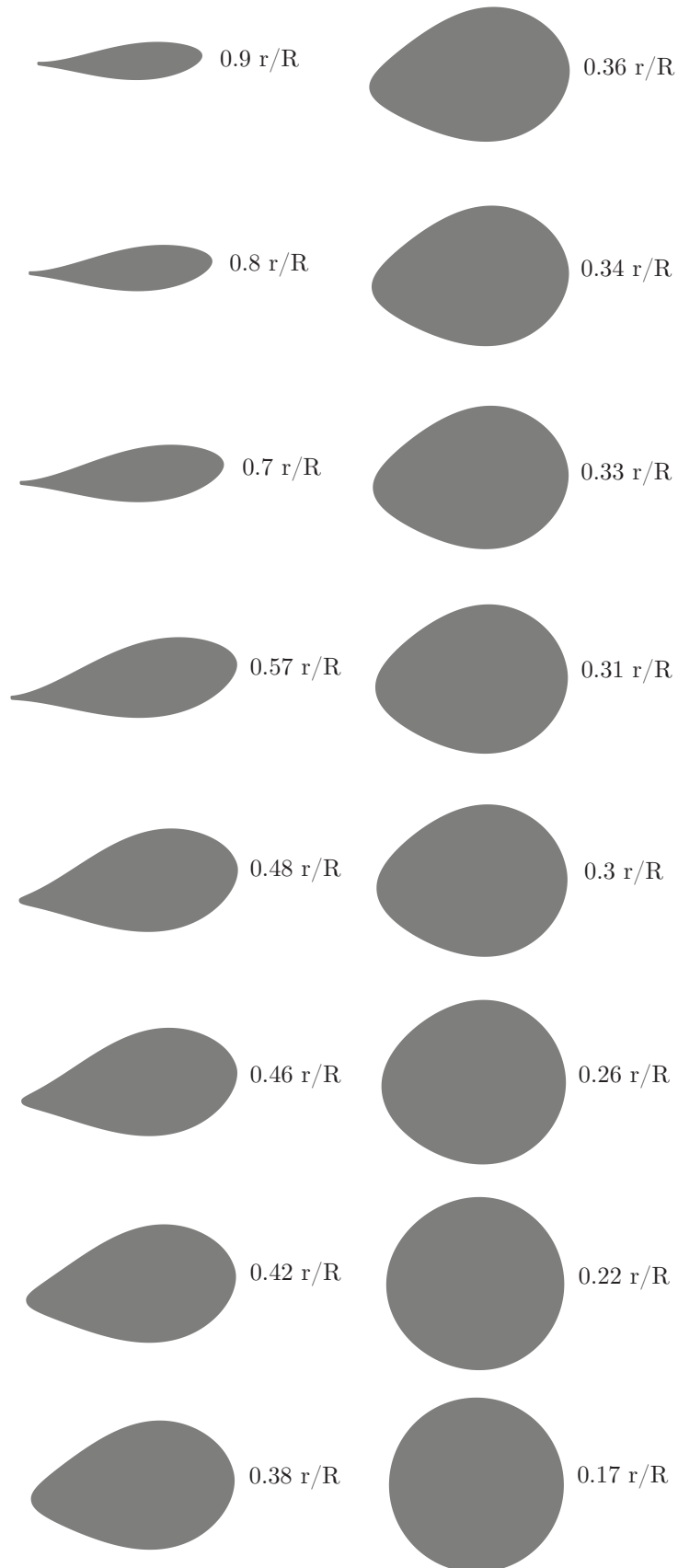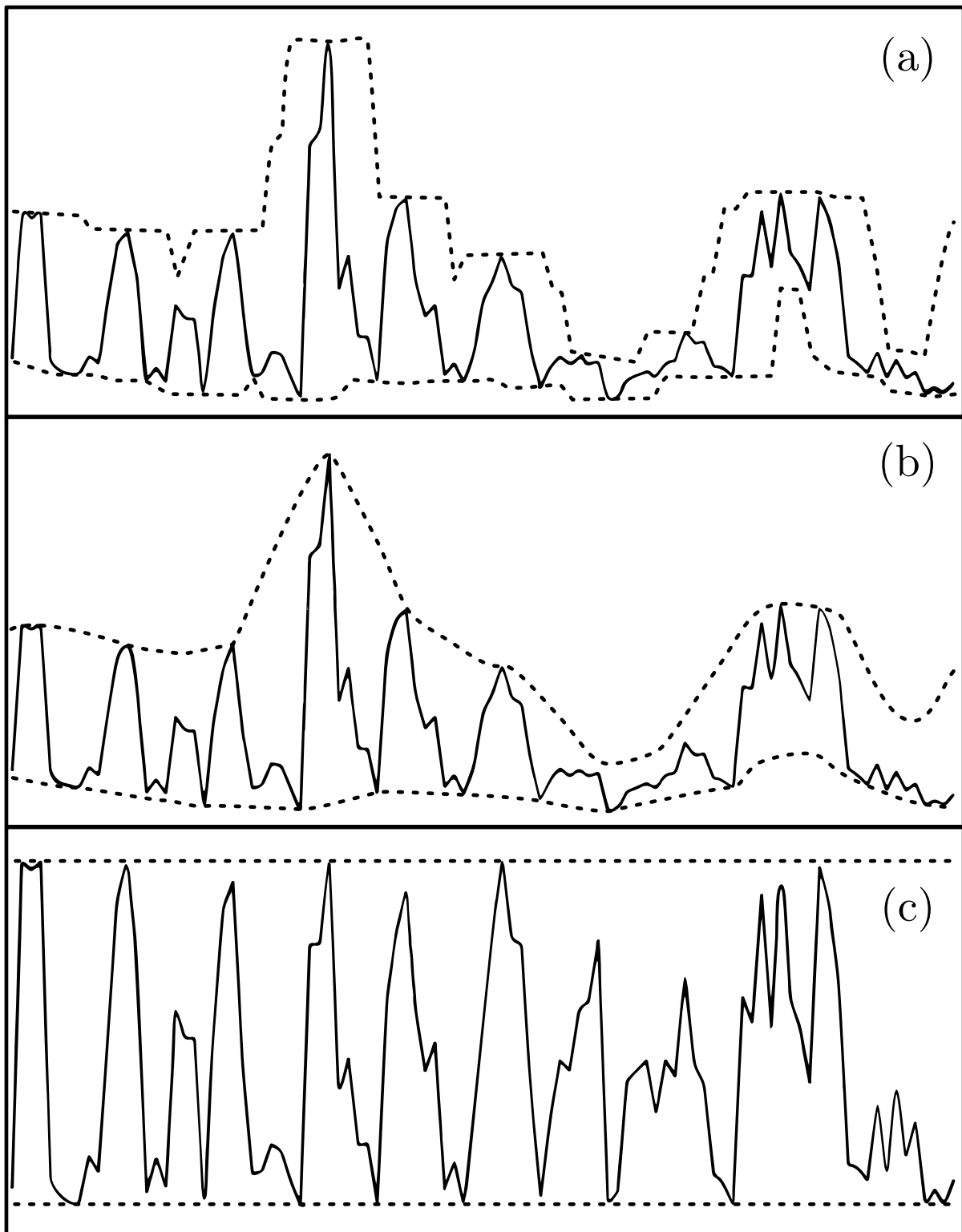
Figure A.4: Screen capture of the Tunnel Control interface used to control the wind speed in the tunnel.

0.9 r/R

0.36 r/R

0.8 r/R

0.34 r/R

0.7 r/R

0.33 r/R

0.57 r/R

0.31 r/R

0.48 r/R

0.3 r/R

0.46 r/R

0.26 r/R

0.42 r/R

0.22 r/R

0.38 r/R

0.17 r/R

Figure A.5: Aerofoils at the different r/R locations

Figure A.6: Example of contrast normalization using min-max filtering applied to a one-dimensional signal. The solid line represents the signal and the dashed lines the upper and lower envelopes: (a) the original signal with local maximum and local minimum envelopes; (b) the envelopes after smoothing with a uniform filter; (c) the signal after subtraction of the lower envelope in (b), and normalization by the difference between the upper and lower envelopes. [40]